

Realistic multi-machine tokamak profile simulations and numerical ramp-down optimization using the RAPTOR code

THÈSE N° 8478 (2018)

PRÉSENTÉE LE 20 AVRIL 2018
À LA FACULTÉ DES SCIENCES DE BASE
SPC - THÉORIE
PROGRAMME DOCTORAL EN PHYSIQUE

ÉCOLE POLYTECHNIQUE FÉDÉRALE DE LAUSANNE

POUR L'OBTENTION DU GRADE DE DOCTEUR ÈS SCIENCES

PAR

Anna TEPLUKHINA

acceptée sur proposition du jury:

Prof. F. Mila, président du jury
Dr O. Sauter, directeur de thèse
Dr E. Joffrin, rapporteur
Dr T. Pütterich, rapporteur
Dr J.-M. Moret, rapporteur



ÉCOLE POLYTECHNIQUE
FÉDÉRALE DE LAUSANNE

Suisse
2018

There can be no doubt that our descendants will learn to exploit
the energy of fusion for peaceful purposes even before its use
becomes necessary for the preservation of human civilization.
— Lev A. Artsimovich, Soviet physicist

To my family

Abstract

Predictive modelling of plasma profiles is an essential part of ongoing research in tokamak plasmas, required for a successful realization of future fusion reactors. This thesis focuses on upgrading the RAPTOR code to extend the area of its applicability for plasma modelling and scenario development. RAPTOR is a light and fast simulator, solving radial transport equations, developed for plasma real-time control. This thesis also demonstrates new strategy for ramp-down optimization.

The RAPTOR transport model has been extended to take into account the influence of the time-varying plasma equilibrium geometry and background kinetic profiles on the evolution of the predicted plasma profiles. It allows to get more realistic predictions of the plasma state in case of rapid changes in the plasma shape and equilibrium. Also transport equations for the ion temperature and plasma particles (electrons and ions) have been implemented in the code. Benchmarks have been performed with more sophisticated transport ASTRA and CRONOS codes and with prescribed data for the particle transport in ITER. With successful benchmarks, we confirm that the new transport equations are solved correctly.

A new ad-hoc transport model based on constant gradients for core and pedestal regions, that is suitable for simulations of transition between H (high) and L (low confinement) modes, has been implemented into RAPTOR. This model assumes “stiffness” of the plasma profiles in the core region, reflecting their relatively weak reaction to changes in the heat flux. Only few transport model parameters have to be prescribed. They are validated with predictive simulations of the time evolution of plasma profiles for TCV, ASDEX Upgrade and JET plasmas. We demonstrate the capabilities of RAPTOR for fast and realistic predictions of plasma state over the entire plasma discharges, i.e. from ramp-up to ramp-down. We have defined characteristic gradients in the “stiff” region for each machine and L/H confinement modes and have obtained a very good agreement with experimental measurements. We have also demonstrated several special cases, where the obtained set of the transport parameters does not work, and proposed possible solutions of the problems.

An optimization procedure for the plasma ramp-down phase has been developed during this work. Nondisruptive termination scenarios are necessary for safe operation of ITER, since it can withstand only a limited amount of plasma disruptions. Automatic optimization algorithms can be applied for searching the optimal ramp-down trajectory. With RAPTOR, optimization results are obtained in a reasonable time (hours). We define the goal of the optimization as ramping down the plasma current as fast as possible while avoiding any disruptions caused by reaching physical or technical limits. Physical constraints are relevant

for most tokamaks, others are technical and related to the specific tokamaks. We show how different goals and constraints can easily be included or updated in order to simulate a new machine. A proper plasma shaping during the current ramp-down can reduce significantly the plasma internal inductance, improving its vertical stability. Specific heating scenarios allow to reduce the drop in β_{pol} during H-L transition, which is important for plasma MHD stability. Results of numerical and experimental ramp-down studies for TCV, AUG and JET plasmas are presented.

Key words: RAPTOR, transport modelling, predictive simulations, electron heat diffusivity, ramp-down optimization

Résumé

La simulation prédictive des profils cinétiques du plasma est une partie essentielle de la recherche en physique des plasmas des tokamaks, qui est importante pour la réalisation des futurs réacteurs de fusion. La présente thèse est dédiée au développement du code RAPTOR afin d'étendre son applicabilité pour la modélisation des plasmas de tokamak et le développement de scénarios. Le code RAPTOR est un simulateur rapide et léger, résolvant les équations de transport radial, qui a été développé pour le contrôle du plasma en temps réel. Cette thèse démontre également une nouvelle stratégie pour l'optimisation de la phase de terminaison des décharges.

Le modèle de transport de RAPTOR est étendu pour prendre en compte l'influence de la dynamique de la géométrie des équilibres du plasma sur l'évolution des profils du plasma. Cette modification nous permet d'avoir des prédictions plus réalistes en cas de changements rapides de la forme et de l'équilibre du plasma. Les équations de diffusion pour la température des ions ainsi que pour les particules du plasma (c'est-à-dire, la densité des électrons et ions) sont également introduites dans le code. Des études comparatives sont réalisées avec les codes de transport plus complexes et sophistiqués : ASTRA et CRONOS, ainsi qu'avec les données prescrites pour le transport des particules dans ITER. Grâce à ces études, nous confirmons que les équations de transport sont résolues correctement par RAPTOR.

Un nouveau modèle de transport ad-hoc a été implémenté dans le code RAPTOR. Il est basé sur des gradients constants, pour les régions centrales et du piédestal, et est adapté aux simulations de transitions entre le mode H (haut) et L (bas confinement). Ce modèle suppose une «rigidité» des profils de plasma dans la région centrale, reflétant leur faible réaction aux changements du flux de chaleur. Seuls quelques paramètres du modèle de transport doivent être prescrits. Ils sont validés par des simulations prédictives de l'évolution temporelle des profils des plasmas de TCV, ASDEX Upgrade et JET. Nous démontrons les capacités du code RAPTOR pour des prédictions rapides et réalistes des profils du plasma sur les décharges de plasma complètes, i.e. de la phase initiale à la phase de terminaison. Nous avons défini des gradients caractéristiques dans la région «rigide» pour chaque machine et mode de confinement bas/haut et nous avons obtenu un très bon accord avec les mesures expérimentales. Nous avons également démontré plusieurs cas particuliers, où l'ensemble des paramètres de transport obtenu ne fonctionne pas complètement, et avons proposé des solutions possibles, qui peuvent être implémentées dans le code.

Une procédure d'optimisation de la phase de terminaison du plasma a été développée pendant ce projet. Des scénarios de terminaison sans interruption brutale sont nécessaires pour

ITER, car il ne peut résister qu'à une quantité limitée d'interruptions. Des algorithmes d'optimisation automatique peuvent être appliqués pour la recherche de la trajectoire optimale. Avec RAPTOR, les résultats d'optimisation sont obtenus dans un délai raisonnable (heures). Nous définissons l'objectif de l'optimisation comme la réduction du courant de plasma le plus rapidement possible, en évitant toutes les interruptions causées par l'atteinte de limites physiques ou techniques. Les contraintes physiques sont pertinentes pour la plupart des tokamaks. D'autres contraintes sont techniques et liées aux tokamaks spécifiques. Nous démontrons comment ces objectifs et contraintes peuvent facilement être inclus ou révisés pour simuler une nouvelle machine. Une diminution rapide de l'élongation du plasma peut réduire de manière significative l'inductance interne du plasma, améliorant sa stabilité verticale. Les scénarios de chauffage spécifiques permettent de réduire la chute de β_{pol} pendant la transition H-L, ce qui est important pour la stabilité MHD du plasma. Les résultats des optimisations numériques et expérimentales pour les plasmas TCV, AUG et JET sont présentés.

Mots clés : RAPTOR, modélisation de transport, simulations prédictives, diffusivité de chaleur des électrons, optimisation de terminaison

Contents

Abstract	i
Résumé	iii
Contents	v
1 Introduction	1
1.1 Nuclear fusion and plasmas	1
1.2 Plasma confinement with tokamaks	2
1.2.1 Conception of the tokamak device	3
1.2.2 Heating systems for tokamaks	4
1.2.3 Diagnostic systems for tokamaks	5
1.2.4 Tokamaks relevant for this thesis	6
1.3 Thesis motivation	7
1.4 Thesis outline	9
2 The RAPTOR code: overview and developments	11
2.1 Capabilities of the RAPTOR code	12
2.1.1 Real-time control of a tokamak plasma	12
2.1.2 Off-line predictive simulations	13
2.2 Processing of the equilibrium data	14
2.3 Overview of the transport equations	17
2.3.1 The flux diffusion equation	18
2.3.2 The energy transport equation	20
2.3.3 The particle transport equation	22
2.3.4 Modelling of MHD instabilities	23
2.3.5 A fixed geometry assumption	25
2.3.6 RAPTOR transport equations summary	26
2.4 Code development: time-varying geometry	29
2.4.1 Extension of the transport equations for the time-varying equilibrium	29
2.4.2 Verification with the ASTRA code	29
2.5 Code development: additional transport equations	31
2.6 Code development: the gradient-based transport model	32
2.6.1 The gradient-based electron heat diffusivity	33

Contents

2.6.2	The gradient-based transport coefficients for electrons	36
2.6.3	The gradient-based ion heat diffusivity model	38
2.6.4	Profiles sensitivity to the boundary conditions	39
2.6.5	Summary of the transport model parameters	40
2.7	Summary	41
3	Entire shot simulations with the RAPTOR code	45
3.1	Predicted parameters for a RAPTOR run	46
3.2	TCV plasma modelling	48
3.2.1	An ohmic L-mode shot	48
3.2.2	An entire shot simulations in case of H-mode plasma	54
3.2.3	Simulation in case of off-axis heating	59
3.3	ASDEX Upgrade plasma modelling	62
3.3.1	Standard H-mode discharge	62
3.3.2	AUG H-mode discharge with time-varying transport gradients	65
3.4	JET plasma modelling	67
3.4.1	An entire shot simulation	67
3.4.2	Simulation of hollow profiles for the electron temperature	71
3.5	Summary	71
4	Optimization of the ramp-down phase	75
4.1	Overview of the ramp-down issues for a tokamak plasma	77
4.2	Formulation of the optimization problem	79
4.2.1	Optimization parameters	80
4.2.2	The cost function	82
4.2.3	The constraint function and other optimization limits	82
4.2.4	Summary for the optimization algorithm	84
4.2.5	Simple 2D optimization	85
4.3	Ramp-down optimization for TCV	87
4.3.1	Numerical optimization	87
4.3.2	An experimental test	88
4.4	Ramp-down optimization for ASDEX Upgrade	89
4.4.1	Numerical optimization	89
4.4.2	Experimental tests	91
4.5	Ramp-down optimization for JET	94
4.6	Ramp-down trajectories sensitivity	95
4.6.1	Trajectories sensitivity to transport parameters	95
4.6.2	Trajectories sensitivity to the geometry interpolation	97
4.7	Summary	97

5 Conclusion	101
5.1 Summary on the RAPTOR code updates	101
5.2 Summary on realistic plasma profiles simulations with the RAPTOR code	103
5.3 Summary on the numerical ramp-down optimization	105
A Equilibrium quantities required by RAPTOR	107
B Numerical implementation of the transport equations	111
C The PI controller for the electron transport models	115
Bibliography	119
Acknowledgements	133
Curriculum Vitae	135

1 Introduction

1.1 Nuclear fusion and plasmas

In contrast to nuclear fission, nuclear fusion is a reaction in which colliding multiple atomic nuclei join together into a heavier nucleus. The total mass of the light nuclei is bigger than the mass of the resulted heavy nucleus leading to a positive energy outcome of the fusion reaction, because of the difference in the binding energy. Stars produce large amounts of energy, spread across the Universe, thanks to nuclear fusion. This way of power generation is cleaner and safer than nuclear fission and requires smaller amount of fuel. Therefore an idea of fusion reactors is very attractive for the worldwide electricity production. Research related to the controlled nuclear fusion has been started in the 1950's and continues nowadays.

Stars interior, where this reaction occurs, consists of nuclei (fully ionized neutral atoms), electrons and neutral atoms and stays in a special state of matter called plasma. In addition to solid, liquid and gas states, plasma is the fourth state of matter and, in a general sense, is a quasi-neutral mixture of charged particles and neutrals characterized by collective properties. Plasma is neutral globally but not locally on a characteristic Debye length, which leads to its quasi-neutrality. The collective behavior of charged particles arises from their interactions through locally generated electric and magnetic fields.

To fuse, two positive nuclei have to overcome strong repelling forces. If their energy is high enough, they can exceed the Coulomb barrier between them and come closer such that the nuclear force becomes dominant, resulting into the fusion of a heavy nuclei. The cross-section of fusion reaction, i.e. its probability, depends on the temperature of nuclei. There are various fusion reactions in stars where even such heavy elements like carbon and iron can be produced. However, the dominant process of the energy degeneration in main-sequence stars, like the Sun, is hydrogen fusion into helium. Moreover the reaction between two isotopes of hydrogen, deuterium (D) and tritium (T), has the largest reaction cross-section [Wesson(2004)]. As it is shown in Fig. 1.1, the fusion reaction between D and T nuclei produces a nucleus of helium H_e and a neutron n . Because of the positive outcome of the fusion reaction, the products get additional kinetic energy, where 3.5 MeV go to heavier H_e and 14.1 MeV to n .

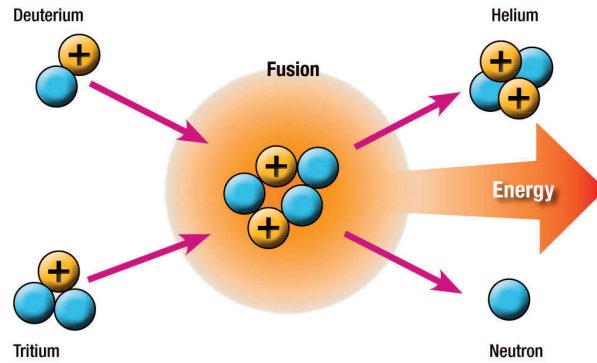


Figure 1.1: The D-T fusion reaction produces helium H_e and a neutron n . Released fusion energy is transferred to the kinetic energy of the reaction products. Reproduced from iter.org.

The fusion reaction is self-sustained if the plasma heating by its products maintains the plasma temperature against various losses without an additional power input. This state is called “ignition”, and the Lawson criterion [Lawson(1957), Wesson(2004)] gives a minimum required value for the product of the plasma density n and temperature T , assuming they are equal for all plasma species, and the energy confinement time τ_E to reach this state. The latter parameter τ_E equals to the ratio of the plasma energy to power losses and its smaller value indicates that more power is needed to maintain plasma energy at the required level. The “ignition” condition developed for the D-T reaction gives

$$nT\tau_E > 3 \cdot 10^{21} \text{ keV s m}^{-3}. \quad (1.1)$$

Thus, for the plasma to be self-sustained, the triple product of the plasma parameters has to be larger than the minimum value defined with the Lawson criterion.

1.2 Plasma confinement with tokamaks

In order to produce fusion power in a controlled way, conceptions of various devices for plasma confinement have been proposed. Since the plasma is a mixture of charged particles, they can be governed by external electromagnetic fields. Thanks to the Lorentz force $\mathbf{F} = q(\mathbf{E} + \mathbf{v} \times \mathbf{B})$, particles of a charge q and with velocity \mathbf{v} in the presence of the electromagnetic field (\mathbf{E}, \mathbf{B}) gyrate around the magnetic field lines with \mathbf{v}_\perp and move parallel to the field with \mathbf{v}_\parallel , resulting in a helical trajectory. The motion direction depends on the charge q , i.e. it is opposite for electrons and ions. One of the most promising design for the investigation of the magnetically confined plasma is a tokamak [Artsimovich(1972)], an abbreviation from Russian “toroidal chamber with magnetic coils”.

1.2. Plasma confinement with tokamaks

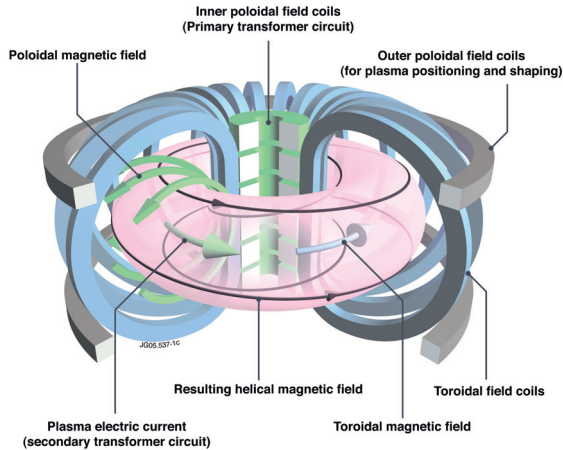


Figure 1.2: The principle scheme of a tokamak. Reproduced from euro-fusion.org.

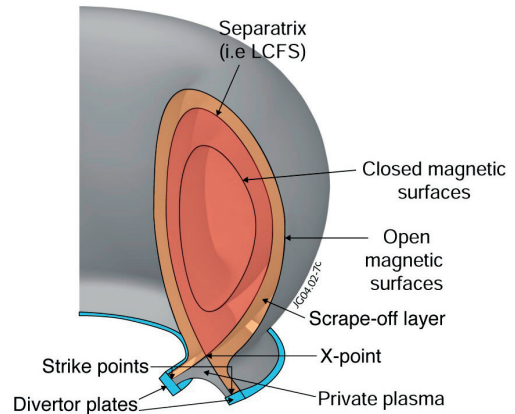


Figure 1.3: The tokamak plasma poloidal cross-section with the divertor plates. Reproduced from euro-fusion.org.

1.2.1 Conception of the tokamak device

A tokamak is a device of a torus shape which confines a plasma with the help of the helical magnetic field, as shown in Fig. 1.2. This complex magnetic field can be split into two components, defining the fields in toroidal (the blue arrow) and poloidal (small green arrows) directions. The toroidal field coils (blue coils arranged in the poloidal plane) induce the toroidal magnetic field. The primary coil circuit (green inner coils) generates the plasma current by induction in the toroidal direction (the big green arrow), which produces the magnetic field in the poloidal direction. The combination of the toroidal and poloidal fields results in helical field lines, and charged particles in a plasma are confined by following these field lines. Tokamak toroidal geometry leads to the generation of a hoop force in the outward direction of the torus. This force is balanced by applying a vertical magnetic field produced by the outer poloidal coils. Also additional poloidal coils are used for the stabilization and control of the plasma position and shape.

The plasma is placed inside the toroidal chamber away from the wall, since no material can withstand against the plasma extreme temperatures. As it is shown in Fig. 1.3, the tokamak plasma can be split into several characteristic areas [Wesson(2004)]. The plasma core (an area in dark red) consists of charged particles following closed magnetic field lines. Then there is a magnetic surface (the last closed flux surface LCFS or separatrix) sharply separating closed field lines, forming the nested magnetic surfaces, from open field lines, intersecting the vessel wall. Open field lines form the region between LCFS and machine-wall components (an area in dark yellow), called the scrape-off layer (SOL). In an ideal case, charged particles would stay confined in the plasma core. However, because of collisions between particles and various plasma instabilities leading to local field fluctuations, particles can move in the radial direction, changing the guiding magnetic field lines. The structure of the open magnetic field lines have to be optimized to guide charged particles in the safest way for the device. According to one of the most promising design, so called “poloidal divertor tokamaks”, the

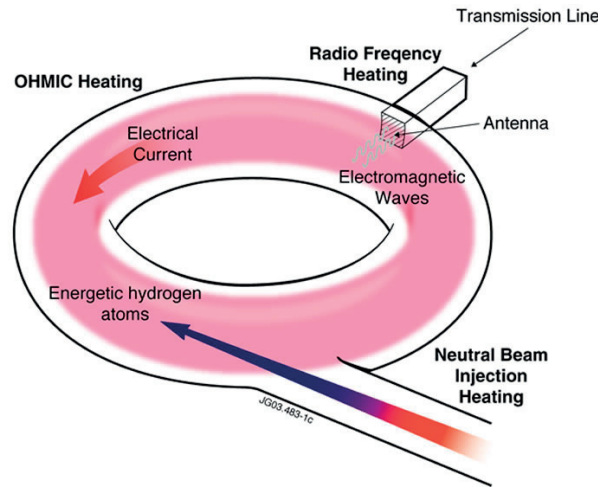


Figure 1.4: A tokamak plasma heating: ohmic heating with the plasma current, injection of neutral particles (NBI) and electromagnetic waves of different frequencies. Reproduced from euro-fusion.org.

open magnetic field lines, thus charged particles, are diverted into a dedicated region, divertor plates (marked in blue in Fig. 1.3), at the vessel wall from where they are pumped away.

1.2.2 Heating systems for tokamaks

The Sun core is strongly compressed by the gravity forces resulting in the plasma high pressure. In tokamaks according to the Lawson criterion 1.1, a plasma has to be heated externally to have sufficiently high plasma temperatures. Since the plasma conductivity increases with its temperature, the ohmic heating is not efficient at high plasma temperatures. There are two main ways for the plasma external heating: injection of neutral beams (NBI) and electromagnetic waves at resonance frequencies for plasma particles, presented in Fig. 1.4.

In case of NBI heating, a beam of highly energetic neutrals is injected directly into a plasma ([Kelley et al.(1972), Koch(2006b)] and references therein). The beam is typically generated from deuterium ions. Since injected particles are initially neutral, they are not affected by the magnetic field and can penetrate rather deeply into the plasma interior. Through collisions with ions and electrons, they become ionized. Such generated high energetic ions are confined in the tokamak and transfer their energy to plasma particles increasing the overall plasma temperature. Neutral beams can be injected along the main radius of the torus or in the direction of the plasma current, i.e. tangentially to the torus. Depending on the direction of its injection, NBI can drive an additional plasma current and change the plasma rotation.

An injection of electromagnetic waves at different frequencies into the plasma is another way of heating. Depending on the frequency, the waves can interact more effectively with electrons or ions. In case of ion cyclotron resonance heating (ICRH) low radio frequency

waves (30 MHz to 55 MHz) are used ([Koch(2006a)] and references therein). A special antenna, located in the vacuum vessel, sends the high-power radio frequency waves into the plasma, heating mainly the plasma ions (ICRH) and driving the ion cyclotron current (ICCD). Electron Cyclotron Resonance Heating (ECRH) heats the electrons with high-frequency waves (100 GHz to 170 GHz) which resonate with the electron cyclotron motion around the field lines ([Westerhof(2006)] and references therein). The electrons absorb the waves energy and transfer it to ions through collisions. Another method for plasma heating is Lower Hybrid heating (LHRH) and current drive (LHCD) using intermediate frequency waves (around 5 GHz) ([Koch(2006a)] and references therein). Depending on the plasma density, dominant heating goes to electrons or ions. The ECRH method is less difficult from the technical side than ICRH. Since high-frequency waves can propagate through vacuum, the ECRH system does not need an antenna installed in the vacuum vessel. However, an efficiency of the current drive (ECCD) is lower than LHCD.

1.2.3 Diagnostic systems for tokamaks

Main plasma characteristics like particles temperature and density, radiation losses, the magnetic topology and plasma fluctuations can be determined with the help of special measuring systems, called “diagnostics”. Direct measurements inside the plasma are hardly possible for two reasons. Since the tokamak plasma is extremely hot, it can melt sensitive elements of a diagnostic. Secondly, such an external disturbance can bring impurity to the plasma and lead to loss of particle and heat confinement. Thus, the information about the plasma state has to be collected from outside with electromagnetic and radiation measurements. There is a large amount of diagnostics common for most of existing tokamaks or developed for a specific goal. Below, only a few of them, relevant for this thesis, are mentioned.

To measure the electron temperature and density of the plasma, the Thomson scattering diagnostic is widely used on existing tokamaks [Bowden et al.(1999)]. With intense bursts of laser light, the thermal motion of the plasma electrons is affected, since the electrons are accelerated in the laser oscillating field and re-emit radiation. Analyzing the scattering of laser light, the electron temperature can be determined from the broadening of the radiation spectra while the density is proportional to the total scattered power. Another common way to determine the electron temperature is measurement of the electron cyclotron emission (ECE) [Celata and Boyd(1977)], i.e. the emission due to the Larmor motion of the electrons around the magnetic field lines.

Soft X-ray radiation gives important information on plasma heat and particle behavior, since it consists of radiation coming from various sources, like the electron-ion Coulomb collisions (Bremsstrahlung), electron-ion recombination, and line radiation. These measurements can be done with the help of the Duplex Multiwire Proportional X-ray counter (DMPX), a soft X-ray diagnostic, for example.

Many properties of a tokamak plasma can be determined with magnetic measurements using

	TCV	AUG	JET	ITER
Major radius [m]	0.89	1.65	3	6.2
Minor radius [m]	0.25	0.5	0.9	2.0
Magnetic field [T]	1.43	3.1	4	5.3
Plasma current [MA]	1	2	5	15
Maximum elongation	2.8	1.8	1.8	1.85
Additional heating (up to) [MW]	7	27	42	73
Plasma volume [m ³]	1	13	100	840

Table 1.1: Main characteristics for tokamaks TCV, AUG, JET and ITER.

simple loops or coils of wire. Measurements with poloidal, toroidal and Rogowski coils of variation in the magnetic flux give information on the plasma current and its distribution, plasma position and shape, stored plasma energy, and plasma instabilities. Diamagnetic measurements are used to derive the plasma pressure from the measured toroidal flux. On the TCV tokamak, rapid changes in plasma pressure can be measured thanks to additional single loops placed outside the vessel [Moret et al.(2003)].

1.2.4 Tokamaks relevant for this thesis

In the last fifty years, thanks to the growth of the plasma community interest in the tokamak conception, many tokamaks have been constructed around the world. In this thesis we focus on three of them: the Tokamak à Configuration Variable (TCV) in EPFL/Lausanne (Switzerland), the ASDEX Upgrade tokamak (AUG) near Munich (Germany) and The Joint European Torus (JET) near Oxford (UK). These tokamaks have similar geometry and operational domains, thus plasma transport characteristics are similar too. Main characteristic of the machines are shown in Table 1.1.

In order of the preparation to ITER (“the way” in Latin) [Shimada et al.(2007)] operation, an investigation of the plasma behavior and fusion properties is one of the major goals for the nuclear fusion community. ITER is an international collaborative project for an experimental fusion reactor with the first plasma planned in 2025. The main subject of this project is a demonstration of the feasibility of a fusion reactor which includes generation of a plasma that is dominantly heated by fusion reactions and a demonstration that an integrated design can meet the technological constraints.

The Tokamak à Configuration Variable (TCV) [Hofmann et al.(1994)] started operation in 1992. It is a medium size, highly elongated tokamak, capable of producing limited or diverted plasmas with currents up to 1 MA. It has been developed to investigate effects of the plasma shape on the plasma stability and confinement properties. The magnetic control system consists of 16 poloidal field coils, 7 coils forming the Ohmic transformer primary, 16 toroidal field coils and two internal (fast) coils placed inside the vessel for vertical position control. To produce stable plasmas of various shapes, poloidal field coils are controlled by 16 independent

power supplies. TCV has good capabilities in Electron Cyclotron Heating (ECH) and Electron Cyclotron Current drive (ECCD) thanks to the powerful and flexible system, consisting of six 82.7 GHz gyrotrons coupled in two clusters for heating at the second harmonic of electron cyclotron resonance and of three 118 GHz gyrotrons in one cluster for heating at the third harmonic. The 82.7 GHz gyrotrons launchers are located at two equatorial and four upper lateral ports. The nominal power of each 82.7 GHz gyrotron is 465 kW resulting in total of 2.79 MW of heating power at the second harmonic with 2 s of maximum pulse length. The first (inner) wall of the TCV vacuum vessel is covered with graphite tiles, thus carbon is the main impurity. It has been recently updated with 1 MW NBI heating source [Coda et al.(2017)].

The ASDEX Upgrade tokamak is based on the Axial Symmetric Divertor Experiment, which divertor conception was upgraded in 1991. In 2007 the machine was upgraded to all-W divertor tokamak, when the graphite tiles were replaced by the W-coated ones [Neu et al.(2007)]. The magnetic coils system consist of 16 toroidal coils and 12 vertical field coils for plasma shape and position control. The plasma is kept in its elliptical shape with an X-point above the bottom divertor. The toroidal magnetic field is usually kept constant during the entire discharge. Additionally there are two vertical field coils close to the plasma for the fast plasma position control. The main scientific goals of the device are investigation of the divertor physics, plasma transport and plasma fueling with pellets. There are various systems of additional heating, in particular 8 NBI injectors, 4 ICRH antennas and 8 gyrotrons for ECRH [Kallenbach et al.(2017)].

The Joint European Torus (JET) started operations in 1983. At this moment, is the largest tokamak in the world. Designed to study plasma properties in conditions approaching those needed for a fusion reactor, it is the only device currently operating that can use the deuterium-tritium fuel mixture [Litaudon et al.(2017)]. In addition to the central solenoid consisting 10 modules, JET has 32 toroidal field coils and 6 poloidal field coils. In 2011 the first wall of the vacuum vessel was upgraded to have an ITER-like wall, with the beryllium main wall and the full-tungsten modules in the divertor. The additional heating system provides 34 MW with NBI, 10 MW with ICRH and 7 MW with LHCD.

1.3 Thesis motivation

For a successful realization of the project aiming to producing fusion power in future reactors, transport codes suitable for predictive/interpretative plasma simulations and plasma real-time control are beneficial. The development of such codes and controllers require experimental and numerical studies of the plasma behavior on existing tokamaks. In recent years, such integrated codes like DINA [Khayrutdinov and Lukash(1993)] and CRONOS [Artaud et al.(2010)], enable for simulation of plasma and full tokamak environment, have been developed. Because of their complexity, numerical simulations take significant time. However, it might be very useful to test and verify plasma control systems using simulation models that can be executed in real-time [Humphreys et al.(2015)]. For such purposes, a fast, control-oriented simulation code, capable of predicting the plasma quantities, is required. One of such codes developed

Chapter 1. Introduction

for the real-time plasma control is RAPTOR, the RAPid Plasma simulatOR. This thesis focuses on investigation of the reliable physical models required for the realistic description of the time evolution of the plasma state, and contributes to the development and optimization of plasma ramp-down scenarios with the RAPTOR code.

The RAPTOR code has been developed for plasma real-time control, aiming to fast and accurate predictions of the plasma state [Felici(2011), Felici et al.(2011), Felici et al.(2012)]. In order to reduce computing time, its transport model has been simplified assuming fixed plasma equilibrium. The code has been focused on off-line and real-time predictions of the poloidal magnetic flux and the electron temperature, since these parameters provide most important information on the plasma state and many other plasma parameters can be estimated from them. Moreover, appropriate analytical, and therefore fast, models for transport coefficients have been available. To expand an area of the code applicability, several upgrades were required with respect to the version reported in [Felici et al.(2012)]. To get realistic predictions of the plasma profiles in case of rapid changes in the plasma shape and equilibrium, the time-varying plasma equilibrium geometry has to be taken into account. Rapid coupled simulations of heat and particle transport open new directions in the development of real-time controllers on existing machines. Therefore, as part of this thesis, the transport model of the RAPTOR code is extended with time-varying geometrical terms and diffusion equations for ions and electron particles.

To keep the high speed of simulations with the RAPTOR code, we need simple or at least fast models for heat and particle transport. A new model, implemented in the code as part of this thesis, is based on [Kim et al.(2016)]. This model assumes “stiffness” of the plasma profiles in the core region, reflecting their weak reaction to changes in the heat flux [Garbet et al.(2004), Sauter et al.(2014)] and on the global confinement properties. It is a fast model, requiring few prescribed parameters, which are based on experimental measurements, and therefore, they can be easily checked. However, because of the initial conception, the model developed in [Kim et al.(2016)] is not suitable for transport modelling in case of fast changes in the plasma state, like transitions between low and high confinement modes. Since with the recent upgrades in the RAPTOR code, we are focusing on simulations of entire plasma discharges with time-varying shape and equilibrium, the transport model is upgraded to allow fast changes in the transport parameters. Although the developed model for temperature and density profiles may not have as high predictive capabilities as models based on first principles, it gives reliable profiles on long plasma time scales. Thus, thanks to the high speed of the model and its good predictive capabilities, it can be used to estimate the plasma behavior in real-time and to develop plasma scenarios off-line.

In this thesis, in particular, we contribute to the development of scenarios for the final stage of the plasma discharge. This termination stage is characterized by the decrease in the plasma current, pressure and volume. In a programmed way, plasma has to be guided from a high energetic state to the cold low density plasma. Because of simultaneous changes in various plasma parameters, plasma stability limits or machine safety requirements can be easily

broken, leading to a plasma disruption and potentially to machine damages. Nondisruptive termination scenarios are especially important for future fusion reactors, since they have to be designed in a way to produce the fusion energy uninterruptedly. Because of the approaching initiation of ITER operations, an investigation of the plasma behavior during the ramp-down phase and development of safe plasma ramp-down strategies become more crucial, prompting more numerical and experimental studying focused on this topic. In the past, automatic optimization algorithms were used for study of the plasma ramp-up phase [Felici et al.(2012)]. In this thesis, numerical optimization studies are carried out for the plasma ramp-down phase, including for the first time the effects of plasma geometry and additional heating. Automatic optimization algorithms can be applied for searching of optimal ramp-down trajectories, providing a nondisruptive plasma ramp-down within physical and technical limits of a machine. Since RAPTOR is a fast simulator, enable for ramp-down plasma simulations, we use it in the numerical ramp-down optimization procedure, developed as part of this thesis.

1.4 Thesis outline

The first chapter is dedicated to a brief introduction to plasma physics and thermonuclear fusion, a general description of a tokamak plasma device, heating and diagnostic systems. Numerical and experimental research has been carried out as part of this thesis for the TCV, AUG and JET tokamaks, briefly introduced as well in this chapter with specifications of the main tokamak parameters. The rest of the thesis is organized in the following way:

- Chapter 2 gives an overview of the RAPid Plasma Transport simulatOR (the RAPTOR code) what is the main tool for plasma modelling in this work. The code updates, carried out as part of this thesis, are presented. The diffusion equations, describing plasma transport, are extended with time varying terms increasing the range of the code applicability. New ad-hoc models for electron and ion transport coefficients suitable for entire plasma discharge simulations with transition between low and high confinement modes are presented.
- Chapter 3 presents simulations of tokamak plasma discharges for TCV, AUG and JET tokamaks. We demonstrate the capabilities of the RAPTOR code for realistic predictions of plasma profiles for different machines, confinement modes and heating scenarios. With a simple set of the prescribed parameters for the developed transport model, we can well predict the evolution of the plasma state on global scales, and of the radial profiles, in various operation regimes and scenarios.
- Chapter 4 discusses the ramp-down optimization algorithm and provides its brief overview. Preliminary numerical optimization results are presented for TCV, AUG and JET tokamaks. Proper plasma shaping and specification of the time instant of the H-to L-mode transition can help to control the radial and vertical positions of a plasma discharge. Experiments, dedicated to tests optimized trajectories and development of the ramp-down scenarios, are discussed.

Chapter 1. Introduction

- Chapter 5, concluding the thesis, discusses the main results obtained in the thesis, and a brief outlook for future research directions is presented.

Part of this thesis, related to the electron heat transport and the implementation of the time-varying terms in the code, has been published in [Teplukhina et al.(2017)].

2 The RAPTOR code: overview and developments

Reliable plasma simulators are necessary for development of operational scenarios and real-time controllers for future devices like ITER to reduce risks of its ineffective management in terms of safety and expenses. Sophisticated physical models are required, therefore their development with the help of numerical and experimental studies, and the following validation on existent machines, are essential part of ongoing research in a field of integrated plasma modelling. There are various control-oriented codes developed for fast tokamak plasma simulations, like the METIS code, part of the CRONOS suite [Artaud et al.(2010)], and the transport simulator developed at Lehigh University [Ou et al.(2007)]. This work is performed mainly with the RAPTOR code, the RAPid Plasma Transport simulatOR [Felici(2011), Felici et al.(2011)]. It is a light and fast code developed for real-time control of a tokamak plasma and installed on the control systems of TCV [Felici et al.(2011)], ASDEX Upgrade [Felici et al.(2016)] and RFX [Piron et al.(2017)] tokamaks.

This chapter is focused on recent upgrades of the RAPTOR transport model, implemented into the code as part of this thesis, to continue development of the code started in [Felici(2011), Felici et al.(2011)]. First of all, RAPTOR transport equations have been extended with time-varying terms. Thus, the time evolution of a plasma geometry and equilibrium can be taken into account for plasma modelling and control [Teplukhina et al.(2017)]. It might change significantly the quality of plasma profiles predicted by the code during phases of a plasma discharge when fast changes in the plasma shape/heating take place. In addition to the current density diffusion, now RAPTOR allows for coupled simulations of heat and particle profiles for various plasma species [Felici et al.(2018)], whereas initially only a diffusion equation for the electron temperature was simulated. This upgrade of the code improves its modelling capabilities and opens new opportunities for controllers development on existent and future tokamaks. Corresponding models for transport coefficients for electrons and ions have been implemented into the code and tested as part of this thesis.

The chapter is organized as follows. Three sections are dedicated to a general description of the RAPTOR code. In Sec. 2.1 main control and modelling capabilities of the code are discussed. Sec. 2.2 is related to processing of the equilibrium data required by the code. Sec. 2.3 provides

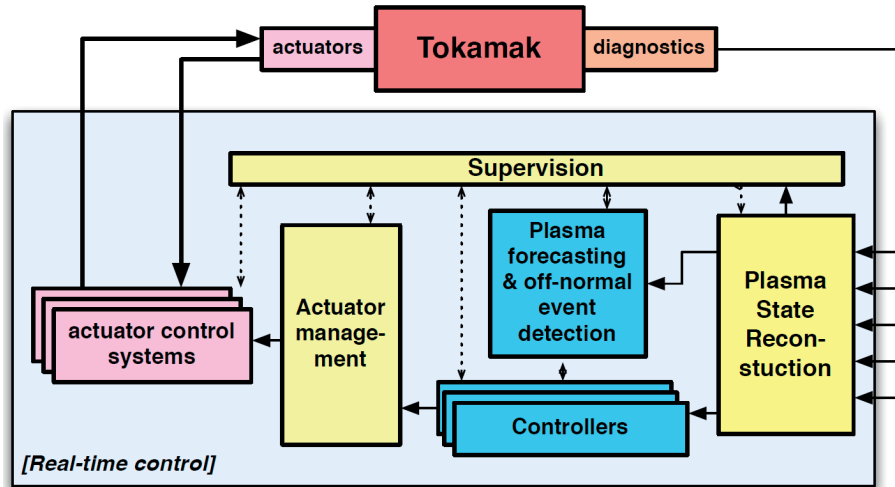


Figure 2.1: The scheme of real-time plasma control. Reproduced from [Felici et al.(2016)].

a general information about the transport equations and models built into the code. Then the chapter continues presenting code improvements developed as part of this thesis. Sec. 2.4 focuses on the extension of the RAPTOR transport equations with time-varying terms, and a benchmark against the ASTRA code [Pereverzev and Yushmanov(2002)] is discussed. A benchmark to verify new transport equations implemented to RAPTOR is demonstrated in Sec. 2.5. Then new ad-hoc models for heat and particle transport are presented in Sec. 2.6. In Sec. 2.7, after summarizing of the main code developments, we discuss possible steps for further improvements of the code.

2.1 Capabilities of the RAPTOR code

The RAPTOR code can be used either in real-time for the plasma control or off-line for plasma modelling. Also one can choose between various transport equations to define plasma parameters for which one is solving for. In real-time, there is an option to use experimental measurements. For example, one can predict the diffusion of the plasma current density (from the poloidal flux $\psi(\rho, t)$) based on various experimental measurements, in particular on measurements of the electron temperature. Otherwise, the time evolution of the plasma kinetic profiles is prescribed from the experiment or is simulated in addition to the plasma current density. In this work we use off-line RAPTOR only.

2.1.1 Real-time control of a tokamak plasma

The main functions of a real-time simulator in a tokamak real-time control scheme are presented in Fig. 2.1. A plasma (the red block “Tokamak”) is affected by various actuators (the pink block “actuators”) like heating systems, external coils for plasma position and shape control, gas puff and other ways of plasma feeding. Its state is estimated by various diagnostic systems

(the orange block “diagnostics”). The plasma state reconstructor simulates the plasma state based on the knowledge of the same actuators as the actual tokamak. The available real-time diagnostics help the simulator to converge to an accurate plasma state. Deviations between measured and simulated values can be used either to estimate disturbances, or to adapt the model parameters in real-time. Based on combinations of controllers output signals, obtained with the help of the reconstructor and measurements, the actuators are adapted for further plasma control. The plasma state reconstructor, the case of RAPTOR, is a model-based plasma state estimator, in which real-time diagnostics are combined with the expected plasma state evolution, known from a model. In particular, the RAPTOR-based plasma profile observer scheme is used to reconstruct profiles. RAPTOR has been constructed as a real-time capable simulator to provide an information on a complex plasma dynamics, including plasma quantities which can not be measured directly. Thus, the controller algorithms do not depend on diagnostics only but can get actual information about the plasma state from the reconstructor which is able to exclude faulty diagnostics signals.

The main advantage of the RAPTOR code is its capability to simulate the time evolution of the plasma state faster than real-time for existing medium-size tokamaks (1 second of a JET plasma can be simulate in around 0.2 second [Felici et al.(2018)]), and also for ITER, which 300 s plasma can be simulated by RAPTOR in about 10 s. Thus the plasma state knowledge provided by RAPTOR can be applied for the plasma forecasting and prediction of various events (like disruptions) and feedback controllers [Humphreys et al.(2015)].

2.1.2 Off-line predictive simulations

Real-time controllers requires reliable physical models, thus, their off-line testing and verifying with experimental data is an essential part of the code development. Thanks to simulation speed and good physical representation, RAPTOR is a perfect tool for a fast post-shot analysis and scenario development. In this work we apply RAPTOR for the optimization of the ramp-down phase since many optimization trajectories can be tested in a reasonable time. For example, an optimization of the AUG plasma ramp-down phase 1 s long might take up to 10 hours depending on the complexity of the optimization task, which consists in simulating about 500 times the 1 s ramp-down phase.

A detailed description of the RAPTOR code can be found in [Felici(2011), Felici et al.(2011), Felici et al.(2012)], and a few major points are given in the following sections 2.2 and 2.3. The code works in a right-handed (R, ϕ, z) cylindrical coordinate system where R is the distance between the vertical axis of the device and a given point in the plasma, ϕ is the toroidal angle defined in the way to have the right-handed system, z is the vertical coordinate as shown in Fig. 2.2. We assume an axisymmetric tokamak equilibrium, i.e. plasma equilibria do not depend on the toroidal angle ϕ , and positive plasma current I_p and magnetic field B_0 . This corresponds, with choice of ψ defined below and the direction of the poloidal angle, to the coordinate convention COCOS=11 [Sauter and Medvedev(2013)] similar to the ITER choice,

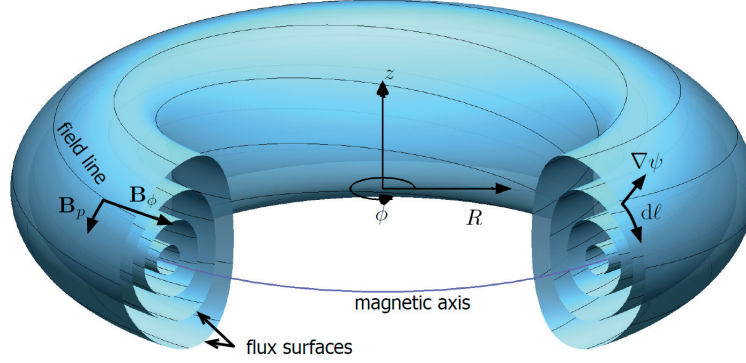


Figure 2.2: Coordinate system for a tokamak geometry, reproduced from [Felici(2011)], corresponding to COCOS=11 as defined in [Sauter and Medvedev(2013)].

but with I_p, B_0 positive.

2.2 Processing of the equilibrium data

The RAPTOR code is a transport simulator without an equilibrium solver. A prescribed plasma equilibrium has to be provided by an external source to model this plasma. Firstly, we discuss briefly main plasma equilibrium quantities. Then, a procedure of equilibrium data processing by RAPTOR is discussed.

The plasma MHD equilibrium

The basic condition in ideal magnetohydrodynamics (MHD) theory [Wesson(2004), Fiedberg(1982)], for a static plasma equilibrium is a balance between the magnetic and kinetic forces:

$$\mathbf{j} \times \mathbf{B} = \nabla p \quad (2.1)$$

where \mathbf{j} and \mathbf{B} are the plasma current density and magnetic field, p denotes the plasma pressure. Because of the tokamak geometry, it is convenient to consider the total magnetic field as a sum of its toroidal \mathbf{B}_ϕ and poloidal \mathbf{B}_p components:

$$\mathbf{B} = \mathbf{e}_\phi B_\phi + \mathbf{B}_p \quad (2.2)$$

The poloidal magnetic flux ψ is defined as a negative flux of the magnetic field through a circle of radius R with its center on the vertical axis, covering an area S_p , and perpendicular to \mathbf{e}_z :

$$\psi(R, z) = - \int_{S_p} \mathbf{B} \cdot \mathbf{e}_z dS \quad (2.3)$$

Similarly, the toroidal magnetic flux Φ is defined as the flux of the magnetic field through a

poloidal plasma cross section, covering an area S_t :

$$\Phi(\psi) = \int_{S_t} \mathbf{B} \cdot \mathbf{e}_\phi dS \quad (2.4)$$

The total magnetic field produces an infinite set of nested toroidal magnetic surfaces, and each of them is characterized by a constant ψ and constant pressure p . Helical magnetic field lines, produced by a combination of the poloidal and toroidal magnetic fields, wrap around the magnetic axis. An averaged twist of the magnetic field on flux surface is defined in terms of the safety factor q which can be expressed as the rate of change of the toroidal flux with the poloidal flux:

$$q = \frac{d\Phi}{d\psi} \quad (2.5)$$

A tokamak plasma stability can be determined in terms of q , which higher values correspond to higher plasma stability because of current-driven instabilities arising when the plasma current reaches its upper limit [Fiedberg(1982)]. The magnetic shear, determined by the radial rate of change of q , is another important characteristic of the plasma stability:

$$s = \frac{\rho}{q} \frac{dq}{d\rho} \quad (2.6)$$

where ρ represents an effective plasma minor radius. This parameter can be related to the toroidal flux Φ enclosed by a flux surface [Pereverzev and Yushmanov(2002)]:

$$\rho = \sqrt{\frac{\Phi}{\pi B_0}} \quad (2.7)$$

The poloidal field \mathbf{B}_p according to Eq. 2.3 can be written as a function of ψ :

$$\mathbf{B}_p = \mathbf{e}_\phi \times \frac{\nabla\psi}{2\pi R} \quad (2.8)$$

It is convenient to rewrite Eq. 2.1 to split poloidal and toroidal terms:

$$\mathbf{j}_p \times \mathbf{B}_\phi + \mathbf{j}_\phi \times \mathbf{B}_p = \nabla p \quad (2.9)$$

Equation 2.9 written as function of ψ after some algebra leads to the famous Grad-Shafranov equation [Grad and Rubin(1958), Shafranov(1958)] which describes the static ideal MHD equilibrium of an axisymmetric magnetically confined plasma:

$$\Delta^* \psi = -4\pi^2 \left(\mu_0 R^2 \frac{\partial p(\psi)}{\partial \psi} + \frac{\partial F(\psi)}{\partial \psi} F(\psi) \right) \quad (2.10)$$

where $p(\psi)$ is the plasma pressure with contribution from all species and $F(\psi) = RB_\phi$ is the

Chapter 2. The RAPTOR code: overview and developments

poloidal plasma current function. Here the elliptic operator Δ^* is:

$$\Delta^* \psi = R^2 \nabla \cdot \left(\frac{1}{R^2} \nabla \psi \right) = R \frac{\partial}{\partial R} \left(\frac{1}{R} \frac{\partial \psi}{\partial R} \right) + \frac{\partial \psi^2}{\partial Z^2} \quad (2.11)$$

Solving Eq. 2.10 is a major task for so called fixed boundary or reconstruction equilibrium codes. Using experimental measurements during or after a plasma discharge, these codes provide time evolution of the plasma equilibrium and distribution of the poloidal flux $\psi(R, Z, t)$, the poloidal functions $p(\psi, t)$, and $F(\psi, t)$.

Tokamaks are modeled as a toroidal transformer, where the plasma toroidal circuit with resistance ν and inductance L is coupled with the primary transformer circuit. Plasma currents inside the vessel can be characterized with the plasma internal inductance l_i , which accounts for the energy stored in the poloidal field B_p created by the plasma current I_p and external poloidal field coils [Romero et al.(2010)]. The internal inductance is associated with internal current density distribution, and its higher values correspond to more peaked density current profiles. Using the definition for ITER [Jackson et al.(2008)], the plasma internal inductance can be calculated in the following way:

$$l_i(3) = \frac{2V \langle B_p^2 \rangle_V}{(\mu_0 I_p)^2 R} \quad (2.12)$$

A plasma performance can be expressed in terms of β [Wesson(2004)], which shows the efficiency of the plasma pressure confinement by the magnetic field B_0 . It is defined as the ratio of kinetic pressure $\langle p \rangle_V$, averaged over the plasma volume V , to magnetic pressure in the following form:

$$\beta = \frac{\langle p \rangle_V}{B_0^2 / 2\mu_0} \quad (2.13)$$

In a similar way, the poloidal parameter β_p can be defined, where a poloidal magnetic pressure is taken into account.

Another important parameter related to the kinetic and magnetic balance is the normalized parameter β_N . It indicates, how close the plasma is to reaching the ideal MHD stability limit [Troyon et al.(1984)]. It is defined for a tokamak plasma with the minor radius a , the toroidal field B_0 , the plasma current I_p in the following way [Miyamoto(2005)]:

$$\beta_N = \beta \frac{a[m] B_0[T]}{I_p[MA]} \quad (2.14)$$

Equilibrium data for RAPTOR

As it was mentioned above, to save calculation time, the RAPTOR code does not solve the

equilibrium equation 2.10 self-consistently with the transport equations but uses equilibria calculated externally. In case of a plasma control, a real-time equilibrium reconstruction code, like RT-LIUQE for TCV [Moret et al.(2015)] or EQUINOX for JET [Mazon et al.(2010)], can provide time-varying plasma equilibria. For off-line simulations, there are various post-shot equilibrium reconstruction codes, for example LIUQE [Hofmann et al.(1988), Moret et al.(2015)] for TCV, CLISTE [Schneider et al.(2000)] for ASDEX Upgrade, EFIT [Lao et al.(1985a)] for JET. Generally, the main disadvantage of these codes is an inaccurate information about evolution of plasma profiles in the core since they use mainly magnetic measurements only for a plasma state reconstruction. Special tools for integrated data analysis, like IDA [Fischer et al.(2003)] for AUG, can be used additionally. Some codes for plasma integrated modelling, like AS-TRA [Pereverzev and Yushmanov(2002)] and CRONOS [Artaud et al.(2010)], solve the Grad-Shafranov equation consistently with plasma transport equations, therefore their output parameters can be used by RAPTOR for an equilibria determination.

An equilibrium data file, generated with the help of these codes, contains information about the various plasma geometry, like the plasma volume, and physical quantities, like the safety factor. The former are prescribed parameters for the RAPTOR code, the latter can be used for validation of the simulation results. If a limited set of equilibria is provided for a simulation of a plasma shot, we assume a linear time-evolution for the plasma geometry between equilibria times slices. Geometrical parameters required by transport equations are discussed below in Sec. 2.3. We use the CHEASE code [Lütjens et al.(1996)], interfaced with EQDSK/EXPEQ files, to compute the various quantities which are reprocessed with an automatic interface in RAPTOR. In Appendix A more details on equilibrium data processing are provided.

2.3 Overview of the transport equations

The transport theory of magnetically confinement plasma provides a closed set of equations describing time evolution of densities and pressures of all plasma species. As was shown in [Hinton and Hazeltine(1976)], this set consists of the conservation laws for particles and energy, determined as even moments of the momentum conservation law, and the fluxes, i.e. moments of the distribution function, for electrons, electron heat, ion heat and an average of the parallel current density. Depending on purposes of a transport code this set can be extended for a specific goal or reduced to a subset of equations under appropriate assumptions to keep it closed.

The transport equations consider a radial transport only. RAPTOR is a 1D simulator, which means that at the every time instant, radial profiles of plasma quantities correspond to their values averaged over a flux surface at the given radial position. Below, the general set of the transport equations for RAPTOR is presented. All equations are constructed on a normalized

toroidal radial grid $\hat{\rho}$, defined as:

$$\hat{\rho} = \sqrt{\frac{\Phi}{\Phi_b}} \quad (2.15)$$

with a toroidal flux, defined in Eq. 2.4, for a tokamak geometry can be written as $\Phi = \pi \rho^2 B_0$ normalized on its boundary value $\Phi_b = \pi \rho_b^2 B_0$. The normalized grid $\hat{\rho}$ does not depend on time but the toroidal flux at the plasma boundary Φ_b does and is provided by an external equilibrium solver.

2.3.1 The flux diffusion equation

The time evolution of the poloidal magnetic flux ψ is solved with the following PDE:

$$\sigma_{\parallel} \left(\frac{\partial \psi}{\partial t} \Big|_{\hat{\rho}} - \frac{\hat{\rho} \Phi_b}{2\Phi_b} \frac{\partial \psi}{\partial \hat{\rho}} \right) = \frac{F^2}{16\pi^2 \mu_0 \Phi_b^2 \hat{\rho}} \frac{\partial}{\partial \hat{\rho}} \left[\frac{g_2 g_3}{\hat{\rho}} \frac{\partial \psi}{\partial \hat{\rho}} \right] - \frac{B_0}{2\Phi_b \hat{\rho}} V'_{\hat{\rho}} j_{ni} \quad (2.16)$$

where $\sigma_{\parallel}(\hat{\rho}, t)$ is the neoclassical conductivity, $F(\hat{\rho}, t) = RB_{\phi}$ is the poloidal current function, $j_{ni}(\hat{\rho}, t)$ is the non-inductive current density, the geometrical parameters are: $V'_{\hat{\rho}}(\hat{\rho}, t) = \partial V / \partial \hat{\rho}$, $g_2(\hat{\rho}, t) = \langle (\nabla V)^2 / R^2 \rangle$, $g_3(\hat{\rho}, t) = \langle 1/R^2 \rangle$ where $\langle \cdot \rangle$ means flux-surface averaging and V is the plasma volume.

The flux diffusion equation represents the Ohm's law, projected on the parallel direction of the magnetic field and averaged over a flux surface:

$$\frac{\langle \mathbf{j} \cdot \mathbf{B} \rangle}{B_0} = \sigma_{\parallel} \frac{\langle \mathbf{E}_{\parallel} \cdot \mathbf{B} \rangle}{B_0} + \frac{\langle \mathbf{j}_{ni} \cdot \mathbf{B} \rangle}{B_0} \quad (2.17)$$

or

$$j_{\parallel} = \sigma_{\parallel} E_{\parallel} + j_{ni} \quad (2.18)$$

The non-inductive current density j_{ni} consists of the currents driven by external systems of auxiliary heating $j_{aux} = \langle \mathbf{j}_{aux} \cdot \mathbf{B} \rangle / B_0$ and the bootstrap current density $j_{BS} = \langle \mathbf{j}_{BS} \cdot \mathbf{B} \rangle / B_0$. Additional currents j_{aux} are driven by various heating systems like injection of neutral particles (NBCD), electron cyclotron waves (ECCD) and so on.

Bootstrap current and neoclassical conductivity

The bootstrap current j_{BS} is a naturally generated current in a tokamak geometry arising from the pressure gradient anisotropy and inhomogeneity of the tokamak magnetic field [Hinton and Hazeltine(1976), Kessel(1994), Peeters(2000)]. This effect is important in low collisional regimes, when there is a significant fraction of charged particles trapped in outer region of a tokamak (the weaker region of the magnetic field), so called the ‘‘banana’’ regime. Formation of trapped orbits is violated in case of high collisionality, what leads to reduction

2.3. Overview of the transport equations

of j_{BS} . The pressure gradient leads to an asymmetry in a velocity space of trapped particles, which is transferred to passing particles through collisions. The momentum balance between trapped and passing charged particles leads to generation of a toroidal current. The density of this current, the bootstrap current, for the RAPTOR code is defined according to [Sauter and C.(1999), Sauter et al.(2002c)]:

$$j_{BS} = -2\pi \frac{F(\psi)}{R_0 B_0} \left(p_e L_{31} \frac{\partial \ln n_e}{\partial \rho} + p_i L_{31} \frac{\partial \ln n_i}{\partial \rho} + p_e (L_{31} + L_{32}) \frac{\partial \ln T_e}{\partial \rho} + p_i (L_{31} + \alpha L_{34}) \frac{\partial \ln T_i}{\partial \rho} \right) \quad (2.19)$$

where L_{31} , L_{32} , L_{34} and α depend on ψ and are based on the fraction trapped particles f_t and the plasma collisionality. Note that the term 2π arises because of a different definition of ψ for RAPTOR than in [Sauter and C.(1999), Sauter et al.(2002c)]. As it can be seen from Eq. 2.19, the bootstrap current has separate contributions from of different gradients for density and temperature.

Passing particles, able to move freely along the magnetic field lines, respond to the present electric field and thus contribute to the plasma conductivity, which corresponds to so called Spitzer conductivity [Hinton and Hazeltine(1976)]. The reduction of the plasma current because of trapped particles has to be taken into account for the plasma conductivity determination. In [Sauter and C.(1999)] the neoclassical conductivity has been defined as:

$$\sigma_{||} = \sigma_{Spitz} \left(1 - \left(1 + \frac{0.36}{Z_{eff}} \right) X + \frac{0.59}{Z_{eff}} X^2 - \frac{0.23}{Z_{eff}} X^3 \right) \quad (2.20)$$

where Z_{eff} is an effective plasma charge, $X(f_t, \nu_{e*})$ is the neoclassical correction depending on the trapped fraction f_t and arbitrary collisionality ν_{e*} . Here we define the effective charge of a mixture of ion particles with charges Z_s and density n_s in the following way:

$$Z_{eff} = \frac{\sum_s n_s Z_s^2}{\sum_s n_s Z_s} = \frac{\sum_s n_s Z_s^2}{n_e} \quad (2.21)$$

using the plasma quasi-neutrality condition [Tonks and Langmuir(1929)]:

$$n_e = \sum_s Z_s n_s \quad (2.22)$$

In the RAPTOR code, the trapped fraction f_t is calculated with an extended formula which includes the effect of triangularity δ [Sauter(2016)]:

$$f_t = 1 - \frac{1 - \epsilon_{eff}}{1 + 2\sqrt{\epsilon_{eff}}} \sqrt{\frac{1 - \epsilon}{1 + \epsilon}} \quad (2.23)$$

where $\epsilon_{eff} = 0.67(1 - 1.4\delta|\delta|)\epsilon$, ϵ is the inverse aspect ratio.

2.3.2 The energy transport equation

Here we write the equation for the energy flux in the common form valid for various species “s” (electrons, ions, other minor species)

$$\frac{3}{2} \frac{1}{(V'_{\hat{\rho}})^{5/3}} \left(\frac{\partial}{\partial t} \Big|_{\hat{\rho}} - \frac{\Phi_b}{2\Phi_b} \frac{\partial}{\partial \hat{\rho}} \hat{\rho} \right) [(V'_{\hat{\rho}})^{5/3} n_s T_s] = \frac{1}{V'_{\hat{\rho}}} \frac{\partial}{\partial \hat{\rho}} \left[\frac{g_1}{V'_{\hat{\rho}}} n_s \chi_s \frac{\partial T_s}{\partial \hat{\rho}} + \frac{5}{2} T_s \Gamma_s g_0 \right] + P_s \quad (2.24)$$

where $T_s(\hat{\rho}, t)$, $n_s(\hat{\rho}, t)$ are the temperatures and densities of the various species, $\chi_s(\hat{\rho}, t)$ is the thermal diffusivity, Γ_s is the convective flux defined below, $g_0(\hat{\rho}, t) = \langle \nabla V \rangle$ and $g_1(\hat{\rho}, t) = \langle |\nabla V|^2 \rangle$ are the geometrical quantities with the plasma volume V , $P_s(\hat{\rho}, t)$ represents the power density as a sum of various sources and sinks.

Thermal diffusivity models

Depending on the goals of a numerical code and its physical conception, various models for the thermal diffusivity of electrons and ions $\chi_{e,i}$ can be used. In the RAPTOR code there is a choice between several models.

Firstly, a well known Bohm/gyro-Bohm model [Erba et al.(1998)] provides heat transport coefficients both for electrons and ions. In [Felici et al.(2012), Felici(2011)] a simple ad-hoc model for the electron heat diffusivity has been presented. This model takes into account a shear-dependent anomalous transport accounting an improved confinement in case of the low and negative magnetic shear as observed in TCV [Zucca et al.(2009)]. Recently, for calculations of the turbulent transport for the plasma energy and particles, a neural-network emulation of the quasilinear gyrokinetic QuaLiKiz transport model [Bourdelle et al.(2016), Citrin et al.(2015)] has been coupled to the RAPTOR code [Felici et al.(2018)].

Another ad-hoc transport model for heat and particle transport based on the assumption of stiffness of the plasma core and non-stiffness of the plasma edge [Sauter et al.(2014), Kim et al.(2016)] has been implemented into RAPTOR as part of this thesis. One of the advantages of this model is a good capability for simulations of plasmas with transitions between low (L) and high (H) confinement modes. Thus, this model is very efficient for an entire shot simulations, and the transport modeling for this thesis has been done with this model. More details are provided in Sec. 2.6.

Power sources and sinks

For electrons the power sources consist of the ohmic heating P_{OH} , the auxiliary external heating $P_{e,aux}$ and the fusion power $P_{e,fus}$. The first one comes from electron-ion collisions, as a result of the plasma resistance to the toroidal current which produces the poloidal magnetic field necessary for a tokamak equilibrium. In RAPTOR the ohmic power is calculated in the following way:

$$P_{OH} = \frac{1}{2\pi R_0} \int_V U_{pl} j_{tor} dV = \frac{1}{2\pi R_0} \int_V \frac{\partial \psi}{\partial t} j_{tor} dV \quad (2.25)$$

2.3. Overview of the transport equations

where U_{pl} denotes the plasma loop voltage, j_{tor} is the toroidal current density, defined in Appendix A. Since electrons are lighter than ions, ohmic heating mainly goes to electrons but part of it nevertheless conducts to ions via thermal electron-ion collisions. Ohmic heating is relatively strong at lower temperatures, but decreases with growth of the electron temperature T_e , since the plasma conductivity $\sigma_{||}$ increases with its temperature as $T_e^{3/2}$.

As it was described in Subsec. 1.2.2, for external heating there are RF power sources (ECRH, ICRH) and neutral beams (NBI). Power deposition profiles can be obtained with special codes like ASTRA-NBI [Polevoi et al.(1997)] and NUBEAM [Pankin et al.(2004)] for NBI, TORBEAM [Poli et al.(2001)] and TORAY-GA [Matsuda et al.(1989)] for EC heating and current drive, PION [Eriksson et al.(1993), Eriksson et al.(1995)] and TORIC [Brambilla et al.(1999)] for IC heating and current drive. Also, if a very high accuracy is not required, parametrized expressions can be used, and power and current densities can be modeled by Gaussian distributions. This approach is usually used for simulations with the RAPTOR code where the radial deposition ρ_{dep} and the Gaussian width are user-defined parameters. For control-oriented purposes, it is useful to model non-inductive current profile sources as parametrized functions of engineering quantities, based on approximate theoretical formulas for current densities [Witrant et al.(2007)]. The last source, the fusion power, as a result of the thermonuclear reaction, will be a major one for ITER D-T plasmas. Therefore, RAPTOR simulations for ITER take this power into account [Felici(2011), van Dongen et al.(2014)].

The main power sinks for electrons are an equipartition power P_{ei} and radiated power P_{rad} . The first one comes from electron-ion interaction and is defined in [Hinton and Hazeltine(1976)] in the following way:

$$P_{ei} = n_e v_{eq} (T_e - T_i) \quad (2.26)$$

where the neoclassical equipartition rate v_{eq} is defined as:

$$v_{eq} = 0.041 T_e^{-3/2} [keV] \sum_{si} n_{si} \frac{Z_{si}^2}{A_{si}} \quad (2.27)$$

Here Z_{si} and A_{si} are charges and atomic mass numbers for various ion species.

The radiation losses for a plasma can be split into two groups: electromagnetic and impurity radiation. Charged particles emit radiation because of acceleration in the electric field. Since electrons are much lighter than ions, they are more accelerated and radiate stronger. Thus in RAPTOR, electromagnetic losses are taken into account for electrons only.

There are two ways of electrons' acceleration. First one comes from collisions and the resulted radiation is called Bremsstrahlung which is the most dominant in existing large tokamaks. The formula for its definition in the RAPTOR code has been taken from [Wesson(2004)]:

$$P_{br} = 5.35 \cdot 10^{-37} Z_{eff} n_e n_i T_e^{1/2} \quad (2.28)$$

Chapter 2. The RAPTOR code: overview and developments

where Z_{eff} is a plasma effective charge, defined in Eq. 2.21, n_e and n_i are electron and ion densities, T_e is the electron temperature.

The second source of the electromagnetic radiation is cyclotron losses because of the cyclotron motion of electrons. This radiation has been found negligible in comparison to Bremsstrahlung [Wesson(2004)] and therefore is not included to P_{rad} for RAPTOR.

Presence of impurities enhances the Bremsstrahlung radiation because of the higher ion charge for impurities. Also there is a radiation related to the atomic process like recombination and so called the line radiation where an emission spectrum consists of multiple emitting lines produced by ionized high- Z impurities [Wesson(2004)]. In RAPTOR we use a simplified formula for the line radiation estimation:

$$P_{at} = \sum_{rp} n_{e0} \exp\left(\frac{(T_{e,rp} - T_e)^2}{w_{rp}^2}\right) \quad (2.29)$$

where n_{e0} is the central electron density; $T_{e,rp}$ is the prescribed electron temperature for a radiation peak “rp”; w_{rp} is the prescribed width of a radiation peak “rp”. This model is tuned for a set concentration of a given impurity with a given charge state, that radiates at a certain temperature.

Note that for simulations, there is also an option to use prescribed radiation profiles constructed with the help of experimental measurements, for example provided by bolometers.

Thus the total power density for electrons is written as:

$$P_e = P_{OH} + P_{e,aux} + P_{e,fus} - P_{ei} - P_{e,rad} \quad (2.30)$$

It can be written in a similar way for ions:

$$P_i = P_{i,aux} + P_{ei} + P_{i,fus} \quad (2.31)$$

2.3.3 The particle transport equation

The particle transport equation is written in the common form for various species “s” as the energy transport equations according to [Hinton and Hazeltine(1976)]:

$$\frac{1}{V'_\rho} \left(\frac{\partial}{\partial t} \Big|_\rho - \frac{\Phi_b}{2\Phi_b} \frac{\partial}{\partial \hat{\rho}} \hat{\rho} \right) [V'_\rho n_s] = -\frac{1}{V'_\rho} \frac{\partial}{\partial \hat{\rho}} \Gamma_s + S_s \quad (2.32)$$

where the particle flux is defined in the following way

$$\Gamma_s = -\frac{g_1}{V'_\rho} D_s \frac{\partial n_s}{\partial \hat{\rho}} + g_0 V_s n_s \quad (2.33)$$

here D_s corresponds to the particle diffusivity, V_s is the pinch velocity, S_s represents a combination of various sources and sinks of particles.

If Eq. 2.32 is solved for electrons and the effective charge profile Z_{eff} is known then densities of main ions and one other type of minor impurities can be calculated from the Z_{eff} definition Eq. 2.21 and the condition of the plasma quasi-neutrality Eq. 2.22. If several types of impurities n_{si} are considered, then from the set of parameters $[n_e, n_i, Z_{eff}, n_{si}]$, two of them can be calculated with the help of the Z_{eff} definition and the condition of the plasma quasi-neutrality, whereas others have to be prescribed by the user.

Transport coefficients for particles

As for the heat diffusivity, there is a wide range of transport models for particles. As it was mentioned earlier the quasilinear gyrokinetic QuaLiKiz transport model [Bourdelle et al.(2016), Citrin et al.(2015)] provides transport coefficients for particles transport. More details can be found in [Felici et al.(2018)]. In this thesis, a transport model similar to the one developed for the electron temperature is used for n_e simulations and described in detail in Sec. 2.6.

Sources and sinks of particles

An important work on the determination of particle sources and sinks has been performed as part of the development of a particle density observer for real-time reconstruction of particle density profiles in tokamak plasmas [Blanken et al.(2018)]. There is some level of uncertainty in the prediction of the particle origin coming from such uncontrolled sources and sinks like the fueling and recycling from the first wall. In particular for electrons, the main source is an ionization of neutrals coming with NBI and pellets. For estimation of produced particle flux, NBI and pellets fueling rates and their deposition profiles are required. Opposite processes, like thermal recombination and wall recycling, are the sinks of electrons. For their modelling, characteristic rates and intensity have to be prescribed.

In this work we do not consider plasma dynamics in presence of electron sources and assume zero flux of electron particles. As a starting point for further studies, for TCV plasmas ASTRA NBI-module [Polevoi et al.(1997)] can be used for prediction of the electron source for RAPTOR. On AUG, a suite of NBI modules provide various information on injected power and particle fluxes from injectors. To keep the high speed of RAPTOR simulations, development of simple modules has to be continued with the help of ASTRA simulations and analysis of experimental data for TCV and AUG tokamaks [Weiland et al.(2017)].

2.3.4 Modelling of MHD instabilities

Modelling of MHD plasma instabilities is an important issue for predictions of the plasma transport and profiles because of their huge impact on the plasma heat and particle transport and confinement. There are two MHD instabilities simulated by the RAPTOR code: sawtooth crashes and neoclassical tearing modes (NTMs).

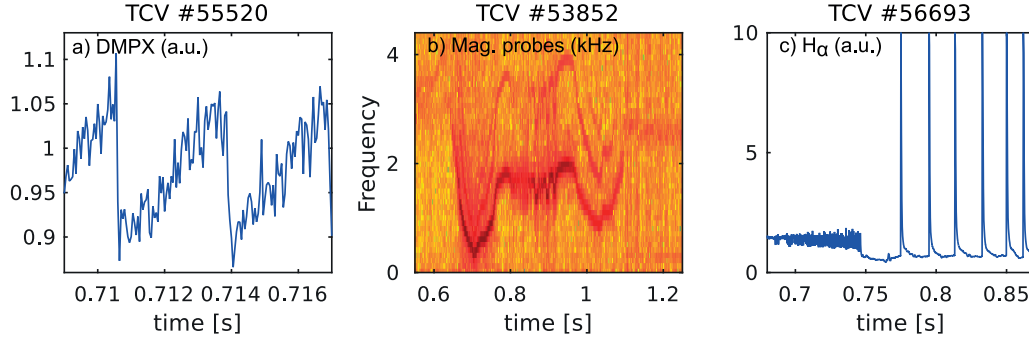


Figure 2.3: MHD instabilities for the TCV tokamak: a) the sawtooth plasma TCV #55520 represented by DMPX measurements; b) NTM $m=2$, $n=1$ TCV #53852 observed with spectrogram of magnetic probe signals; c) ELMs for TCV #53996 observed with the H_α signal.

Sawtooth instability

The central plasma region is characterized by the periodic relaxation (“crashes”) of the plasma temperature and density profiles which occur when the safety factor q is less than or equal to unity [von Goeler et al.(1974)]. These instabilities can be detected measuring the soft X-ray emission by the DMPX diagnostic (Duplex Multiwire Proportional X-ray counter), in TCV for example, described in Subsec. 1.2.3. On Fig. 2.3.a) the sawtooth plasma has crashes with a period of 2.5 ms. Heat and particle transport determine a slow growth of plasma profiles, followed by a decrease in a safety factor q to below unity what leads to growth of an internal kink mode $m = 1$, $n = 1$ instability [von Goeler et al.(1974), Fiedberg(1982), Porcelli et al.(1996)]. Sawtooth crashes do not degrade the plasma confinement since the plasma profiles are affected only within the characteristic mixing radius r_{mix} . This radius constraints a plasma volume, where mixing of plasma particles and energy occur during the MHD event, and it is a bit larger than radius of $q = 1$ surface before the crash. A positive consequence of the sawtooth crashes for a global plasma performance is an outward transport of high-Z impurities, which prevents their accumulation in the core center and therefore increased radiation, what has been observed in experiments on various machines [Ödöblom et al.(1996)] (and references therein). However, this process can lead to destabilization of NTMs [Sauter et al.(2002b), Canal(2013)].

Sawtooth modelling in RAPTOR has been presented and developed in [Piron et al.(2015)]. The sawtooth crash is defined according to the Porcelli crash criteria with Sauter corrections [Porcelli et al.(1996), Sauter et al.(1998)]. In RAPTOR a simplified condition is usually used, where a crash occurs when the plasma shear, defined with Eq. 2.6, becomes bigger than its user-defined critical value [Sauter et al.(1998)]. Plasma profiles are reconstructed after the crash with the Kadomtsev full reconnection model [Kadomtsev(1975)] and the incomplete relaxation model [Porcelli et al.(1996)].

Neoclassical tearing modes

In theory [Strait(1994)] and experiments [Sauter et al.(1997)] (and references therein), it has

been shown that maximum achievable β , in terms of which a tokamak performance can be estimated, is limited by a growth of resistive MHD modes with low m , n numbers. These neoclassical tearing modes (NTMs) cause the reconnection of the nested flux surfaces and form regions of so-called magnetic islands. The temperature and density gradients are strongly reduced inside these islands, leading to a decrease in the bootstrap current with further mode destabilization [Sauter et al.(1997)] and plasma heat and particle confinement degradation. Thus, these modes are unfavorable for tokamak performance and should be suppressed or avoided. Experimentally they can be detected by measuring oscillations in the magnetic field with magnetic probes (Fig. 2.3.b)). These modes can be triggered by a seed island created by another event like a sawtooth crash, or because of an unstable q profile [Reimerdes et al.(2002)].

In the RAPTOR code, for NTMs simulations, we use the modified Rutherford equation which determines the growth of the NTM island width, as was shown in theoretical and experimental studies [Callen et al.(1987), Carrera et al.(1986), Sauter et al.(2002a)]. In this work NTMs are not included to plasma simulations, we leave it for future studies.

Edge localized modes

In the pedestal region, plasmas experience crashes related to collapses in the edge pressure gradients [Ryter et al.(1994)]. These edge localised modes (ELMs) are observed in the plasma high confinement mode (H-mode) and their presence is a good marker to define transitions from the low to high confinement mode and back. ELMs cause rapid spontaneous growth of heat and particle transport at the plasma edge and their rapid exhaust to the scrape-off layer, continuing to the divertor targets. They can be detected with the help of measured emission spectra of hydrogen or fast ions (so called H_α and D_α signals) [Kirk et al.(2004)]. On the TCV tokamak, photo diodes measure the hydrogen light emission. The H-mode is characterized by a drop in the H_α signal and periodic peaks which correspond to ELMs crashes. On Fig. 2.3.c) the plasma turns to the high confinement mode around 0.75 s and a few ELMs crashes can be observed after it. H-modes are characterized by an edge transport barrier leading to high edge pressure gradients which become MHD unstable and trigger ELMs [Snyder et al.(2011)].

We do not simulate these modes in the RAPTOR code but for post-shot modelling the H_α signal has to be analysed to prescribe time instants of transitions between low and high confinement modes.

2.3.5 A fixed geometry assumption

Here we briefly remind the reader that in the transport model used by RAPTOR in the versions up to 2017 a simplified set of transport equations has been used. Initially, for compatibility with real-time execution [Felici et al.(2011)], only two diffusion equations, for ψ and T_e , have been included into it. Such a simplification was justified by the fact that the most important parameters for the plasma state description are the electron temperature T_e and the poloidal flux ψ . Indeed these quantities directly determine the transport properties, hence global

confinement, and the plasma resistivity and the current density profile, which provide the q profile time evolution depending on $T_e(\rho, t)$ as well. It was chosen to use experimental measurements for the electron density, which were much more reliable than a predicted value at this stage. In the first version of the model, described in [Felici et al.(2011)], [Felici et al.(2012)], the transport model used in RAPTOR has been constructed based on a fixed equilibrium assumption. It was supposed that the magnetic field B_0 , the geometry of flux surfaces and the enclosed toroidal flux Φ were fixed. This assumption was weaker than the condition of a fixed Grad-Shafranov equilibrium, since in RAPTOR, the poloidal flux profile $\psi(\rho)$ and therefore the current density $j_{tor}(\rho)$ and the safety factor $q(\rho)$ could evolve in time. In [Felici et al.(2011)] it was shown that the geometry profiles do not change a lot with the Shafranov shift. The transport equations for ψ and T_e in case of a fixed equilibrium and the electron density assumption have the following form:

- The poloidal flux equation

$$\sigma_{\parallel} \left. \frac{\partial \psi}{\partial t} \right|_{\hat{\rho}} = \frac{F^2}{16\pi^2 \mu_0 \Phi_b^2 \hat{\rho}} \frac{\partial}{\partial \hat{\rho}} \left[\frac{g_2 g_3}{\hat{\rho}} \frac{\partial \psi}{\partial \hat{\rho}} \right] - \frac{B_0}{2\Phi_b \hat{\rho}} V'_{\hat{\rho}} j_{ni} \quad (2.34)$$

- The electron temperature equation

$$\frac{3}{2} n_e \left. \frac{\partial T_e}{\partial t} \right|_{\hat{\rho}} = \frac{1}{V'_{\hat{\rho}}} \frac{\partial}{\partial \hat{\rho}} \left[\frac{g_1}{V'_{\hat{\rho}}} n_e \chi_e \frac{\partial T_e}{\partial \hat{\rho}} \right] + P_e \quad (2.35)$$

In this case, other kinetic parameters like the electron density n_e , the ion temperature T_i and the ion density n_i , are prescribed and either analytical profiles or experimental data can be used for their description during the simulation. Note that in Eqs. 2.34 and 2.35 the geometrical and kinetic profiles $V'_{\hat{\rho}}$, $n_e(\hat{\rho})$ and etc are fixed in time. Recently and as part of this thesis, transport equations have been extended to allow time-evolving plasma equilibria as described in details in Sec. 2.4.

2.3.6 RAPTOR transport equations summary

To summarize, here we present a set of transport equations important for this thesis including new developments [Felici et al.(2018), Teplukhina et al.(2017)]:

- The poloidal flux diffusion equation

$$\sigma_{\parallel} \left(\left. \frac{\partial \psi}{\partial t} \right|_{\hat{\rho}} - \frac{\hat{\rho} \dot{\Phi}_b}{2\Phi_b} \frac{\partial \psi}{\partial \hat{\rho}} \right) = \frac{F^2}{16\pi^2 \mu_0 \Phi_b^2 \hat{\rho}} \frac{\partial}{\partial \hat{\rho}} \left[\frac{g_2 g_3}{\hat{\rho}} \frac{\partial \psi}{\partial \hat{\rho}} \right] - \frac{B_0}{2\Phi_b \hat{\rho}} V'_{\hat{\rho}} j_{ni} \quad (2.36)$$

- The electron temperature diffusion equation

$$\frac{3}{2} \frac{1}{(V'_\rho)^{5/3}} \left(\frac{\partial}{\partial t} \Big|_{\hat{\rho}} - \frac{\dot{\Phi}_b}{2\Phi_b} \frac{\partial}{\partial \hat{\rho}} \hat{\rho} \right) [(V'_\rho)^{5/3} n_e T_e] = \frac{1}{V'_\rho} \frac{\partial}{\partial \hat{\rho}} \left[\frac{g_1}{V'_\rho} n_e \chi_e \frac{\partial T_e}{\partial \hat{\rho}} + \frac{5}{2} T_e \Gamma_e g_0 \right] + P_e \quad (2.37)$$

- The electron density diffusion equation

$$\frac{1}{V'_\rho} \left(\frac{\partial}{\partial t} \Big|_{\hat{\rho}} - \frac{\dot{\Phi}_b}{2\Phi_b} \frac{\partial}{\partial \hat{\rho}} \hat{\rho} \right) [V'_\rho n_e] = -\frac{1}{V'_\rho} \frac{\partial}{\partial \hat{\rho}} \Gamma_e + S_e \quad (2.38)$$

where the particle flux Γ_e is defined in the following way

$$\Gamma_e = -\frac{g_1}{V'_\rho} D_e \frac{\partial n_e}{\partial \hat{\rho}} + g_0 V_e n_e \quad (2.39)$$

- The ion temperature diffusion equation

$$\frac{3}{2} \frac{1}{(V'_\rho)^{5/3}} \left(\frac{\partial}{\partial t} \Big|_{\hat{\rho}} - \frac{\dot{\Phi}_b}{2\Phi_b} \frac{\partial}{\partial \hat{\rho}} \hat{\rho} \right) [(V'_\rho)^{5/3} n_i T_i] = \frac{1}{V'_\rho} \frac{\partial}{\partial \hat{\rho}} \left[\frac{g_1}{V'_\rho} n_i \chi_i \frac{\partial T_i}{\partial \hat{\rho}} + \frac{5}{2} T_i \Gamma_e g_0 \right] + P_i \quad (2.40)$$

where $V'_\rho = \partial V / \partial \hat{\rho}$, V is the plasma volume, Φ_b is the toroidal flux within the last closed flux surface; geometrical parameters $g_0 = \langle \nabla V \rangle$, $g_1 = \langle (\nabla V)^2 \rangle$, $g_2 = \langle \frac{(\nabla V)^2}{R^2} \rangle$, $g_3 = \langle \frac{1}{R^2} \rangle$; $F = RB_\phi$ is the poloidal current function; $P_{e,i}$ and S_e are the heat and particle sources/sinks; $\chi_{e,i}$, D_e and V_e are the transport coefficients. Below we shortly describe the numerical method used for RAPTOR simulations.

Boundary conditions

We set the boundary conditions at $\hat{\rho} = 0$ in the following way:

$$\frac{\partial \psi}{\partial \hat{\rho}} \Big|_{\hat{\rho}=0} = \frac{\partial T_e}{\partial \hat{\rho}} \Big|_{\hat{\rho}=0} = \frac{\partial n_e}{\partial \hat{\rho}} \Big|_{\hat{\rho}=0} = \frac{\partial T_i}{\partial \hat{\rho}} \Big|_{\hat{\rho}=0} = 0 \quad (2.41)$$

At the plasma edge, we set the time-varying Neumann boundary condition for the poloidal flux $\psi(\hat{\rho}, t)$. For this parameter, the total plasma current $I_p(t)$ can be imposed as a boundary condition, analytical derivation is described in Appendix B. For the electron temperature $T_e(\hat{\rho}, t)$, electron density $n_e(\hat{\rho}, t)$ and ion temperature $T_i(\hat{\rho}, t)$, we use Dirichlet boundary

conditions. Their values are prescribed and can be fixed or time-varying.

$$\psi|_{\hat{\rho}=\rho_b} = \frac{16\pi^3\mu_0\Phi_b}{F} \Big|_{\hat{\rho}=\rho_b} I_p \quad (2.42)$$

$$T_e|_{\hat{\rho}=\rho_b} = T_{eb}(t) \quad (2.43)$$

$$n_e|_{\hat{\rho}=\rho_b} = n_{eb}(t) \quad (2.44)$$

$$T_i|_{\hat{\rho}=\rho_b} = T_{ib}(t) \quad (2.45)$$

Spatial discretization

The RAPTOR code uses the finite element method for the discretization of infinite-dimensional Eqs. 2.36-2.40. There are several advantages of this method, like a flexible choice of basis functions, a natural implementation of a non-equidistant mesh and of the boundary conditions and a reduction of the order of spatial derivatives through integration by parts. We approximate plasma state profiles in the following way:

$$m(\hat{\rho}, t) = \sum_{\alpha=1}^{n_{sp}} \Lambda_{\alpha}(\hat{\rho}) \hat{m}_{\alpha}(t) \quad (2.46)$$

where $m(\hat{\rho}, t)$ corresponds to $\psi(\hat{\rho}, t)$, $T_e(\hat{\rho}, t)$, $n_e(\hat{\rho}, t)$ or any other plasma profile; $\Lambda(\hat{\rho})$ are the finite element basis functions and are chosen as nonperiodic B-splines; \hat{m} is the spline coefficient vector; n_{sp} denotes the number of splines. To guarantee continuity up to the second derivative, and consequently to ensure continuity of current densities and the magnetic shear, we use cubic splines. The set of basis functions is furthermore chosen such that all elements have zero derivatives at $\rho = 0$, thus, the solutions automatically satisfy the Neumann boundary conditions in Eq. 2.41.

The continuous-time transport equations are discretized in time by choosing

$$x_{k+1} = x_k + \delta t \dot{x}(t) \quad (2.47)$$

$$x(t) = \theta x_{k+1} + (1 - \theta) x_k \quad (2.48)$$

Varying θ between 1 and 0 allows one to vary between a fully implicit and fully explicit method. We choose a fully implicit method $\theta = 1$, thus the time step can be taken quite large without risking numerical stability problems.

More details can be found in Appendix B and in the papers [Felici(2011), Felici et al.(2011), Felici et al.(2012), Teplukhina et al.(2017), Felici et al.(2018)] related to the RAPTOR code.

2.4 Code development: time-varying geometry

This section is dedicated to the first stage of the code development, carried out as part of this thesis. Thus, a reader can assume that the transport equations have been prescribed as in Eqs. 2.34-2.35. Time evolution of the plasma equilibrium geometry influences the plasma profiles and have to be taken into account in the case of simulations of entire discharges, where significant changes in the plasma state occur during ramp-up and ramp-down phases, in particular, including fast evolution of the plasma boundary.

2.4.1 Extension of the transport equations for the time-varying equilibrium

The simplified diffusion equations 2.34 and 2.35 have been extended with the time-varying terms as stated in equations 2.36 and 2.37. The parameters related to equilibrium geometry are defined through a linear interpolation of several equilibria corresponding to different time instants. The kinetic profiles $n_e(\hat{\rho}, t)$, $T_i(\hat{\rho}, t)$, etc. and geometrical quantities $V'_\rho(\hat{\rho}, t)$, $g_1(\hat{\rho}, t)$, etc are now both space- and time-varying. Since the solution method used in RAPTOR is based on the finite-element approach, these equations can be easily extended to include new terms. See [Teplukhina et al.(2017)] and Appendix B for more details of the implementation of the time-varying terms in the code. Here the updated equations are presented:

- The poloidal flux equation

$$\sigma_{\parallel} \left(\frac{\partial \psi}{\partial t} \Big|_{\hat{\rho}} - \frac{\hat{\rho} \dot{\Phi}_b}{2\Phi_b} \frac{\partial \psi}{\partial \hat{\rho}} \right) = \frac{F^2}{16\pi^2 \mu_0 \Phi_b^2 \hat{\rho}} \frac{\partial}{\partial \hat{\rho}} \left[\frac{g_2 g_3}{\hat{\rho}} \frac{\partial \psi}{\partial \hat{\rho}} \right] - \frac{B_0}{2\Phi_b \hat{\rho}} V'_\rho j_{ni} \quad (2.49)$$

- The electron temperature equation

$$\frac{3}{2} \frac{1}{(V'_\rho)^{5/3}} \left(\frac{\partial}{\partial t} \Big|_{\hat{\rho}} - \frac{\dot{\Phi}_b}{2\Phi_b} \frac{\partial}{\partial \hat{\rho}} \hat{\rho} \right) [(V'_\rho)^{5/3} n_e T_e] = \frac{1}{V'_\rho} \frac{\partial}{\partial \hat{\rho}} \left[\frac{g_1}{V'_\rho} n_e \chi_e \frac{\partial T_e}{\partial \hat{\rho}} \right] + P_e \quad (2.50)$$

In contrast to Eqs. 2.34-2.35, there are time-varying terms related to the toroidal flux Φ_b , thus to the plasma equilibrium. The code had to be changed extensively since not only new terms related to $\dot{\Phi}_b$ have been added, but also related to $\partial n_e / \partial t$ and $\partial V'_\rho / \partial t$. In addition, RAPTOR computes analytically Jacobians related to the plasma state. To take into account time-varying geometry and density, new derivatives have been implemented in the code.

2.4.2 Verification with the ASTRA code

Benchmark with the ASTRA code [Pereverzev and Yushmanov(2002)] has been performed to verify the code extension with the time-varying terms.

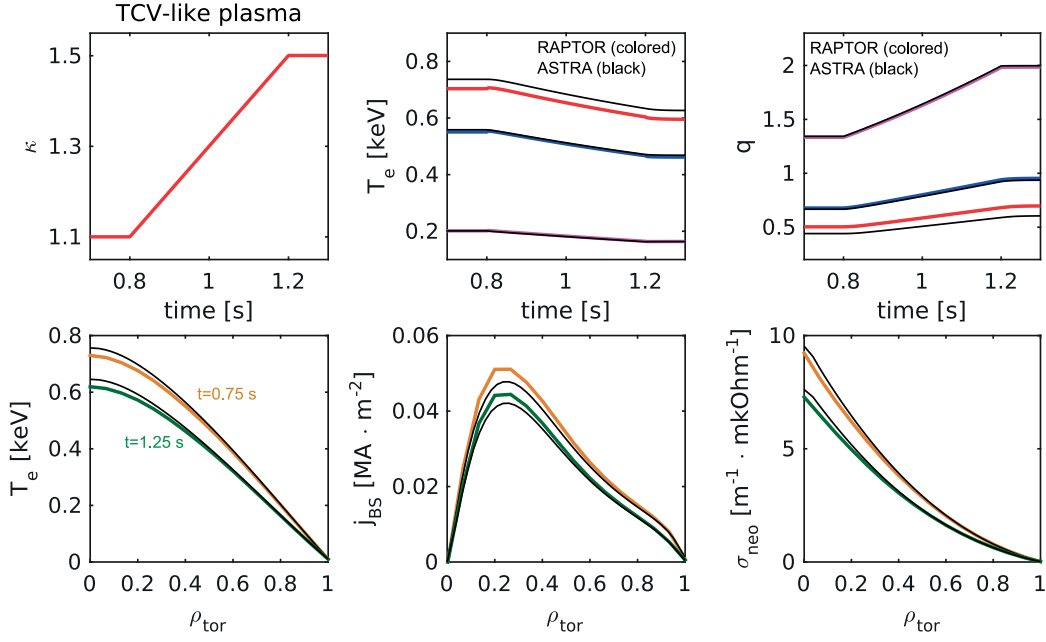


Figure 2.4: Benchmark of RAPTOR and ASTRA simulation results for the TCV-like ohmic plasma with time-varying plasma geometry. The first row: time evolution of the electron temperature T_e and the safety factor q at radial positions $\rho_{tor} = [0.1, 0.4, 0.8]$ in case of the time-varying plasma boundary elongation κ for RAPTOR (colored) and ASTRA (black). The second row: radial profiles for the electron temperature T_e , the bootstrap current density j_{BS} and the neoclassical conductivity σ_{neo} at time instants $t=0.75$ s (yellow) and $t=1.25$ s (green), where RAPTOR traces are marked by colored lines, ASTRA traces are in black.

The ASTRA code

The transport code ASTRA (Automated System for Transport Analysis) is the well-known code used for plasma transport modeling [Pereverzev and Yushmanov(2002)]. It is a 1.5D code which solves 1D diffusion equations for densities and temperatures of different plasma species and the 2D fixed-equilibrium Grad-Shafranov equilibrium equation. It also provides various modules for simulations of auxiliary heating profiles and current drive profiles. The transport model can include the transport equations for the poloidal flux ψ , the electron T_e and ion T_i temperatures, the electron density n_e and other species.

Simulations verification

For the benchmark, an artificial TCV-like plasma geometry has been simulated. The Grad-Shafranov equation has been solved by the ASTRA's internal prescribed-boundary equilibrium solver and then the equilibrium data has been processed by the CHEASE code [Lütjens et al.(1996)] to generate the equilibrium geometry information as input for RAPTOR. Both ASTRA and RAPTOR solve the diffusion equations for the poloidal flux ψ and the electron temperature T_e . Profiles for $n_e(\hat{\rho}, t)$, $n_i(\hat{\rho}, t)$, $T_i(\hat{\rho}, t)$ have been defined as Gaussian

profiles, centered at $\hat{\rho} = 0$ with widths equal to 0.3, and fixed in time. The electron heat diffusivity $\chi_e(\hat{\rho}, t)$ has been determined as a square function of the radial coordinate only. Figure 2.4 shows the results of the simulation in case when the elongation of the plasma boundary has been increased from 1.1 to 1.5 in 800 ms. A decrease of the electron temperature T_e and growth of the safety factor q are expected and obtained with both codes which results are similar. There is a good correspondence for various radial profiles, in particular in the electron temperature T_e , the bootstrap current density j_{BS} and the neoclassical conductivity $\sigma_{||}$. Small differences between RAPTOR and ASTRA for j_{BS} and σ_{neo} radial profiles might arise from numerical processing of the equilibrium data, since the plasma trapped fraction and plasma collisionality used for calculation of j_{BS} and σ_{neo} depend on q and geometrical parameters.

2.5 Code development: additional transport equations

Next step in the code development is related to implementation of the additional transport equations, in particular for the electron density n_e and other particles, and the ion temperature T_i .

Prescribed data from the ITER particle transport benchmark [Na et al.(2016)] are used for verification of the n_e transport equation. Eq. 2.38 is coupled with Eqs. 2.36 and 2.37, but data from [Na et al.(2016)] are specified only for particle transport. Hence in this simulation the n_e equation is entirely decoupled from the other equations, since the D_e , V_e terms are manually specified. The ITER plasma at one time instant is considered, therefore simulations are done for a fixed equilibrium. There are three types of impurities: helium (He), beryllium (Be) and argon (Ar). Radial profiles for Be and Ar are scaled from n_e , i.e. same transport characteristics are assumed for electrons and impurities, and the radial profile of He is prescribed. The diffusion equation Eq. 2.38 is solved for the electron density n_e . Thus, for particle transport there are 6 characteristic parameters (n_e , n_i , n_{He} , n_{Be} , n_{Ar} , Z_{eff}) and four of them are known. Therefore, the ion density n_i is calculated from the quasi-neutrality condition Eq. 2.22 and the effective charge Z_{eff} is determined according to its definition Eq. 2.21. Here, by ions we assume deuterium ions with charge 1 and an atomic mass 2. As shown in Fig. 2.5, there is very good agreement for particle densities and Z_{eff} between RAPTOR and the benchmark data. The diffusion coefficient D_e , the pinch velocity V_p and the particle source S_e for the n_e diffusion equation are prescribed and shown in the second row in Fig. 2.5. Equilibrium data processing might lead to some difference in particle radial profiles, however the pedestal height predicted by RAPTOR is very close to the reference.

Also simultaneous prediction of the electron T_e and ion T_i temperatures and the electron density n_e , defined with Eqs. 2.36-2.40, has been done for a JET discharge [Felici et al.(2018)]. Obtained plasma profiles have shown a good agreement with simulation results provided by the CRONOS transport code [Artaud et al.(2010)], using the same transport model.

With these benchmarks we confirm that the transport equations Eqs. 2.36-2.40 are solved correctly in the RAPTOR code.

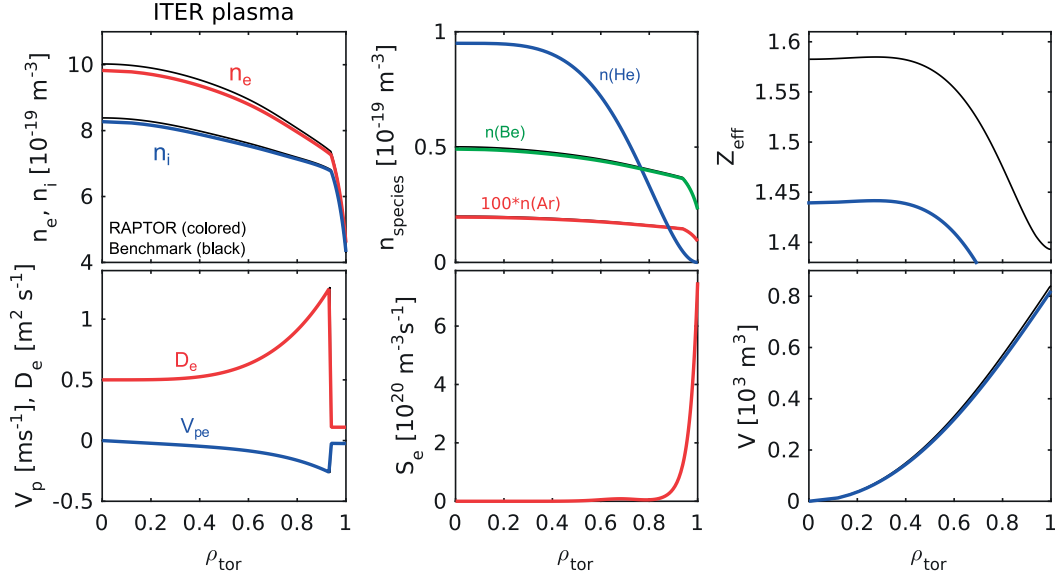


Figure 2.5: Particle transport benchmark of RAPTOR and reference data for ITER plasma at the fixed time instant. Profiles for the electron density n_e , ion density n_i , impurities $n_{He/Be/Ar}$, an effective charge Z_{eff} prescribed by RAPTOR (colored lines) are in a good agreement with their reference values. Transport parameters D_e and V_p are prescribed from ITER data as well as the plasma equilibrium (the radial profile for the plasma volume V is shown).

2.6 Code development: the gradient-based transport model

In this section we present the ad-hoc gradient-based transport model for heat and particle transport implemented into the RAPTOR code as part of this thesis. The transport coefficients are radially dependent and are constructed on the normalized toroidal grid $\hat{\rho}$. We distinguish between three regions: the central region between 0 and $\hat{\rho}_{inv}$ which is defined as a radial coordinate of the $q = 1$ surface; the intermediate region between $\hat{\rho}_{inv}$ and the pedestal position $\hat{\rho}_{ped}$; the edge (pedestal) region between $\hat{\rho}_{ped}$ and 1. In [Garbet et al.(2004)], it was shown that we can assume the intermediate region to be “stiff” as a consequence of the observed resistance of electron temperature profiles to increase their peaking with growth in the central heating. In [Sauter et al.(2014)] the normalized inverse scale length R/L_{Te} has been defined in the pedestal region, which has been determined for an L-mode plasma too. In Fig. 2.6.a) we show a typical profile of R/L_{Te} for the electron temperature defined in the following way:

$$\frac{R}{L_{Te}} = -\frac{R_0}{a} \frac{d \ln T_e}{d \rho_V} = \begin{cases} 0 & \text{for } 0 < \rho_V < \rho_{inv, Te} \\ \frac{R_0}{a} \lambda_{Te} & \text{for } \rho_{inv, Te} < \rho_V < \rho_{ped, Te} \\ \frac{R_0}{a} \frac{\mu_{Te}}{T_e(\rho_V)} & \text{for } \rho_{ped, Te} < \rho_V < 1 \end{cases} \quad (2.51)$$

Thus we have the central region with $R/L_{Te} = 0$, the intermediate “stiff” region with fixed R/L_{Te}

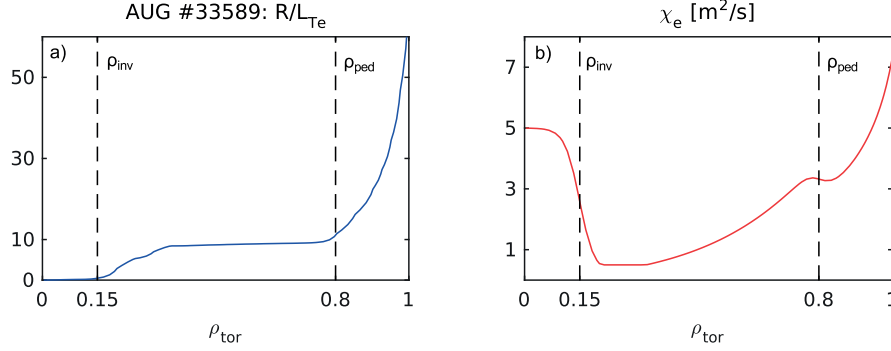


Figure 2.6: L-mode AUG #33589 at 0.5 s: a) the normalized inverse scale length radial profile R/L_{T_e} ; b) the radial profile of the electron heat diffusivity χ_e .

which is characterized by the constant logarithmic gradient $\lambda_{T_e} = -T_e^{-1} \partial T_e / \partial(\rho / \rho_{edge})$, and the edge “non-stiff” region with the characteristic gradient $\mu_{T_e} = -\partial T_e / \partial(\rho / \rho_{edge})$. For the electron density the inverse scale length can be defined in a similar way. It was demonstrated in [Sauter et al.(2014)] that, for a wide range of TCV scenarios, values of λ_σ ($\sigma = T_e, n_e$) are close to each other, whereas μ_σ reflects changes in thermal and particle transport and confinement.

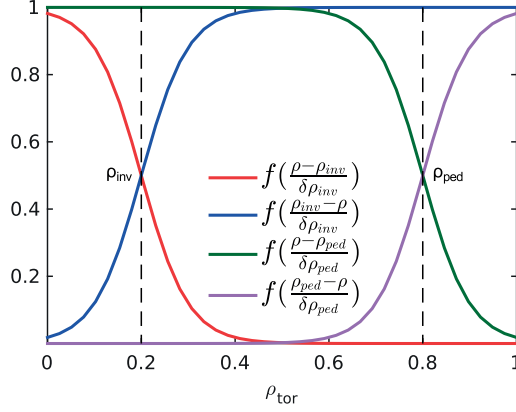
The model, described in detail below, has been developed to be very simple and fast to keep a high speed of simulations. It depends only on a few characteristics which can be easily related to experimental measurements and thus checked or identified in real-time, like the H factor relating the experimental or predicted global confinement time to a given scaling law and the expected profile of inverse scale length in the core plasma region. The profiles for T_e , n_e and T_i are simulated up to $\hat{\rho} = 1$, i.e. transport in the pedestal area is taken into account. The model prescribes realistic transport for L-/H-modes, thus can be used for the entire shot simulations and for the ramp-down simulations in particular. Note that at this stage we do not consider an effect on plasma profiles from the internal transport barriers (ITBs) [Wolf(2003)] (and references therein).

2.6.1 The gradient-based electron heat diffusivity

The empirical formula for the gradient-based electron heat diffusivity χ_e was first defined and used in [Kim et al.(2016)] and is given by:

$$\chi_e(\hat{\rho}, t) = \underbrace{f\left(\frac{\hat{\rho} - \rho_{inv}}{\delta \rho_{inv}}\right)}_{(a)} \chi_{ST} + f\left(\frac{\rho_{inv} - \hat{\rho}}{\delta \rho_{inv}}\right) \frac{q_e}{V'_\rho \langle (\nabla \hat{\rho})^2 \rangle n_e T_e} \quad (2.52)$$

$$\times \left[\underbrace{\frac{\lambda_{T_e}}{\rho_{edge}} f\left(\frac{\hat{\rho} - \rho_{ped}}{\delta \rho_{ped}}\right)}_{(b)} + \underbrace{\frac{\mu_{T_e}}{T_e \rho_{edge}} f\left(\frac{\rho_{ped} - \hat{\rho}}{\delta \rho_{ped}}\right)}_{(c)} \right]^{-1}$$


 Figure 2.7: f -functions for the χ_e formula.

where ρ_{inv} is the sawtooth inversion radius which can be approximated by the $q = 1$ surface, ρ_{ped} is the pedestal position, $\delta\rho_{inv,ped}$ are the widths of the transition areas (center to core, core to edge), respectively using $f(x) = 1/(1 + \exp(x))$ and $f \sim 1$ if $x < 0$ and $|x| \gg 1$ and $f \sim 0$ if $x > 0$ and $|x| \gg 1$. Corresponding f -functions are presented in Fig. 2.7.

This equation has been derived for a plasma in the stationary state, i.e. the left-hand side of Eq. 2.36 equals zero, neglecting the electron heat flux Γ_e :

$$0 = \frac{1}{V'_\rho} \frac{\partial}{\partial \rho} \left[\frac{g_1}{V'_\rho} n_e \chi_e \frac{\partial T_e}{\partial \rho} \right] + P_e \quad (2.53)$$

Thus, after integration over the plasma volume, the diffusion coefficient χ_e is defined via the heat flux q_e :

$$\chi_e = -\frac{q_e V'_\rho}{n_e g_1} \left[\frac{\partial T_e}{\partial \rho} \right]^{-1} = -\frac{q_e}{n_e V'_\rho \langle (\nabla \rho)^2 \rangle} \left[\frac{\partial T_e}{\partial \rho} \right]^{-1} \quad (2.54)$$

where $g_1 = \langle |\nabla V|^2 \rangle$, the last term $\left[\frac{\partial T_e}{\partial \rho} \right]^{-1}$ has to be rewritten with definitions for λ_{T_e} and μ_{T_e} from Eq. 2.51.

In this way the term (a) of Eq. (2.52) corresponds to the flat profile in the central region to take into account the influence of plasma sawtoothing on electron temperature profiles, the term (b) to the constant inverse scale length R/L_{T_e} defined by λ_{T_e} in the core and the term (c) to the linear gradient μ_{T_e} in the edge. A typical χ_e radial profile is demonstrated in Fig. 2.6.b). We limit χ_e with its neoclassical value around $0.5 \text{ [m}^2/\text{s]}$.

Setting the model parameters

An essentially constant λ_{T_e} can be specified for a machine/scenario and then μ_{T_e} is automatically adjusted to match the correct predicted energy confinement time ratio for elec-

2.6. Code development: the gradient-based transport model

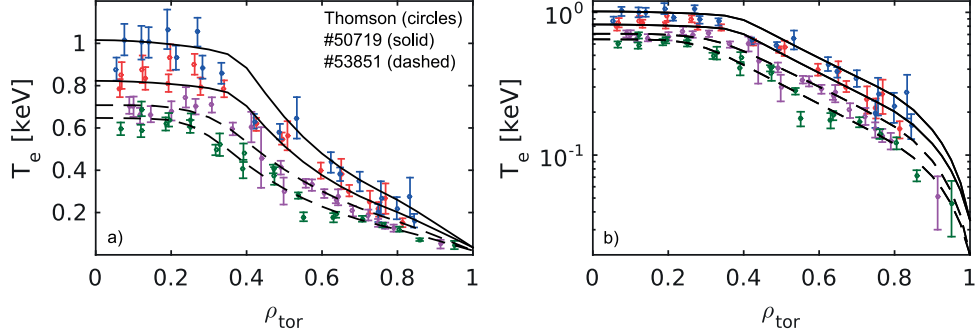


Figure 2.8: T_e ((a) linear plot, (b) log plot) simulated profiles by RAPTOR vs the experimental ones provided by Thomson measurements (circles) for the TCV shots #50719 (solid) and #53851 (dashed): ● – #50719 Ip=195 kA, ● – #50719 Ip=206 kA, ● – #53851 Ip=205 kA, ● – #53851 Ip=185 kA.

trons $H_e = \tau_{E,e}/\tau_{scl}$ [Kim et al.(2016)], where τ_{scl} is calculated with the $H_{98,y,2}$ scaling law [ITER Physics Expert Groups(1999a)] (but other scaling laws can be used). Figure 2.8 shows simulated and experimental radial profiles of the electron temperature for the TCV discharges #50719 and #53851. Simulations have been performed with fixed gradient for the core region $\lambda_{T_e} = 3.2$ and $H_e = 0.4$. Figure 2.8 shows a very good agreement with the experimental profiles. In [Kim et al.(2016)] at each time step the characteristic gradient μ_{T_e} was calculated in the following way:

$$\mu_{T_e}^n = \mu_{T_e}^{n-1} \left\langle \frac{\tau_{scl} H_e^{ref}}{\tau_{E,e}} \right\rangle_{time} \quad (2.55)$$

where n and $n-1$ represent the values of the gradient at the current and previous time steps and $\tau_{E,e}$ is the electron energy confinement time defined as follows:

$$\tau_{E,e} = \frac{W_e}{P_{loss}} = \frac{W_e}{P_{aux} - dW/dt} \quad (2.56)$$

here W and W_e are the total and electron thermal energies correspondingly. If, for example, the estimated $H_e^{n-1} = \tau_{E,e}^{n-1}/\tau_{scl}^{n-1}$ factor is lower than the prescribed one H_e^{ref} , μ_{T_e} will be increased, hence the pedestal top as well, and as a result the whole electron temperature profile will be pushed up to match the desirable H_e value. In Eq. 2.55, averaging over time is performed on a characteristic time period (around 10-15 confinement times) to avoid spurious oscillations. This approach assumes slow variation of H_e during the simulation. In case of large and fast changes in the prescribed H_e , the effect on the electron temperature profiles is delayed because of the time averaging of μ_{T_e} . For a correct simulation of L- to H-mode and H- to L-mode transitions, plasma profiles should react quite rapidly to changes in H_e . Therefore in this work, the gradient μ_{T_e} is calculated with the help of a feedforward and feedback controller, implemented as part of the transport model, based on a ratio of simulated

and prescribed values of H_e .

$$\mu_{T_e}(t) = \underbrace{\mu_{T_e}^{ff}(I_p(t), P_{tot}(t), n_{ei}(t))}_{\text{feedforward}} + \underbrace{K_p \cdot e(t) + K_i \cdot \int^{\delta t} e(t) dt}_{\text{feedback}} \quad (2.57)$$

where K_p and K_i are the proportional and integrated gains for the PI controller, an error $e(t)$ is defined in this way

$$e(t) = H_e^{ref} - H_e^{sim} = H_e^{ref} - \frac{\tau_{E,e}}{\tau_{scl}} \quad (2.58)$$

Discussion of the controller and more details can be found in Appendix C.

Note that the transition between L- and H-modes is modeled here through the time evolution of the value of the pedestal position ρ_{ped} and the gradient in the edge region, μ_{T_e} , thus of the position and value of the top of the pedestal, which then result in a change of the whole profile to match the related expected thermal energy. This is effectively what happens experimentally since the transport near the edge is the main rapid change from L- to H- transition and vice versa. The only main part which is not specified by the model is the time rate of the L-H or H-L transitions. We have used typical values observed in TCV, AUG and JET, but a specific study would be required in order to better predict ITER cases for example. There are two ways to define transition time instant. The first one is to analyse H_α signal, as it was mentioned in Subsec. 2.3.4. The second one is to compare the input power level with the power calculated with the scaling law for the power required for a transition to H-mode [Martin et al.(2008)]:

$$P_{LH}^{scl} = 2.15 e^{0.107} n_{e20}^{0.782} B_T^{0.772} a^{0.975} R^{0.999} \quad (2.59)$$

Note that this scaling law has been developed for transitions from L- to H-mode but because of the absence of an analytical scaling law for the back transition, we use it for L-H and H-L transitions, assuming no hysteresis.

2.6.2 The gradient-based transport coefficients for electrons

We know that the particle confinement time for electrons is relatively long, up to five to ten times as long as the energy confinement time [Becker(1988)]. Thus, in this work the electrons' diffusivity is scaled proportionally to the electron heat diffusivity:

$$D_e = 0.2 \chi_e \quad (2.60)$$

According to the particle flux definition in Eq. 2.33, a model for the pinch velocity is required. In [Kim et al.(2016)] an empirical formula, similar to the gradient-based electron heat diffusivity

2.6. Code development: the gradient-based transport model

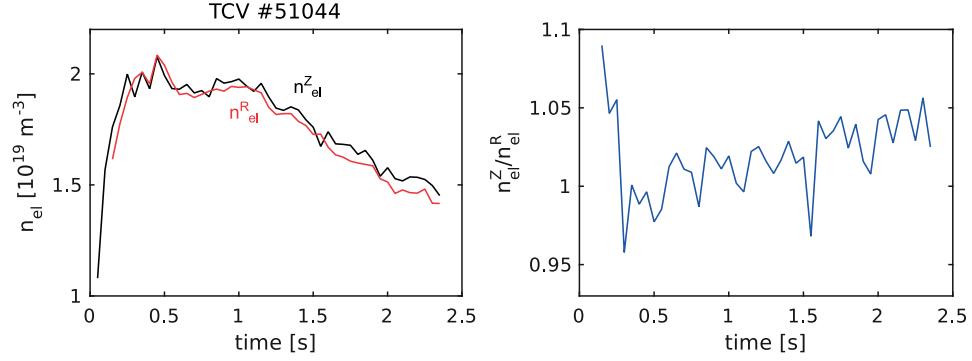


Figure 2.9: Comparison of the line-averaged density n_{el}^Z from the TCV database for the TCV shot #51044 and n_{el}^R calculated from Thomson measurements of the electron density fitted to the normalized toroidal grid.

χ_e , was derived for the ratio V_e/D_e and is given by:

$$\frac{V_e}{D_e} = -f \left(\frac{\rho_{inv} - \rho}{\delta \rho_{inv}} \right) \left[\frac{\lambda_{n_e}}{\rho_{edge}} f \left(\frac{\rho - \rho_{ped}}{\delta \rho_{ped}} \right) + \frac{\mu_{n_e}}{n_e \rho_{edge}} f \left(\frac{\rho_{ped} - \rho}{\delta \rho_{ped}} \right) \right]^{-1} + \frac{\Gamma_e}{n_e V' \langle (\nabla \rho)^2 \rangle} \frac{1}{D_e} \quad (2.61)$$

where the latter term can be neglected in absence of the strong particle sources. In this work, for the first tests of the transport model for electrons, we assume zero particle flux Γ_e and leave modelling of Γ_e for further studies.

The parameter λ_{n_e} has to be specified for a machine and/or a confinement mode in the similar way as for the electron heat diffusivity. The controlled parameter μ_{n_e} is calculated according to the requested line-averaged electron density n_{el} . For the post-shot analysis experimental time-varying n_{el} can be used as a prescribed parameter.

$$\mu_{n_e}(t) = K_p \cdot e(t) + K_i \cdot \int^{\delta t} e(t) dt \quad (2.62)$$

where an error $e(t) = n_{el}^{ref} - n_{el}^{sim}$.

The line-averaged density n_{el}^{sim} , calculated by RAPTOR, is defined in the following way:

$$n_{el}^R(t) = \frac{\int_{\hat{\rho}} n_e(\hat{\rho}, t) d\hat{\rho}}{\int d\hat{\rho}} = \int_{\hat{\rho}} n_e(\hat{\rho}, t) d\hat{\rho} \quad (2.63)$$

On tokamaks an integrated value of the electron density is known from its measurements along the interferometer chords [Ma et al.(1982)]. Therefore, generally the line-averaged density is defined as the electron density averaged over an interferometry chord passing through the

plasma axis Z , i.e. n_{el}^Z :

$$n_{el}^Z = \frac{\int n_e(Z) dZ}{\int dZ} = \frac{\int n_e(\hat{\rho}(Z)) \frac{dZ}{d\hat{\rho}} d\hat{\rho}}{\int \frac{dZ}{d\hat{\rho}} d\hat{\rho}} \quad (2.64)$$

where $\hat{\rho}(Z)$ and $dZ/d\hat{\rho}$ can be defined from the CHEASE code, for example. Since RAPTOR n_e profiles are averaged over $\hat{\rho}$ n_{el}^R might be different to n_{el}^Z . A simple test has been done for the TCV shot #51044. We compare the line-averaged density from the TCV database n_{el}^Z with n_{el}^R , calculated from Thomson n_e profiles fitted on the normalized toroidal grid. From Fig. 2.9 it is clear that a difference of 5% can be expected. In this thesis, we assume $n_{el}^R = n_{el}^Z$, since more detailed studies are required for TCV, AUG and JET plasmas in L- and H- modes. Thus, in the following simulations in Chapter 3, the reference line-averaged density n_{el}^{ref} , required by the transport model, is defined as n_{el}^Z from a machine database.

We assume the same position for ρ_{inv} and ρ_{ped} for n_e and for T_e . Note that experimentally some differences can be observed for ρ_{inv} [Sauter et al.(2014)] and ρ_{ped} [Dunne et al.(2012), Pitzschke et al.(2012)]. The pedestal position in the transport model can be easily specified separately for the electron temperature and the electron density.

2.6.3 The gradient-based ion heat diffusivity model

In [Sauter et al.(2014)] and [Kim et al.(2016)] transport coefficients for electrons only have been considered. However, a similar model can be applied for the ion heat transport as a simple test of the model capabilities. In this case the parameter μ_{T_e} is controlled based on the total confinement factor H instead of the confinement factor for electrons only, i.e. the error in Eq. 2.57 is defined in the following way:

$$e(t) = H^{ref} - H^{sim} = H^{ref} - \frac{\tau_E}{\tau_{scl}} \quad (2.65)$$

where

$$\tau_E = \frac{W_{tot}}{P_{aux} - dW/dt} = \frac{W_e + W_i}{P_{aux} - dW/dt} \quad (2.66)$$

From μ_{T_e} and a given ratio of the pedestal temperatures of electron and ions we can get the parameter μ_{T_i} :

$$\mu_{T_i} = \frac{\mu_{T_e}}{f} + \frac{T_e^{BC} - f \cdot T_i^{BC}}{f(1 - \rho_{ped})} \quad (2.67)$$

where $f = T_e(\rho_{ped})/T_i(\rho_{ped})$. Thus, the ion heat diffusivity χ_i profile is constructed with the prescribed logarithmic gradient λ_{T_i} for the intermediate region and the gradient μ_{T_i} in the edge region, whereas the central region remains flat.

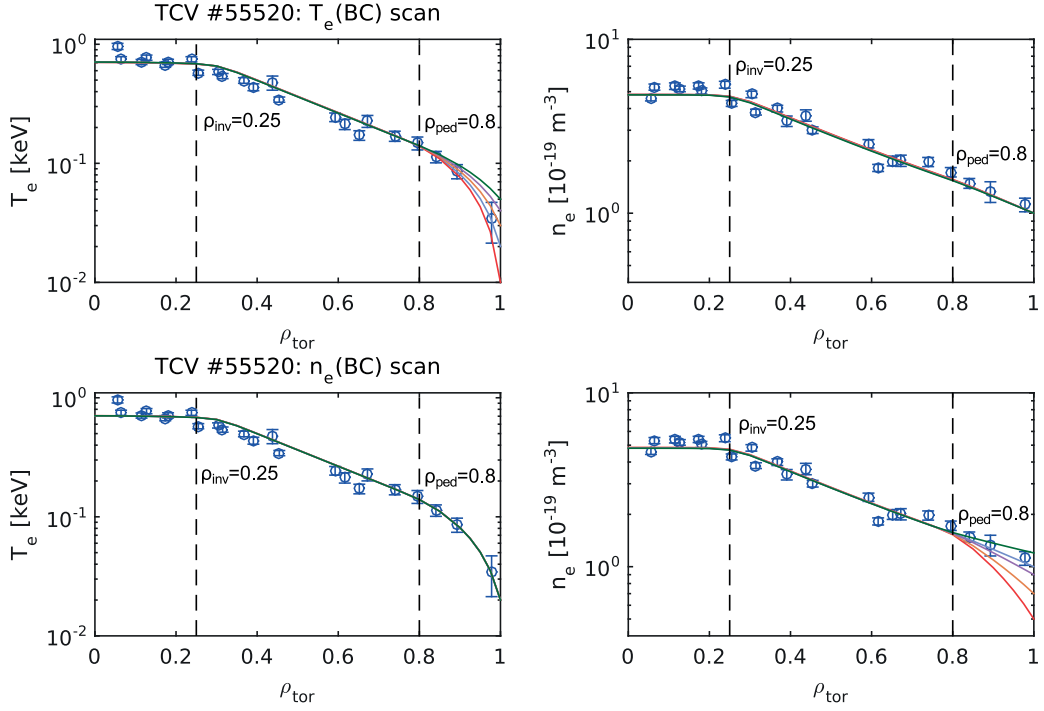


Figure 2.10: Tests of the sensitivity of electron temperature T_e and density n_e profiles, simulated by RAPTOR (color solid), on boundary conditions (BC) for the TCV shot #55520 at $t = 0.6$ s. The first row: scan for T_e BC at 10, 20, 30, 40, 50 keV with $n_e(BC) = 1 \cdot 10^{19} m^{-3}$. The second row: scan for n_e BC at 0.5, 0.7, 0.9, 1.0, 1.2 $10^{19} m^{-3}$ with $T_e(BC) = 20$ keV. Radial profiles, demonstrated on a “log” scale, are constructed with fixed $\lambda_{T_e, n_e} = 3.2/2.0$, $H_e = 0.35$ and $n_{el} = 4.2 \cdot 10^{19} m^{-3}$. Thomson measurements of T_e and n_e are marked by blue circles.

2.6.4 Profiles sensitivity to the boundary conditions

One of the model advantages is the weak dependence of the simulated temperature and density profiles on their boundary conditions (BC). In Fig. 2.10 profiles for the electron temperature T_e and density n_e for the TCV shot #55520 are presented. Predictive simulations of T_e and n_e are done with various boundary conditions, and the profiles are checked at $t = 0.6$ s. Two scans on BC are performed for T_e and n_e separately. In these simulations H_e -factor and n_{el} are prescribed and equal to 0.35 and $4.2 \cdot 10^{19} m^{-3}$. The T_e and n_e gradients in the “stiff” region are fixed, $\lambda_{T_e} = 3.2$ and $\lambda_{n_e} = 2$. Gradients in the pedestal region, μ_{T_e} and μ_{n_e} , vary depending on the boundary conditions to match the requested H_e and n_{el} values with prescribed λ_{T_e} and λ_{n_e} . Thus, main difference in the profiles can be observed in the pedestal region, whereas the intermediate and the central region are almost not affected. For the $T_e(BC)$ scan $n_e(BC)$ is fixed at $1 \cdot 10^{19} m^{-3}$. To get requested H_e factor with different $T_e(BC)$, values of $n_e(\rho_{ped})$ are slightly different what leads to a shift of the n_e profile in the “stiff” region. However, as it can be seen from Fig. 2.10, these shifts are negligible for $T_e(BC)$ and $n_e(BC)$ scans. We can conclude that there is no strong dependence on T_e and n_e boundary conditions, thus fixed BC can be used for simulations of a plasma discharge. This is because the main

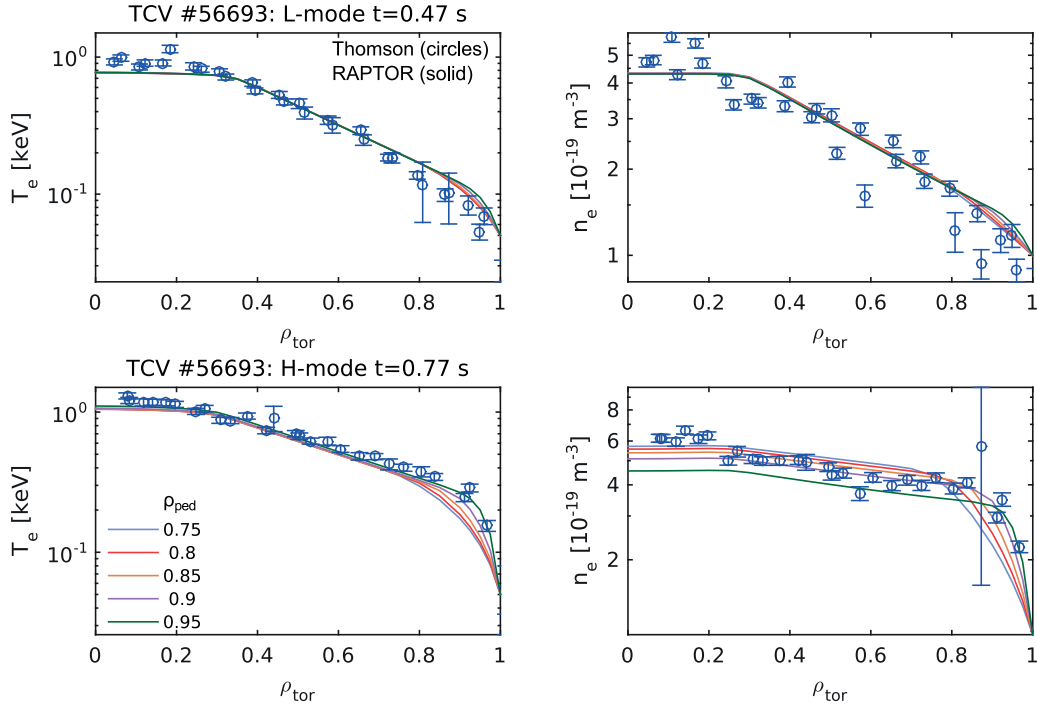


Figure 2.11: Tests of the sensitivity of electron temperature T_e and density n_e profiles on the pedestal position ρ_{ped} at 0.75, 0.8, 0.85, 0.9, 0.95 for the TCV shot #56693 at $t = 0.44$ s (L-mode) and $t = 0.77$ s (H-mode). Radial profiles, demonstrated on a “log” scale, are constructed with fixed $\lambda_{T_e, n_e} = 3.2/2.0$ in L-mode and $\lambda_{T_e, n_e} = 2.3/1.0$ in H-mode, $H_e = 0.35/0.4$ and $n_{el} = 2.9/4.8 \cdot 10^{19} \text{ m}^{-3}$ in L-/H-modes.

parameters determining the kinetic profiles are the H/H_e factors and logarithmic gradients.

2.6.5 Summary of the transport model parameters

Here we summarize parameters required by the gradient-based transport model, presented above. Since the model is based on the assumption of the plasma profiles “stiffness” in the region between ρ_{inv} and ρ_{ped} , a parameter, characterizing the profiles gradients, has to be defined. To simulate one of plasma profiles, T_e , n_e or T_i , we prescribed a constant logarithmic gradient λ_{T_e, n_e, T_i} . Since in the high confinement mode plasma profiles are more flat than in L-mode, λ_{T_e, n_e, T_i} should be defined for L- and H-modes separately. Position of the pedestal is also different for L- and H-modes, generally its width is smaller for H-mode [Ryter et al.(1994)]. In Chapter 3, typical values of λ_{T_e, n_e, T_i} for TCV, AUG and JET plasmas are defined. With predictive simulations, it is important to get realistic pedestal height of plasma profiles, since it can change significantly the global plasma properties, like the heat and particle confinement, which are necessary for correct estimation of a plasma state. Therefore, the proposed transport model requires following prescribed parameters: the confinement factor for the electron energy H_e for T_e modelling, the line-averaged density n_{el} for n_e modelling,

the confinement factor for the total plasma energy H for coupled simulations of T_e and T_i . Thus profiles in the pedestal region, i.e. between ρ_{ped} and 1, are constructed with a linear gradient μ_{T_e, n_e, T_i} to match prescribed global parameters.

Prediction of the pedestal radial coordinate ρ_{ped} is a rather difficult issue for plasma simulations, since its formation depend on many factors, like plasma fueling or instability activities [Urano(2014)]. There are no proper theoretical models for L-mode, since the pedestal region is not generally considered for this mode. The EPED model [Snyder et al.(2011)] predicted ρ_{ped} for H-mode within 20% agreement with experimental data. For the transport model, developed in this thesis, we fix ρ_{ped} at 0.8 and 0.9 for L- and H-modes respectively. Similar values have been used in [Kim et al.(2016)]. As it can be seen from simulations of TCV #56693 with fixed λ_{T_e, n_e} in Fig. 2.11, there are no big changes in the profiles in case of L-mode plasma. In H-mode n_e profiles are affected more than T_e profiles, since they are much more flat. Therefore the variation of ρ_{ped} with fixed n_{el} and λ_{n_e} leads to vertical shifts in the profiles. We can see that ρ_{ped} at 0.8 and 0.9 give the best matching with experimental measurements. Since within this thesis no systematic study on the pedestal position for AUG and JET plasmas have been done, we use the same ρ_{ped} as for TCV plasmas, which matches relatively well the measured profiles simulated so far. Note that in the simulation presented in this thesis, same pedestal position is used for electron temperature and density profiles. However, ρ_{ped} for T_e and n_e can be fixed at different values, defined after more detailed analysis of the pedestal properties.

In the developed model, plasma profiles are characterized by the constant gradient λ_{T_e, n_e, T_i} and pedestal position ρ_{ped} , prescribed for L- and H-modes separately. In the transition phases these parameters are allowed to evolve linearly with time between their L-/H- values. Duration of the transition phase, i.e. characteristic time of the pedestal development/decrease, depends on various plasma parameters, like respective confinement times and plasma volume, and can be estimated with the help of experimental measurements of the plasma profiles time evolution. In the following chapter 3 for TCV, AUG, and JET plasma modelling, duration of the transition phases is around 0.1 s, 0.5 s, 1.0 s respectively. These characteristic times were defined for each machine from Thomson and H_α diagnostic measurements. In this research, we assume same duration of L- to H-modes and H- to L-modes transitions.

2.7 Summary

In this chapter, the RAPTOR code [Felici(2011), Felici et al.(2011), Felici et al.(2012)] has been introduced. Since it has been developed for real-time control purposes, high speed of simulations is one of the important features of the code. RAPTOR is a transport simulator without a special solver for the plasma equilibrium reconstruction. A new numerical procedure for processing the equilibrium data has been discussed in Sec. 2.2. The RAPTOR transport model, updated recently, includes diffusion equations for the poloidal flux, electron and ion temperatures, and density of various plasma species. Predictive simulations of the diffusion of the

Chapter 2. The RAPTOR code: overview and developments

plasma current are coupled with plasma kinetic profiles for self-consistent simulations of the time evolution of the plasma state.

We have presented upgrades of the RAPTOR transport equations, carried out as part of this thesis. In contrast to the initial version of the code, now transport equations allow simulations with time-varying terms, improving predictive capabilities of the code in case of strong changes in the plasma equilibrium, geometry and densities. This is crucial especially for ramp-up and ramp-down phases of a plasma discharge, where simultaneous rapid changes in the plasma volume and the plasma current take place. It is also important to be able to simulate transitions from L- to H-mode and vice versa. Verification tests have been performed with the help of the ASTRA code in Sec. 2.4. Transport equations for plasma particles (Eq. 2.32) and ion temperature (Eq. 2.24) have been implemented in the code. To prove the validity of the new equations, successful benchmarks versus the CRONOS code and prescribed solutions for an ITER case for particle transport have been carried out in Sec. 2.5.

For realistic predictive simulations of plasma profiles, reliable physical models are required. We need to predict correctly a time evolution of an entire plasma discharge, therefore transport models capable for plasma modelling both in L- and H-modes are required. The gradient-based transport model, implemented into the RAPTOR code and described in Sec. 2.6, easily allows switching between L- and H-modes, taking into account such characteristic changes in plasma profiles as varying width of the pedestal or profiles fluttering. Note that any change in the parameters induce a modification of the heat and particle conductivities (Eqs. 2.52, 2.60, 2.61) which then leads to a modification of the time evolution of the kinetic profiles. The time scales are therefore relatively well described. Since this gradient-based transport model uses parameters well-known experimentally (the energy confinement factor, critical gradients for temperature and density profiles, the line-averaged density), they can be easily checked and constrained with experimental measurements.

In this thesis, we consider only off-line applications of the model. However, it is rather promising for real-time applications too. With model parameters prescribed for a machine or confinement mode, plasma profiles are constructed correctly on a global time scale. If a strong difference is observed between predicted and measured plasma profiles, it can indicate the presence of internal barriers or a mode growth which lead to local changes of the plasma profile. Deviations in the plasma confinement estimated in real-time from one prescribed by the model can determine periods of improved or degraded plasma confinement, providing useful information to real-time controllers, or of failure of some diagnostic. Note that at this moment, for real-time usage with the RAPTOR code, the model still has to be optimized. The PI controller, used for calculations of the gradient μ_s in the edge region (s denotes to T_e , n_e , T_i), increases the number of Newton steps, required for the solution convergence at every time step, up to 3 ÷ 4 instead of 1 ÷ 2 typical for RAPTOR [Felici et al.(2011)]. If a scaling law for the parameter μ_s is developed or typical values for μ_s are known, then the PI controller can be replaced by prescribed μ_s , saving calculations time.

Since RAPTOR has been developed as a fast and light simulator, there is no intention to include detailed and extremely precise physical modules as such more complex codes like CRONOS [Artaud et al.(2010)] and ASTRA have [Pereverzev and Yushmanov(2002)]. We are aiming to develop simple and fast modules which nevertheless provide realistic predictions on the plasma state and can be used as core elements for real-time plasma controllers. Note that the development of neural network transport models based on first principles gyrokinetic calculations (like QuaLiKiz [Bourdelle et al.(2016)] coupled with RAPTOR in [Felici et al.(2018)]) can provide fast and sophisticated models.

3 Entire shot simulations with the RAPTOR code

Development of physical models for future machines and their experimental validation on existing devices is an essential part of the ongoing research. Various codes like CRONOS [Artaud et al.(2010)], ASTRA [Pereverzev and Yushmanov(2002)], JETTO [Cenacchi et al.(1988)] have been developed for these purposes focusing on specific goals.

This thesis, related to the development of transport models for the RAPTOR code, is devoted to realistic prediction of plasma transport, electron heat and particle confinement, while keeping a high calculation speed. We focus more on analysis of plasma kinetic profiles on global scales of a plasma discharge rather than their accurate prediction in a specific time instant. Nevertheless for testing the developed models, plasma profiles are checked with respect to local and global measurements. This chapter is dedicated to the validation of the extended set of transport equations, described in Sec 2.4, and the new ad-hoc models for the electron heat and particle transport, implemented into the RAPTOR code and presented in Sec. 2.6, which enable a demonstration of realistic simulations of various plasma profiles for TCV, ASDEX Upgrade (AUG) and JET tokamaks.

As part of this work, transport models are tuned for three machines and appropriate parameter values and ranges are provided. We have found that for the chosen tokamaks, characteristic gradients for electron heat transport λ_{T_e} , describing the “stiff” region defined in Sec. 2.6, are close to each other. They belong to the range $3 \div 3.2$ for L-mode plasmas and are around 2.3 for H-mode, i.e. the normalized inverse scale length R/L_{T_e} lies between $6 \div 14$ for machines with aspect ratios $\epsilon = 3 \div 3.5$. Obtained results stay in a good agreement with theoretical predictions of gyrokinetic studies [Jenko et al.(2005)] and experimental observations [Ryter et al.(2001)], which show that the temperature profiles are limited by a critical gradient $R/L_{T_e}|_c$ because of generation of various turbulent modes and their growth with increasing electron heat flux. Similar studies have been carried out for the electron particle transport [Angioni et al.(2009), Fable et al.(2010)]. Characteristic gradients λ_{n_e} used in this work belong to the range $1 \div 2$ in L-mode and $0.5 \div 1.0$ in H-mode, thus R/L_{n_e} is around $1.5 \div 7$. Exact values of the critical gradient $R/L_{T_e, n_e}|_c$ depends on the driven turbulent mode (trapped electron mode TEM [Coppi and Rewoldt(1974)], ion-temperature-gradient ITG [Romanelli(1989)]

and electron-temperature-gradient ETG [Horton and Hong(1988)] driven modes) and various plasma parameters, like the plasma shear s , an effective charge Z_{eff} and the ion-electron temperature balance. Analytical formulas, based on experimental observations and theoretical predictions, have been derived for $R/L_{T_e, n_e}|_c$ estimation like in [Jenko et al.(2001)] and [Hillesheim et al.(2013)]. However, a detailed analysis of critical gradients and driven turbulent modes is out of scope of this work. Obtained characteristic gradients λ_{T_e, n_e} and corresponding inverse scale lengths $R/L_{T_e, n_e}$ are within the typical range observed on TCV, AUG and JET tokamaks. Also typical values of the electron energy confinement factor H_e , required for a description of the “non-stiff” transport gradient at the plasma edge region μ_{T_e} (in Eq. 2.57), has been specified for a machine and a confinement mode. At this stage of the model development as a part of a post-shot analysis, the line-averaged density n_{el} , required by the predictive transport model for electrons, is defined from experimental measurements.

In addition to obtained general set of transport parameters, we also consider a couple of special cases of plasma behavior. Firstly, a TCV plasma with off-axis heating is simulated. Since there is a well known effect of a plasma confinement degradation because of dominant off-axis heating, H_e for the TCV transport model has to be decreased to match experimental measurements. Also a generation of hollow electron temperature profiles in case of strong radiation from a plasma core is considered for AUG and JET plasmas.

Transport parameters, determined in this chapter for TCV, AUG and JET plasmas, are helpful for future development of feedback controllers and operational scenarios. Since these parameters represent most common plasma behavior on chosen machines, an information provided by RAPTOR simulations can be used for a basic analysis of a plasma behavior before running an experiment, thus helping to improve a plasma performance and to increase a positive outcome of experiments. If feedback controllers observe a large difference between predicted and measured temperature profiles, for example, it can be used as an indicator of an instability mode growth, an improved confinement or diagnostic problem.

The chapter is organized in the following way. Firstly, in Sec. 3.1 we discuss a general set of predicted parameters required by RAPTOR to run a simulation. In Sec. 3.2 we start with simulations of TCV low confinement (L-mode) mode plasmas and continue with simulations of a TCV plasma in the high confinement mode (H-mode) with various heating scenarios. Validation of the transport models is continued with simulations of AUG plasmas in Sec. 3.3. Then results of JET plasma modelling are presented in Sec. 3.4. We conclude the chapter with a general discussion on the presented simulations and with a summary of the main results and proposals of the next-step improvements and requirements in the RAPTOR transport models in Sec. 3.5.

3.1 Predicted parameters for a RAPTOR run

To start a simulation with the RAPTOR code, since it does not include an equilibrium solver, we need a prescribed plasma equilibrium to determine the geometrical quantities used in

3.1. Predicted parameters for a RAPTOR run

the transport equations 2.36-2.40. For the simulations discussed below, output of various equilibrium reconstruction codes is reprocessed with the CHEASE code [Lütjens et al.(1996)] to a special format required by RAPTOR, as described in Sec. 2.2 and Appendix A. To take into account the time evolution of the plasma equilibrium, thus the geometrical quantities, a series of equilibria is required. The exact number of equilibria to characterize a plasma discharge depends on the plasma state time evolution, but at least three equilibria have to be taken for each of the ramp-up and ramp-down phases and a couple of extra equilibria for the flattop phase. The choice is easily made in order to follow well $I_p(t)$ and $\kappa(t)$ in particular with piecewise linear interpolations, as well as $\beta(t)$ and transitions between low (L) and high (H) confinement modes when needed.

The evolution of plasma profiles is considered in two dimensions: in space and time. For simulations presented in this section, the radial grid $\hat{\rho}$ is defined on 21 points to have more than one point in the transition regions between “stiff” and “non-stiff” regions. TCV shots are simulated on a time grid with 1 ms step. For simulations of AUG and JET shots the time grid has a 10 ms step and a phase of 0.2 s at the beginning with 1 ms step for a faster stabilization of the controller in the transport model described in Appenix C.

The next step is to specify plasma actuators, like the plasma current and heating and current drive scenarios. Time evolution of the parameters like total plasma current I_p , total input powers from NBI P_{NBI} , ECRH P_{ECRH} and ICRH P_{ICRH} are generally programmed before an experiment, thus they are known in real-time, and can be obtained from the database after an experiment. The problem of reconstruction of heating and current profiles can be solved with specialized codes, briefly mentioned in Subsec. 2.3.2. To save CPU time, in RAPTOR, heating and current driven profiles are approximated by Gaussian curves with prescribed widths and radial depositions, such that the integrated values match the expected total absorbed power and driven currents.

We use the RAPTOR internal module to simulate sawtoothing plasmas as it has been described in Subsec. 2.3.4. In the simplest form, a critical shear value has to be specified by the user except if the s_{1crit} formula is used. Thus we choose either typical values, known for a machine from experiments or previous simulations, or specify it to match experimental measurements of the sawtooth period.

A critical issue of using the experimental data as input parameters or for the validation of RAPTOR simulation results, is that they have to be provided on the RAPTOR radial grid, i.e. on the toroidal normalized grid $\hat{\rho}$, defined in Eq. 2.15. Some databases, like one for TCV, provide electron temperature T_e and density n_e profiles both on the normalized poloidal and toroidal grids. Thus, they can be used by RAPTOR directly. However generally, the radial coordinate is associated with the poloidal flux ψ , and the measurements have to be interpolated from their own radial grid to the RAPTOR radial grid $\hat{\rho}$. A relation between these grids usually is obtained from an equilibrium reconstruction code, since poloidal and toroidal fluxes are generated by the code. With magnetic measurements of the poloidal flux ψ and solving of

the Grad-Shafranov equilibrium equation 2.10, the code provides the plasma equilibrium quantities on the normalized poloidal grid $\hat{\rho}_{\hat{\psi}}$, associated with fluxes of constant ψ . Such equilibrium profiles like the toroidal flux Φ and the safety factor q are calculated as functions of $\hat{\rho}_{\hat{\psi}}$. Using the definition of the toroidal normalized grid $\hat{\rho}$ in Eq. 2.15, q can be remapped from $\hat{\rho}_{\hat{\psi}}$ to $\hat{\rho}$. If the time evolution of a plasma equilibrium is known, then q profiles can be defined as functions of $\hat{\rho}_{\hat{\psi}}$ and $\hat{\rho}$ in time. In similar way any other profiles can be interpolated from $\hat{\rho}_{\hat{\psi}}$ to $\hat{\rho}$, if plasma equilibria are known. Thus, for example T_e and n_e profiles provided by Thomson diagnostic on $\hat{\rho}_{\hat{\psi}}$ for AUG and JET plasmas can easily be remapped to $\hat{\rho}$.

The transport parameters discussed above can generally be obtained after an experiment from the machine database or from a known scenario of a discharge. For a transport code like RAPTOR, depending on a simulation goal, proper transport coefficients have to be determined. In Sec. 2.3 various transport models implemented into RAPTOR have been mentioned. In this chapter we focus on the validation of the ad-hoc gradient-based transport models proposed in Sec. 2.6. As it has been discussed in that section, for the electron heat and particle transport, there are few model parameters: constant gradients for the “stiff” region λ_{T_e, n_e} , the pedestal radial coordinate ρ_{ped} , the heat confinement factor for electrons H_e and the line-averaged density n_{el} . These parameters, except the last one, are specified for L- and H-modes separately. The line-averaged density n_{el} at this moment is prescribed from the experimental signal. Time instants of transitions between the modes and their duration also have to be specified by a user and can be defined in several ways, as discussed in Subsec. 2.6.1. In the simulations presented below, we validate the transport model simulating TCV, AUG and JET plasmas. A critical question for such transport models is that the various parameters should not need to be tuned in too much detailed for various phases of specific discharges and should be easily applicable to a new machine. From the experience presented here, we will see that the proposed model is efficient across a full discharge simulation and has been very easily extended from one machine to the next.

3.2 TCV plasma modelling

Since the gradient-based transport models have been first developed for various TCV plasmas [Sauter et al.(2014), Kim et al.(2016)], we start this chapter with a section dedicated to simulations of various TCV plasma discharges and developing of the transport model for TCV within RAPTOR.

3.2.1 An ohmic L-mode shot

Here we consider an ohmic L-mode TCV shot #55520. Firstly, we have to define plasma parameters which will be used as input parameters for RAPTOR.

$\lambda_{T_e}(L)$	2.4	2.8	3.2	3.6	4.0
χ^2	5.4	4.2	3.5	4.4	5.3
$\lambda_{n_e}(L)$	1.2	1.6	2.0	2.4	2.6
χ^2	8.1	5.6	5.3	7.3	10.7
$\lambda_{T_e}(H)$	1.7	1.9	2.3	2.7	2.9
χ^2	5.4	4.2	4.0	5.6	6.8
$\lambda_{n_e}(H)$	0.4	0.6	1.0	1.4	1.6
χ^2	9.6	8.5	7.3	7.8	8.6

Table 3.1: The χ^2 tests for various TCV λ_{T_e, n_e} to define the goodness of the fit between RAPTOR simulated and Thomson measured T_e and n_e profiles.

The prescribed data set

The total plasma current $I_p(t)$ is known from the TCV database and, since we consider an ohmic shot, it is the only actuator for RAPTOR. Experimental equilibria for TCV plasmas are generated by the LIUQE code [Hofmann et al.(1988)]. Since RAPTOR requires an equilibrium data set in a special format, LIUQE equilibria have been reprocessed by the CHEASE code [Lütjens et al.(1996)] as it was discussed in Sec. 2.2 and Appendix A. For the entire TCV shot #55520 simulation, twelve CHEASE equilibria have been used. Of course more equilibria can be used but it does not change the result.

For this particular case, we are going to predict time and radial evolution of the poloidal flux $\psi(\hat{\rho}, t)$ and the electron temperature $T_e(\hat{\rho}, t)$. Thus profiles for the ion temperature T_i , the electron n_e and ion density n_i have to be prescribed in advance. We take time-varying radial profiles for n_e from Thomson measurements fitted in a radial direction to get smooth radial profiles. Plasma profiles for ions T_i and n_i are scaled from T_e and n_e with 10% difference in the plasma center to match measured MHD energy, stored in the plasma. Because of the absence of necessary measurements, the effective charge Z_{eff} is fixed at 1.8, typical TCV value, assuming a radially constant profile.

The gradient-based transport model for the electron heat diffusivity χ_e , described in Subsec. 2.6.1, has been chosen for this simulation, thus parameters H_e -factor and ρ_{ped} have to be defined. The latter parameter represents the right boundary of the “stiff” region and, in a similar way as for the H-mode, defines the pedestal region in the L-mode [Sauter et al.(2014)]. Here, it is fixed at $\hat{\rho}_{ped} = 0.8$, the typical value for TCV L-mode shots as shown in Subsec. 2.6.5. The H_e factor has been specified after analyzing various TCV L-mode phases at $H_e(L) = 0.35$.

Predicted parameters

The simulation starts from the middle of the ramp-up phase at 0.1 s, where we have the first LIUQE equilibrium, and continues until 1.07 s, i.e. up to the last available LIUQE equilibrium at the end of the shot. Simulation with 1 ms time step of the entire shot 1 s long took only 50 s of CPU time without any optimization on a standard PC.

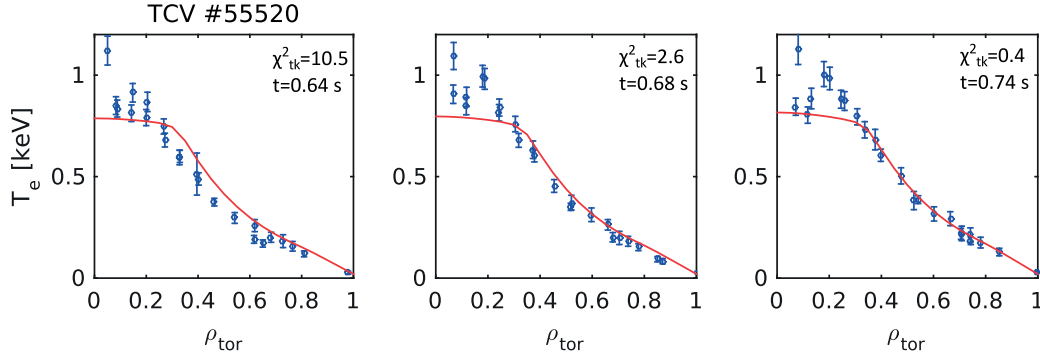


Figure 3.1: Electron temperature T_e profiles for the TCV shot #55520 provided by Thomson measurements and predicted by RAPTOR simulations with fixed $H_e = 0.35$ and $\lambda_{T_e} = 3.2$. The parameter $\chi^2_{t_k}$ is used to estimate the goodness of predicted profiles at the time instant t_k .

To define λ_{T_e} with which RAPTOR simulated T_e profiles will best fit experimental T_e , several simulations have been performed. Their results are presented in Table 3.1 for the parameter $\lambda_{T_e}(L)$. The goodness of the RAPTOR predicted T_e profile with respect to Thomson measurements is accomplished with a χ^2 test. Parameter $\chi^2_{t_k}$ is calculated at the every time step on the RAPTOR time grid between measured and simulated T_e in the “stiff” region and then is averaged over the simulation time to get χ^2 . These parameters are defined in the following way:

$$\chi^2_{t_k} = \frac{1}{N_{\hat{\rho}}} \sum_{i=1}^{N_{\hat{\rho}}} \frac{(T_e^{RP}(\hat{\rho}_i, t_k) - T_e^{TH}(\hat{\rho}_i, t_k))^2}{\sigma_{T_e}^2(\hat{\rho}_i, t_k)} \quad (3.1)$$

$$\chi^2 = \frac{1}{N_{tk}} \sum_{t_k=1}^{N_{tk}} \chi^2_{t_k} \quad (3.2)$$

where $N_{\hat{\rho}}$ and N_{tk} are the number of radial and time points, T_e^{RP} and T_e^{TH} are RAPTOR and Thomson profiles for the electron temperature, $\sigma_{T_e}^2(\hat{\rho}_i, t_k)$ denotes the standard deviation of Thomson measurements. According to $\lambda_{T_e}(L)$ in Table 3.1, λ_{T_e} is fixed at 3.2 for TCV L-mode plasmas. Note that χ^2 presented in the table are averaged over time. The RMS error increases up to 50%. It can be seen from Fig. 3.1 that profiles with $\chi^2_{t_k} \approx 0.4$ have been obtained with $\lambda_{T_e}(L) = 3.2$. Profiles with much higher $\chi^2_{t_k} \approx 10$ can be obtained too, but in the case presented in Fig. 3.1, some Thomson measurements have very small error bars. Since they are used in Eq. 3.1, it can increase χ^2 value.

The plasma current time trace is shown in Fig. 3.2 with red dots, which correspond to time instants of the LIUQE equilibria. To validate RAPTOR simulation results, we check the time and radial evolution of various physical quantities calculated by RAPTOR with signals provided by the database. In Fig. 3.2 we demonstrate time traces of the safety factor q and the electron temperature T_e at various radial positions, the internal inductance $l_i(3)$ and the H_e factor.

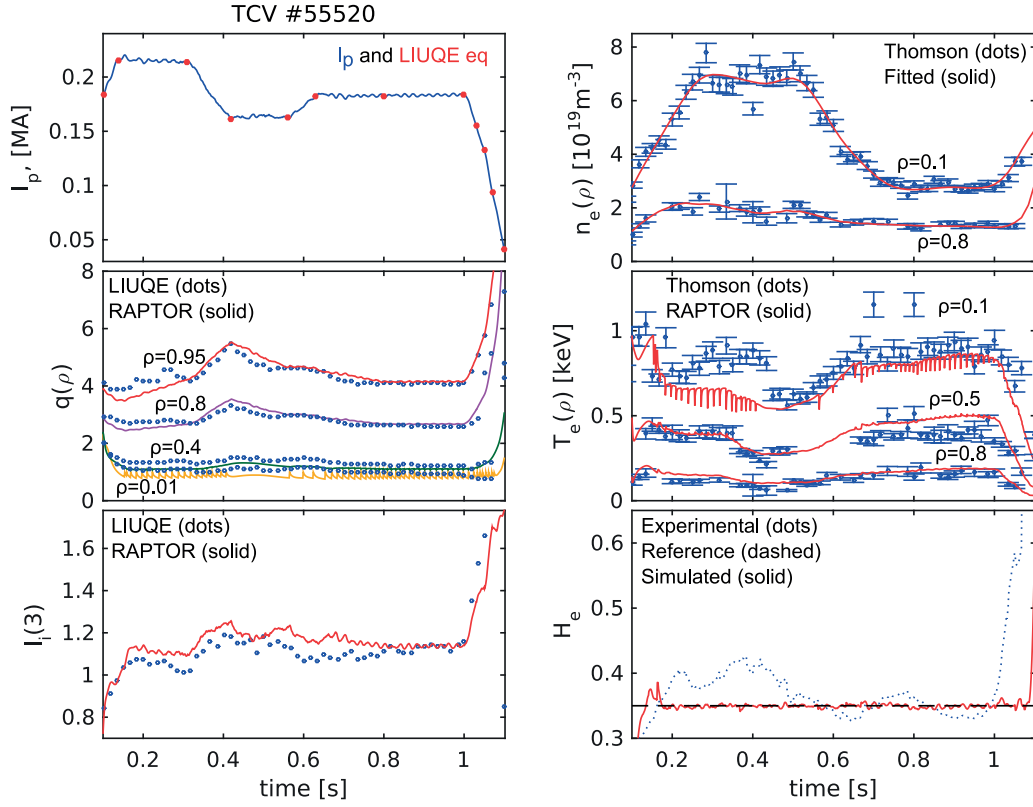


Figure 3.2: Prescribed time traces for the TCV shot #55520: the plasma current I_p ; the electron density n_e provided by Thomson measurements and fitted data used by RAPTOR $\rho_{tor} = [0.1, 0.8]$. Predicted parameters for the TCV shot #55520: the safety factor $q(\rho)$ at $\rho_{tor} = [0.01, 0.4, 0.8, 0.95]$ for LIUQE (dots) and RAPTOR (solid); the electron temperature T_e provided by Thomson (dots) and RAPTOR (solid) $\rho_{tor} = [0.1, 0.5, 0.8]$; the internal inductance $l_i(3)$ from LIUQE (dots) and RAPTOR (solid); experimental (dots), reference (dashed) and RAPTOR (solid) H_e -factor.

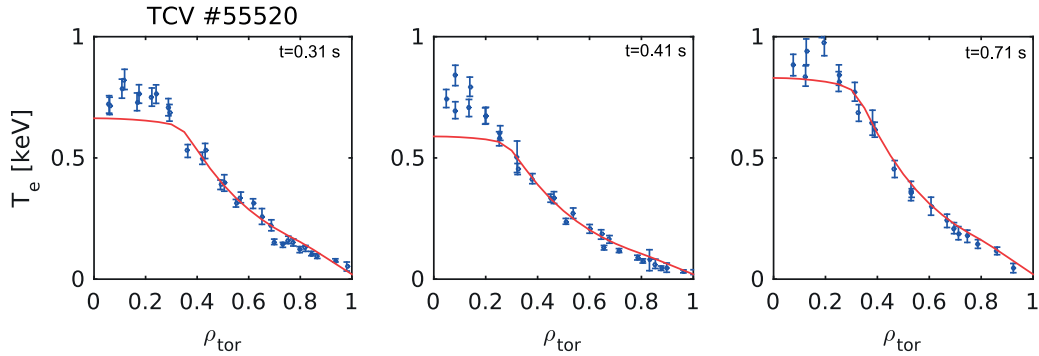


Figure 3.3: Electron temperature T_e profiles at $t = [0.31, 0.41, 0.71]$ s for the TCV shot #55520 provided by Thomson measurements (dots) and predicted by RAPTOR (solid) with fixed $H_e = 0.35$ and $\lambda_{T_e} = 3.2$.

From Fig. 3.2 it can be seen that the time evolution of the safety factor q simulated by RAPTOR shows a good agreement with the results of the equilibrium reconstruction code LIUQE. The simulated plasma internal inductance $l_i(3)$ follows the experimental one very well at the flat-top phase and during the ramp-down phase. When they are different, they still follow the same trends. The LIUQE code uses only the magnetic measurements to solve the Grad-Shafranov equilibrium equation. The disadvantage of such an approach for simulation of dynamic phases of a plasma discharge is the lack of information about resistive diffusion of the current density profile which RAPTOR does compute. This can be a reason for the difference between the internal inductance simulated with RAPTOR and the one provided by LIUQE.

Radial profiles of the electron temperature $T_e(\rho, t)$ from RAPTOR follow Thomson measurements very well as demonstrated in Fig. 3.2. There is a transient slightly improved confinement phase, between 0.2 s and 0.5 s, where the experimental H_e factor, based on Thomson measurements of T_e and n_e , increases up to 0.41. The central electron temperature simulated with RAPTOR does not match the experimental measurements, whereas at $\rho = 0.5$ and $\rho = 0.8$ it follows them very well over the entire plasma discharge. Since many plasma parameters are changing (the plasma current I_p , plasma shape, the electron density n_e), it is difficult to determine the main factor which leads to improved confinement. At least, there is a clear influence of the decrease in the plasma current I_p , which leads to the decrease in ohmic power and the growth in the H_e factor. Looking closer to T_e profiles in Fig. 3.3, we can conclude that the predicted gradients in the “stiff” region stay in a very good agreement with experimental measurements during the phase of the improved confinement (at 0.31 and 0.41 s) and after it (at 0.71 s). Thus, with RAPTOR predictions the information about T_e is missed from the central region only. Adjusting of ρ_{inv} , i.e. making an artificial prolongation of the “stiff” region inside the $q = 1$ surface, will increase T_e profiles at $\rho = 0.2$.

Predicted simulations of the electron density

We continue simulations of the TCV L-mode shot #55520 with predictions of the electron density n_e in addition to the poloidal flux ψ and the electron temperature T_e . For the gradient-based transport model, the line-averaged density n_{el} has to be prescribed. Here we smooth the line-averaged density provided by the integrated FIR measurements with LIUQE equilibrium mapping. After testing several constant gradients for the “stiff” region to predict n_e profiles and using the same procedure as for λ_{T_e} (see Table 3.1), $\lambda_{n_e} = 2.0$.

Simulation results, demonstrated in Fig. 3.4, are similar to the previous modelling with prescribed n_e profiles. Also n_e profiles predicted by RAPTOR are in a good agreement with Thomson measurements, as shown in Fig. 3.5. Note that at this stage we do not predict the particle flux, assuming it to be equal to zero. In this particular case, during the phase of the improved confinement and high n_{el} , i.e. at $t = 0.43$ s in Fig. 3.5, n_e profiles are more peaked than after it. There is a difference between predicted and measured n_e profiles in the central region at $t = 0.43$ s, but later measured as well as predicted n_e profiles are flat. Transport parameters $\lambda_{T_e, n_e} = 3.2/2.0$ and $H_e = 0.35$ have been tested on several other TCV L-mode shots

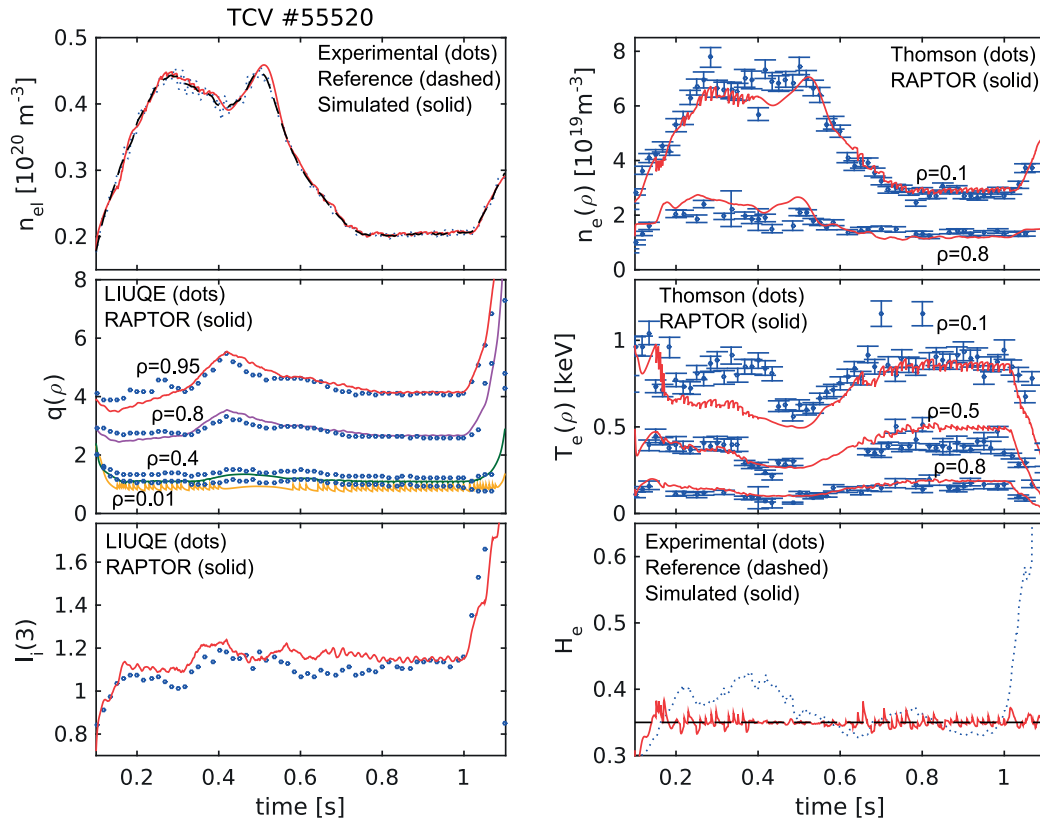


Figure 3.4: Prescribed time traces for the TCV shot #55520: the line-averaged density n_{el} from experimental signals (dots), reference (dashed) and RAPTOR (solid). Parameters predicted by RAPTOR: the safety factor $q(\rho)$ at $\rho_{tor} = [0.01, 0.4, 0.8, 0.95]$ for LIUQE (dots) and RAPTOR (solid); the electron temperature T_e and density n_e provided by Thomson (dots) and RAPTOR (solid); the internal inductance $I_i(3)$ from LIUQE (dots) and RAPTOR (solid); experimental (dots), reference (dashed) and RAPTOR (solid) H_e -factor.

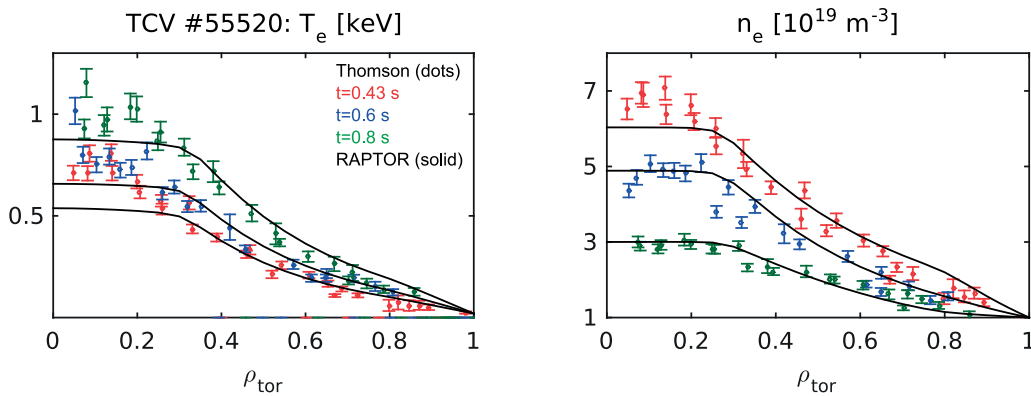


Figure 3.5: Electron temperature T_e and density n_e profiles at $t = [0.43, 0.6, 0.8]$ s for the TCV shot #55520 provided by Thomson measurements (dots) and predicted by RAPTOR (solid) with fixed $H_e = 0.35$ and $\lambda_{T_e, n_e} = 3.2/2.0$.

as well, where we have found a good agreement with Thomson measurements.

3.2.2 An entire shot simulations in case of H-mode plasma

We continue RAPTOR simulations of TCV plasmas with modelling of the shot #56693. The main difference with the previous shot is the presence of NBI heating, which leads to the generation of an H-mode. The NBI power is defined as an additional actuator, and time evolution of the total input power, obtained from the TCV database, is prescribed for the following simulations. Radial profiles of the power density are approximated by Gaussian curves with central deposition at $\rho_{dep} = 0$. and width $w_{NBI} = 0.5$ to get a broad profile. The NBI beam is switched on in the middle of the flattop and kept at 1 MW (with the beam energy 25 keV) up to the end of the discharge, as it is shown in Fig. 3.6. Maximum effective power absorbed by electrons is 0.7 MW, estimated from typical TCV measurements. However, the NBI module for the ASTRA code [Polevoi et al.(1997)] can provide more accurate information about the absorbed power.

Transitions from L- to H-mode and H- to L-mode are fixed at 0.7 s and 0.925 s according to the H_α signal and duration of transition phases equals to 50 ms. Transport parameters λ_{T_e} and H_e for L-mode have the same values as in previous subsection, i.e. 3.2 and 0.35. In H-mode we expect to have flatter T_e profiles and higher H_e -factor, and according to $\lambda_{T_e}(H)$ values from Table 3.1 we use values 3.0 and 0.45 for λ_{T_e} and H_e . From experimental measurements [Urano(2014), Pitzschke et al.(2012)] and numerical predictions [Merle et al.(2017), Snyder et al.(2011)], an H-mode generally is characterized by a narrow pedestal, therefore ρ_{ped} is equal to 0.9 for the H-mode phase (Subsec. 2.6.5).

Prediction of plasma state based on the poloidal flux and the electron temperature

As in the previous subsection, the plasma current $I_p(t)$ and the electron density profiles $n_e(\rho, t)$ have to be prescribed to solve the diffusion equations for the poloidal flux ψ and the electron temperature T_e . Their time traces are presented in Fig. 3.6.

We have a good agreement between RAPTOR and LIUQE simulation results for the safety factor $q(\rho, t)$ and the internal inductance $l_i(t)$. For the transition from L- to H-mode, a decrease in the internal inductance is observed, as we expect: since the electron temperature and density profiles are more flat in H-mode, the current density is less peaked, also because of the edge bootstrap current in H-mode, and therefore, the internal inductance reduces. Transition from H- to L-mode happens during the plasma current ramp-down. With a decrease in the edge current due to the ramp-down induced by a lower edge loop voltage, we observe a fast growth in the internal inductance, and in this case there is no significant impact from the H-L transition on the l_i trajectory.

Simulated temperature profiles $T_e(\rho, t)$ stay very close to Thomson measurements. We can clearly see the growth of the electron temperature at the pedestal area $\rho = 0.8$ during the L-H transition. H_e -factor calculated with predicted T_e profiles follows the experimental one

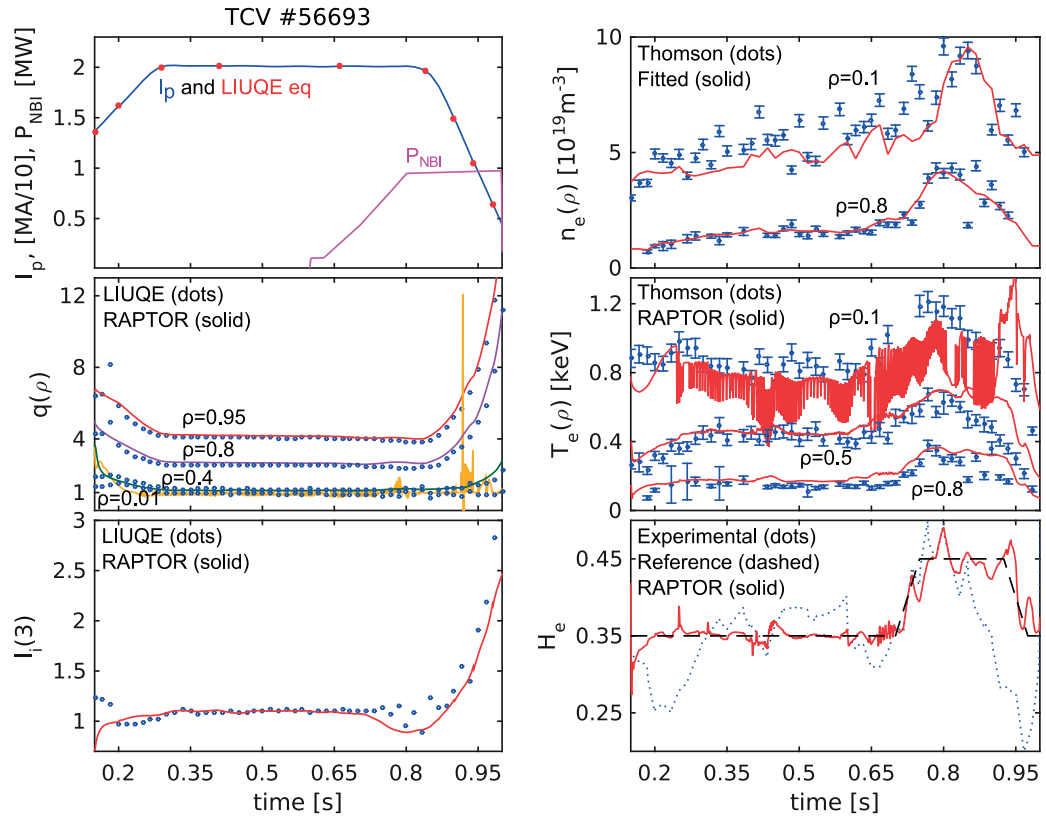


Figure 3.6: Prescribed time traces for the TCV shot #56693: the plasma current I_p and NBI heating power P_{NBI} ; the electron density n_e provided by Thomson measurements and fitted data used by RAPTOR $\rho_{tor} = [0.1, 0.8]$. Predicted parameters: the safety factor $q(\rho)$ time traces for LIUQE (dots) and RAPTOR (solid); the electron temperature T_e provided by Thomson (dots) and RAPTOR (solid) $\rho_{tor} = [0.1, 0.5, 0.8]$; the internal inductance $I_i(3)$ from LIUQE (dots) and RAPTOR (solid); experimental (dots), reference (dashed) and RAPTOR (solid) H_e -factor.

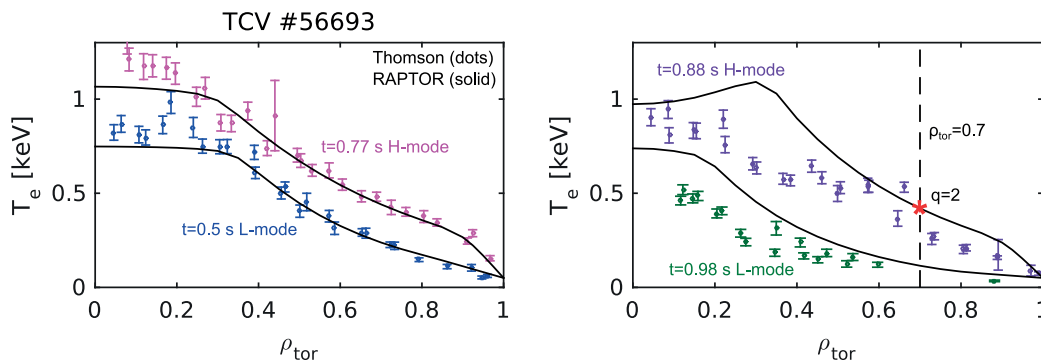


Figure 3.7: T_e profiles from Thomson measurements for TCV shot #56693 and RAPTOR simulation results at $t = [0.5, 0.77, 0.88, 0.98]$ s.

during almost entire discharge as it has been requested by its reference. However, after 0.8 s there is a strong decrease in H_e experimental value. Magnetic measurements show that an NTM was generated and led to the plasma confinement degradation. This can be clearly seen from T_e radial profiles. As it is shown in Fig. 3.7, RAPTOR T_e profiles are in a close agreement with Thomson measurements in L-mode ($t = 0.5$ s) and H-mode ($t = 0.77$ s) plasma. The 2/1 NTM island, generated at the $q = 2$ position around $\rho_{tor} = 0.7$, leads to a flattening of the T_e profile, that is clearly seen from Thomson measurements. Here we do not simulate NTMs with RAPTOR, and therefore there is no effect on simulated T_e profiles which follow the prescribed H_e -factor.

It should be mentioned that the “quality” of T_e profiles also depends on the prescribed n_e profiles. In particular, the formula for the electron energy confinement time, used for calculation of the heat diffusivity χ_e (Eq. 2.56), includes time derivative of the total plasma energy dW/dt . This parameter is calculated in RAPTOR at every time iteration, therefore it is very sensitive to the shape and time evolution of T_e and n_e profiles. Also, the sawtooth crashes are simulated only for T_e profiles, whereas n_e profiles stay as they were prescribed. For this simulation, fitted profiles for the electron density $n_e(\rho, t)$, based on measurements of the Thomson scattering system, are affected by sawtooth crashes and presence of the NTM island. These profiles are fitted in the radial direction but not in time, which can lead to inaccurate prediction of the sawtooth period as in Fig. 3.6.

Test of NBI power density profiles

The simulation presented above uses NBI power density profiles approximated by Gaussian curves with fixed width w and radial deposition ρ_{dep} . We can test the sensitivity of T_e profiles to prescribed parameters w and ρ_{dep} . In Fig. 3.8 T_e profiles (on a “log” scale) at $t = 0.8$ s (H-mode) simulated with various w and ρ_{dep} are shown. In the first row ρ_{dep} equals to 0. In the second row w is fixed at 0.5. Profiles for the electron heat diffusivity χ_e are automatically adjusted in the way to give the same gradient λ_{T_e} in the “stiff” region of T_e .

This low sensitivity to the Gaussian shape parameters w and ρ_{dep} can be considered as another advantage of the transport model, since even not accurate prediction of the shape of power density profiles do not affect the simulation results. Of course it is also a limitation if internal transport barriers are generated in plasmas or lower λ_{T_e} are expected because of off-axis heating. However, these are unusual scenarios and can be treated specifically. Note that in case of prediction of the electron density with a particle source associated with NBI beam, the deposition location might be important.

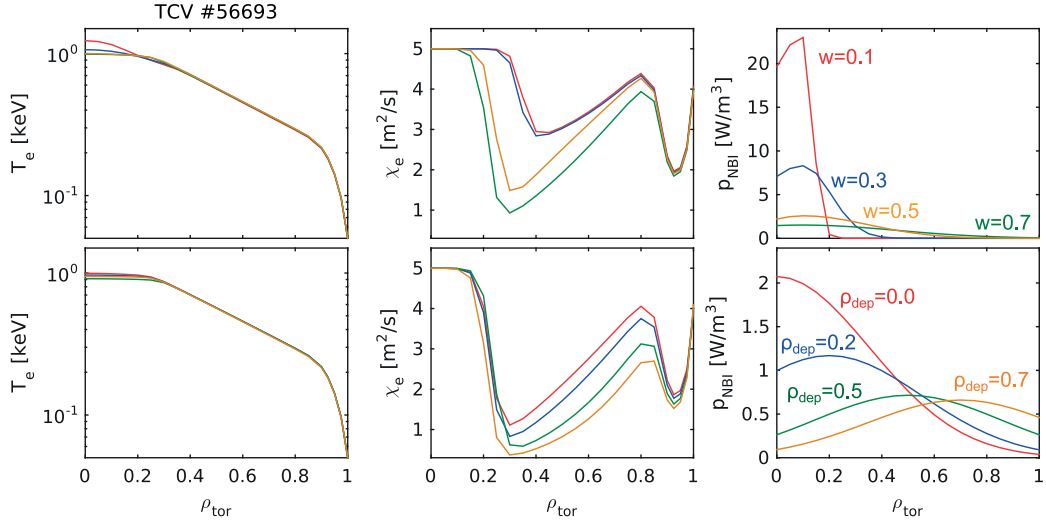


Figure 3.8: Profiles for the electron temperature T_e , the electron heat diffusivity χ_e and NBI power density p_{NBI} for the TCV shot #56693 at $t = 0.8$ s (H-mode). The first row corresponds to p_{NBI} profiles defined as Gaussian curves with various widths $w = [0.1, 0.3, 0.5, 0.7]$. In the second row, plasma profiles obtained in case of various radial depositions of p_{NBI} are demonstrated for $\rho_{dep} = [0.0, 0.2, 0.5, 0.7]$. Thanks to χ_e sensitivity to the heat flux, T_e profiles show the same gradients in the “stiff” region for different p_{NBI} . Figures in the first column are on a “log” scale.

Simulations with the electron density

To have time and radial consistency between the electron temperature T_e and density n_e , the diffusion equation for the electron density (Eq. 2.38) has been solved in addition to transport equations for the poloidal flux ψ (Eq. 2.36) and the electron temperature T_e (Eq. 2.37). As well as for L-mode simulations, here we prescribe the line-averaged density n_{el} from the integrated experimental measurements.

As it can be seen from Fig. 3.9, there is almost no change in time and radial evolution of the safety factor q and the internal inductance l_i . Thanks to consistency of T_e and n_e profiles, we have more regular sawtooth crashes. The sawtooth period increases as the plasma transits to H-mode following the crashes observed with the soft X-ray detector DMPX, described in Subsec. 1.2.3.

Note that the transport model for the pinch velocity V_p , defined in Eq. 2.61, requires the radial-dependent source of particles Γ_e . In this simulation we do not include the source of electrons which comes from NBI. It can be seen from n_e profiles presented in Fig. 3.10, that the source is localized in the central area. Profiles for n_e simulated with RAPTOR have flat central region. Thanks to the controlled μ_{n_e} , the predicted pedestal height follows the experimental one very well and the resulted line-averaged density is close to the prescribed one in the absence of the NTM mode (Fig. 3.10 at $t = 0.5$ s and $t = 0.77$ s). Thus, the absence of the particle source in

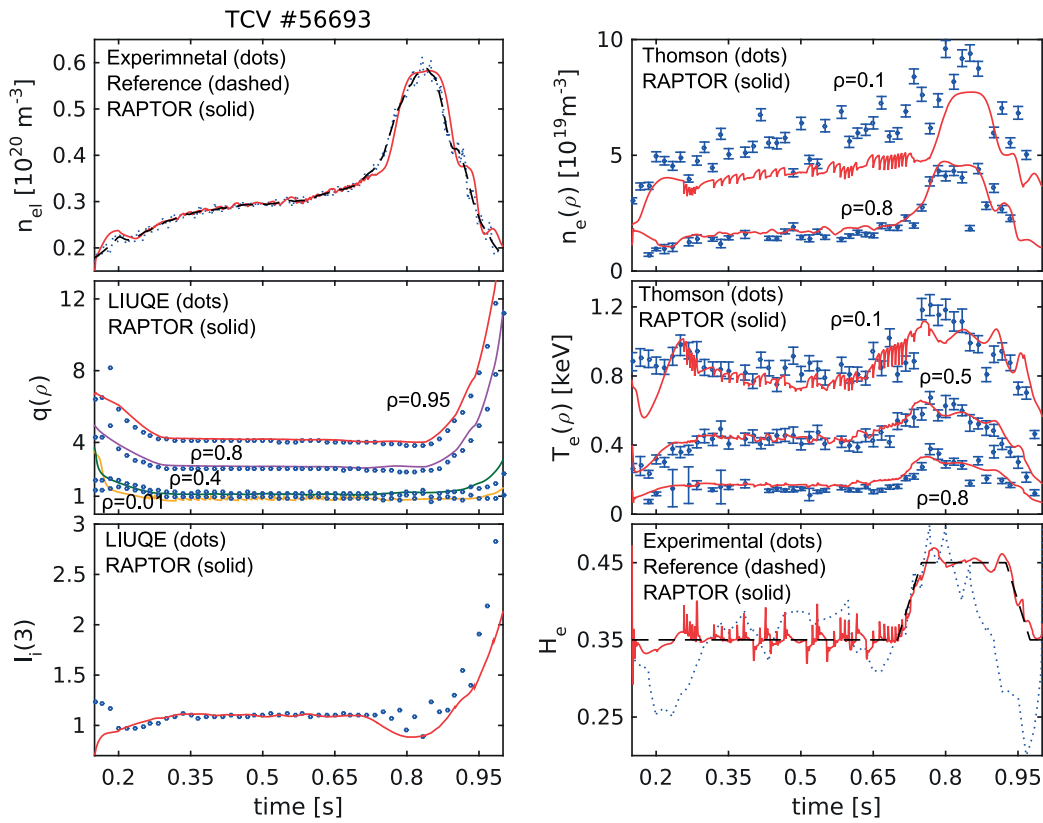


Figure 3.9: Predictive simulation of ψ , T_e , n_e for the TCV shot #56693 with prescribed line-averaged electron density n_{el} and H_e -factor. RAPTOR simulation results are validated with Thomson measurements for the electron temperature density n_e and T_e , with LIUQE output for the safety factor q and the internal inductance l_i .

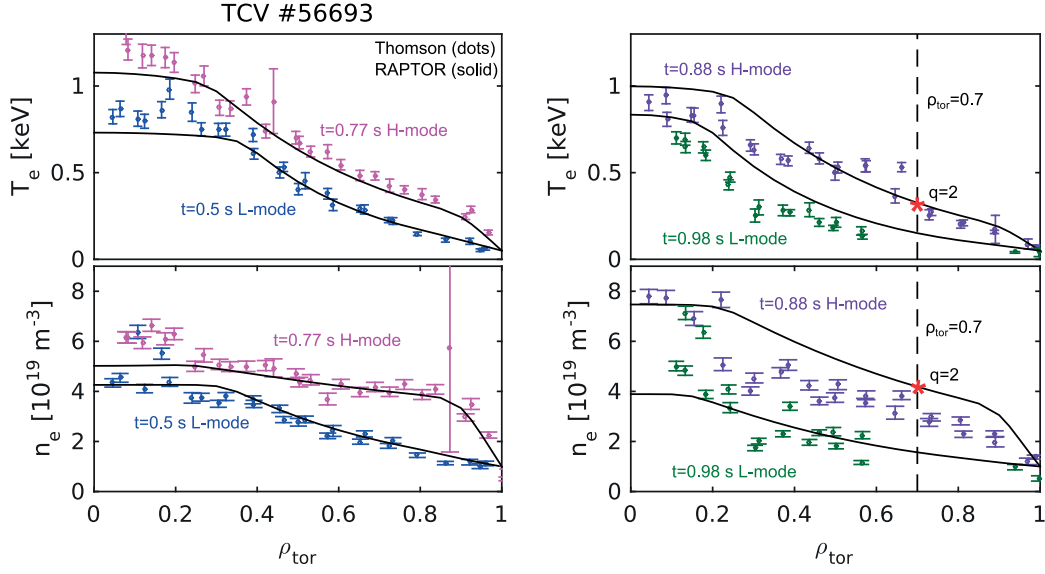


Figure 3.10: Comparison of Thomson measurements for TCV shot #56693 and RAPTOR simulation results for the electron temperature T_e and density n_e at $t = [0.5, 0.77, 0.88, 0.98]$ s.

the transport equation results in an inaccuracy of n_e profiles shape prediction in the central region only but there is no strong effect on the global particle and heat confinement. From ASTRA predictions of the particle flux for this shot, we can see that the source of particles is concentrated mainly at the plasma edge, slowly penetrating to the core region. For further development of the simple models for particle sources and sinks, ASTRA predictions can be used as a reference. At this moment, the particle sources are included to the diffusion equation implicitly, since the electron density profiles are constructed with μ_{T_e} which is determined by the controller to match the prescribed n_{el} . However, the integrated value of the electron density does not provide an information on its local distribution.

In contrast to previous simulations with prescribed electron density profiles, here simulated n_e profiles are not affected by the presence of the NTM mode (Fig. 3.10 at $t = 0.88$ s and $t = 0.98$ s) which leads to different behavior of the electron density n_e and temperature T_e with H_e -factor the same as before. However, the pedestal height of n_e profiles decrease with n_{el} , which is affected by the presence of NTMs.

3.2.3 Simulation in case of off-axis heating

For the simulations discussed above, we use typical L- and H-modes H_e values obtained after analysis of various TCV discharges with dominant central heating or ohmic plasmas. However, there is a well known effect of the energy confinement degradation in case of a strong off-axis heating, in particular ECRH [Pochelon et al.(1998), Henderson et al.(2001), Sauter et al.(2001), Sauter et al.(2010)], due to a decrease of the central heat flux as has been

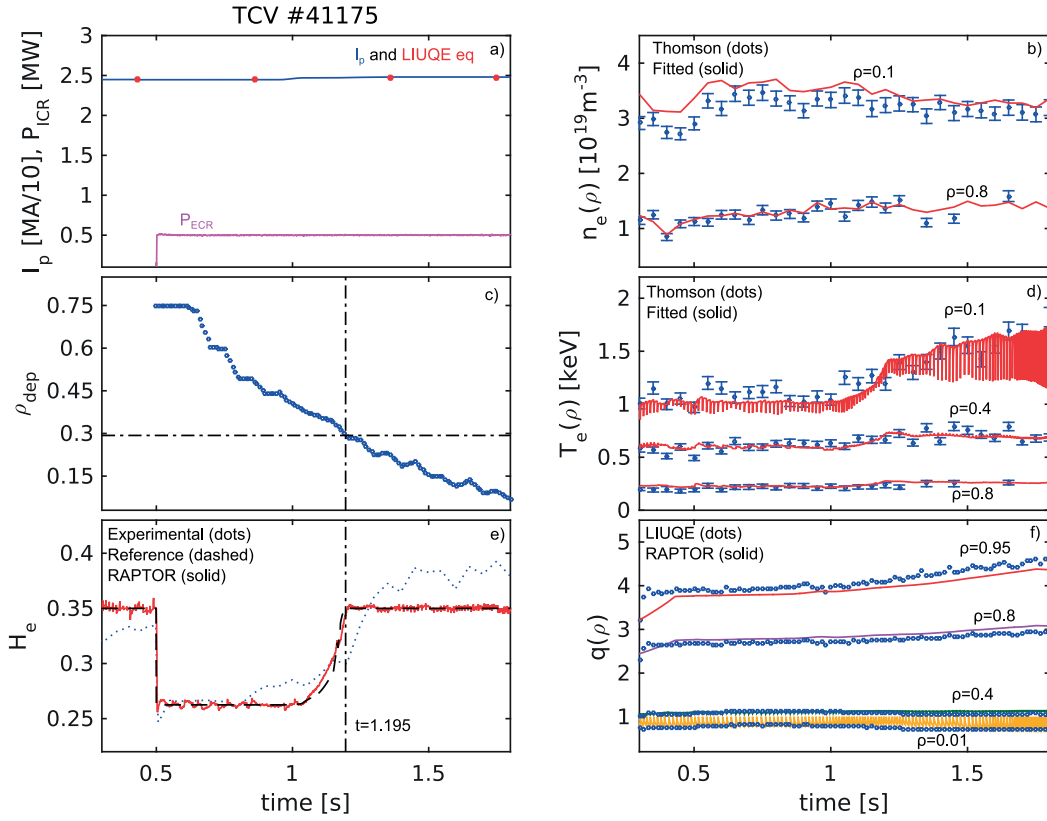


Figure 3.11: Simulation of the TCV shot #41175 with scaled H_e -factor. With prescribed plasma current I_p , ECR heating power P_{ICR} and radial deposition ρ_{dep} , H_e -factor and the electron density n_e fitted from Thomson measurements the RAPTOR code predicts time evolution of the electron temperature T_e and the safety factor q validated with Thomson measurements and LIUQE output correspondingly.

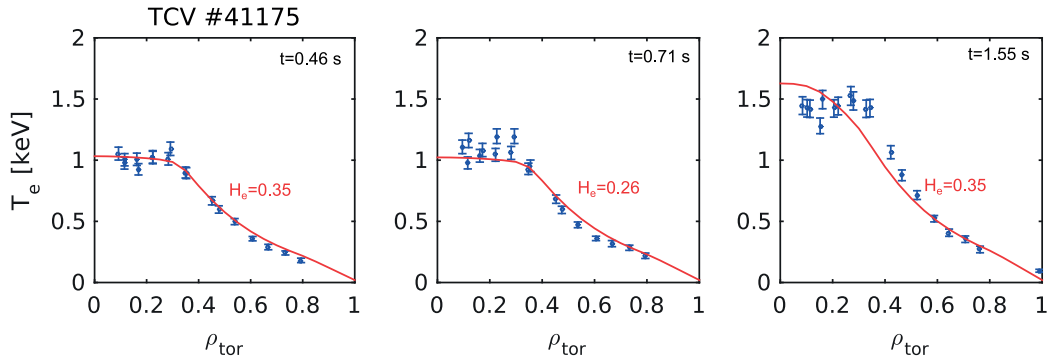


Figure 3.12: T_e profiles from Thomson measurements for TCV shot #41175 and RAPTOR simulation results at $t = [0.46, 0.71, 1.55]$ s.

shown for TCV [Camenen et al.(2005)] and AUG plasmas [Ryter et al.(2003)]. Simulation of a TCV plasma with standard transport model parameters will lead to an overestimation of the stored energy. Thus, an analytical function is required to relate the radial deposition of ECR beams (or any other heating source) and H_e -factor to take into account a reduction of the H_e -factor in case of off-axis heating. This is due to the fact that the confinement scaling laws, like the $H_{98,y,2}$ scaling law [ITER Physics Expert Groups(1999a)], are based on central heating scenario (best plasma performance).

A good example of a such plasma behavior is the TCV shot #41175 [Kirneva et al.(2012)], where the ECR launcher is slowly moving from outer region of the plasma ($\rho_{dep} = 0.75$ on the toroidal normalized grid) to the plasma central region ($\rho_{dep} = 0.07$) with almost constant flat-top plasma current, as shown in Fig. 3.11.a+c. For the following simulation of the electron temperature and the poloidal flux, we use prescribed profiles for the electron density $n_e(\rho, t)$ fitted from Thomson measurements (Fig. 3.11.b). The ECR power density profiles are approximated by Gaussian curves with a fixed width 0.2.

To simulate the confinement degradation because of strong off-axis ECR heating, a scaling parameter s_e for the H_e -factor is defined in the similar way as described in [Kim(2015)]:

$$s_e = 1 - 0.25 \left(1 - \exp \left(-4 \cdot \left(\frac{\rho_{dep}^3 - \rho_{inv}^3}{0.03} \right)^2 \right) \right) \cdot H(\rho_{dep} - \rho_{inv}); \quad (3.3)$$

where ρ_{dep} is the radial coordinate of the maximum of EC power density, ρ_{inv} is the inverse radius used for calculation of transport coefficients, H is the Heaviside function. The scaling factor s_e equals to 1 if the ECR launcher is located inside ρ_{inv} and reduces down to 0.75 if ρ_{dep} is far from the center. Parameters 0.25 and 0.03 are chosen for this particular case to match time evolution of experimental H_e -factor calculated with the $H_{98,y,2}$ scaling law [ITER Physics Expert Groups(1999a)]. The first one corresponds to 75% drop in H_e observed in the experiment. The second one is defined by the rate of change in the ρ_{dep} , which is rather small in this particular case.

Thus, the reference H_e^{ref} -factor for the χ_e transport model in Eq. 2.57 in this L-mode plasma is defined as:

$$H_e^{ref} = s_e \cdot H_e^{ref}(L) = s_e \cdot 0.35 \quad (3.4)$$

Experimental and reference H_e -factors are presented in Fig. 3.11.e). There is a drop in the energy confinement as soon as the off-axis ECRH is switched on at 0.5 s. The H_e -factor stays close to 0.26 (with $s_e=0.75$) up to 1 s. As the launcher radial position comes closer to $\rho_{inv} = 0.3$ the scaling factor s_e increases from 0.75 to 1. We have very good agreement between prescribed and simulated H_e -factors and T_e profiles are presented in Fig. 3.11.f).

It is clearly seen that the energy confinement improves while the launcher becomes more centrally localized, whereas we fix H_e at 0.35. T_e profiles are simulated with $\lambda_{T_e} = 3.2$ and are

close to Thomson measurements at $t=0.46$ s (ohmic) and $t=0.71$ s (ECRH) as shown in Fig. 3.12. However with central ECR heating at $t=1.55$ s, an improved confinement leads to increased λ_{T_e} which is 4 from Thomson measurements instead of 3.2. This actually means that the inverse scale length R/L_{T_e} depends on the ECR radial deposition, increasing while it becomes more centrally located [Camenen et al.(2005), Ryter et al.(2003)], but the effect is not significant. Instead of using constant λ_{T_e} , i.e. averaged TCV value 3.2 for L-mode, it can be recalculated according to ρ_{dep} of ECR and corresponding radial profiles of heat fluxes. However, a more careful study of relations between λ_{T_e} and the heat flux inside ρ_{inv} is required.

3.3 ASDEX Upgrade plasma modelling

We continue demonstrating the RAPTOR code capabilities as a reliable plasma simulator with various ASDEX Upgrade plasma discharges. On the AUG tokamak, the equilibrium code CLISTE is used for calculation of MHD equilibrium and the toroidal current density profile [Schneider et al.(2000)]. Also the integrated data analysis (IDA) [Fischer et al.(2003)] provides information about plasma equilibrium and profiles. The equilibrium data generated with the experimental codes are re-processed with the CHEASE code in the format required by RAPTOR.

3.3.1 Standard H-mode discharge

Here we consider a plasma discharge with two NBI beams. At the beginning of the flat-top phase, the plasma switches to H-mode (at 1.5 s) and stays in this state until switching off the NBI beams at 6.4 s.

Prescribed data set

A set of 14 equilibria is used for the description of the plasma geometry evolution. We start simulation with RAPTOR from the middle of ramp-up, with the first available equilibria at 0.5 s, and continue to the last available equilibria at 7.5 s reaching low plasma current 0.15 MA as presented in Fig. 3.13.a. Here, we assume that half of the total NBI power is absorbed by electrons, and their distribution profiles are approximated with Gaussian radial profiles of widths 0.5 with central deposition. A 10 ms time step is chosen and a simulation of the AUG plasma duration 7 s takes 1.5 min on a standard PC.

Transitions between L- and H-modes are specified from H_α measurements and fixed at 1.5 s and 6.4 s respectively. After analyzing a set of AUG discharges, the H_e -factor has been fixed at 0.2/0.35 for L-/H-mode. Similar to TCV simulations, the line-averaged density n_{el} is a prescribed parameter for the transport model of the electron density. Smoothed experimental signal of n_{el} is the reference for the feedback controller of the model (Fig. 3.13.b). From Table 3.2, obtained with the χ^2 test as for TCV simulations, the transport parameter λ_{T_e} has been fixed at 3.0 for L-mode and 2.3 for H-mode and λ_{n_e} is fixed at 1.0 and 0.5 for L- and H-modes

$\lambda_{T_e}(L)$	2.4	2.6	3.0	3.4	3.6
χ^2	10.5	8.6	6.7	7.3	8.5
$\lambda_{n_e}(L)$	0.4	0.6	1.0	1.4	1.6
χ^2	5.7	4.8	3.7	3.9	4.5
$\lambda_{T_e}(H)$	1.7	1.9	2.3	2.7	2.9
χ^2	8.7	7.4	7.0	10.0	12.1
$\lambda_{n_e}(H)$	0.3	0.4	0.5	0.7	0.9
χ^2	5.3	4.5	4.1	4.8	7.2

Table 3.2: The χ^2 tests for various AUG λ_{T_e, n_e} to define the goodness of the fit between RAPTOR simulated and Thomson measured T_e and n_e profiles.

correspondingly. For the RAPTOR sawtooth model, the critical shear is fixed at 0.3, typical value used for AUG plasmas simulations in RAPTOR to have sufficient time for recovery of the q profile and to match the experimental T_e crashes.

Predicted parameters

As it can be seen from Fig. 3.13.c, the time evolution of the RAPTOR q profile shows a good agreement with the simulation results of the equilibrium reconstruction code CLISTE at various radial coordinates. In addition to q profiles checked at radial coordinates [0.01, 0.4, 0.8] on the RAPTOR toroidal normalized grid $\hat{\rho}$, we consider the safety factor q at $\Phi/\Phi_b = 0.95$, which represents the safety factor at the flux surface which contains 95% of the toroidal flux Φ , instead of verifying the parameter q_{95} . The CHEASE code (and therefore, the equilibrium data provided to RAPTOR) does not consider the X-point configuration and, thus, assumes that the plasma is limited and the safety factor q has finite value at the edge.

The simulated plasma internal inductance $l_i(3)$ follows the experimental one very well for most of the plasma discharge (Fig. 3.13.e). We verify the time evolution of the internal inductance provided by RAPTOR comparing it with CLISTE output and a discrete set of l_i values obtained from CHEASE equilibrium data. Transition from L- to H-mode at 1.5 s is accompanied by a drop in the internal inductance l_i and is simulated both by RAPTOR and CLISTE. At the flat-top and up to half of the ramp-down phase, l_i from RAPTOR and CLISTE/CHEASE are very close to each other, showing similar values and trends. After 6.4 s we observe strong difference between RAPTOR and CLISTE/CHEASE internal inductance. The CLISTE code uses only the magnetic measurements to solve the Grad–Shafranov equilibrium equation. As in the case of LIUQE for TCV, the current density profile resistive diffusion is not taken into account. It might explain the difference in l_i evolution from 6.4 to 6.6.s where, after switching off the NBI beam, redistribution of the current density happens. Also, at 6.6 s the plasma is diverted with the plasma boundary elongation $\kappa_b \approx 1.5$, whereas at 6.8 s it is limited with $\kappa_b \approx 1.3$. It is known that in case of solving the Grad–Shafranov equilibrium equation for a near-circular plasma, the accuracy of the reconstructed poloidal beta β_p and the internal inductance l_i values strongly depends on the plasma elongation decreasing if plasma becomes closer to circular [Hofmann et al.(1988), Lao et al.(1985b), Cooper and Wootton(1982)]. Thus,

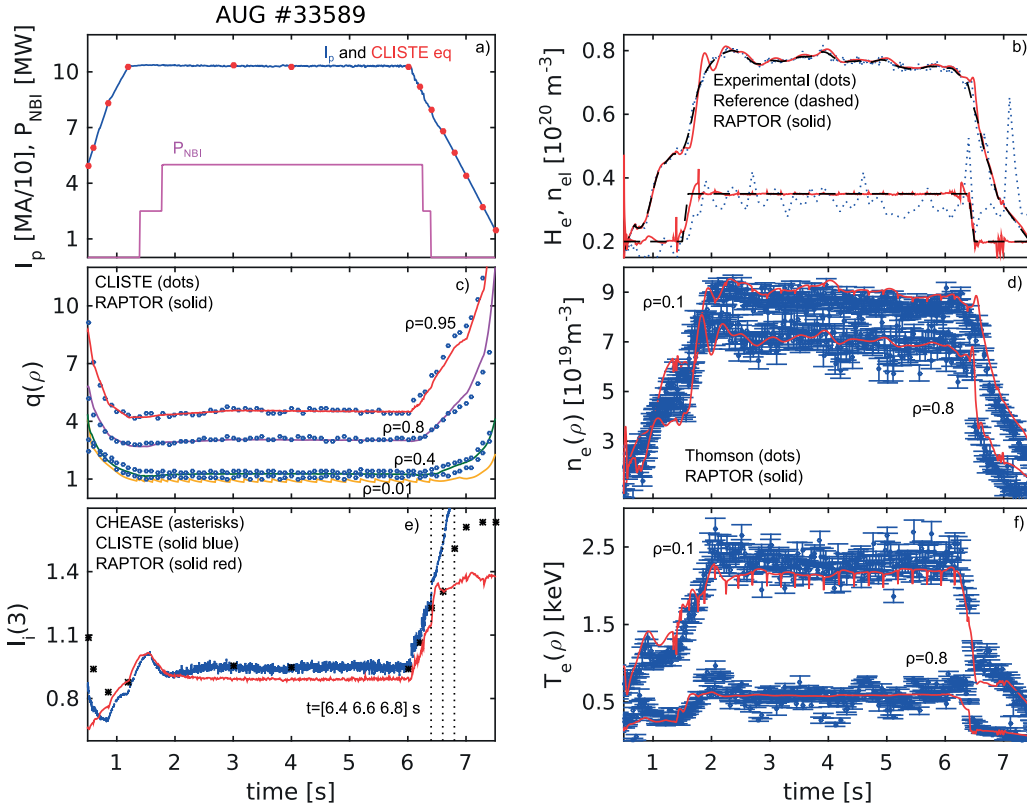


Figure 3.13: Prescribed time traces for the AUG shot #33589: the plasma current I_p and the NBI power P_{NBI} ; the line-averaged density n_{el} and the H_e -factor. Predicted parameters: the safety factor $q(\rho)$ and the internal inductance l_i validated with CLISTE output; the electron density n_e and temperature T_e checked with Thomson measurements.

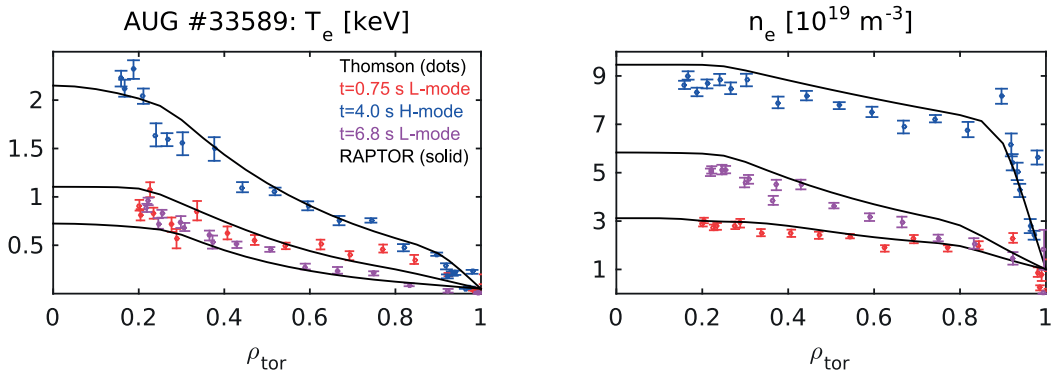


Figure 3.14: Electron temperature T_e and density n_e profiles from Thomson measurements for the AUG shot #33589 and RAPTOR simulation results at $t = [0.75, 4.0, 6.8]$ s.

the internal inductance l_i provided by the CLISTE code for the time period from 6.6 s to 6.8 s might be estimated inaccurately.

From Fig. 3.13.d+f it can be seen that the electron density n_e and temperature T_e simulated with RAPTOR are within the experimental error bars. We check their time evolution at two radial coordinates: close to the center $\hat{\rho} = 0.1$ and around the pedestal $\hat{\rho} = 0.8$. Duration of transition phases between L- and H-modes is equal to 0.1 s. This value is suitable both for the electron density and temperature time evolution. The radial profiles for T_e and n_e at several time instants are demonstrated in Fig. 3.14. The pedestal can be easily recognized in H-mode at 4 s.

3.3.2 AUG H-mode discharge with time-varying transport gradients

For further development of the model, predictive simulations for ψ and T_e have been performed for the AUG shot #32546. Here in addition to NBI, we have ECRH heating. ECRH power density profiles are approximated with Gaussian curves with central deposition and widths 0.04, forming narrow profiles. As in the previous AUG simulation, we assume that electrons absorbed half of NBI and total ECRH heating power. Electron density profiles are fitted from Thomson measurements. The transport parameter λ_{T_e} is fixed at 3.0/2.3 for L-/H-mode, and H_e is equal to 0.2/0.35 for L-/H-mode, as in the previous section. Transition from L- to H-mode is fixed at 0.7 s according to the H_α signal. In the ramp-down phase, due to W accumulation and to match the experimental drop in electron temperature T_e , the H_e factor is changed from 0.35 to 0.2 at 8.1 s instead of 8.55 s, when H-L transition is observed with the H_α signal. Also to mimic the flattening of the electron temperature profiles in the time period [8.1 8.55] s, λ_{T_e} takes a value of 1.2. These changes are not “predicted” within the RAPTOR model at this stage, one would need an advanced impurity and ELM control model. However, it would be rapidly observed in real-time and therefore can be adapted easily in real-time.

With this predictive simulation, which results are presented in Fig. 3.15, we have obtained a very good agreement with the safety factor and the internal inductance, provided by CLISTE and CHEASE codes. The electron temperature from RAPTOR at $\hat{\rho} = 0.1$ is slightly lower than Thomson measurements, whereas at $\hat{\rho} = 0.8$ they are very close during the entire discharge. If we look closer to T_e profiles presented in Fig. 3.16.a), it is clear that some profiles are more peaked in the very central region, whereas in the “stiff” region (between $\hat{\rho} \approx 0.2$ and $\hat{\rho} \approx 0.8$) electron temperature profiles from RAPTOR follow Thomson measurements very well both in L- and H-mode. As it has been demonstrated also with the TCV shot #41175, the presence of ECRH might lead to centrally peaked T_e profiles.

This shot is also interesting because of impurity accumulation in the ramp-down phase, which leads to flattening in T_e profiles and sudden drop in l_i . To get the T_e profiles evolution similar to experimental measurements, we need to reduce λ_{T_e} from 2.3 up to 1.2 after 8.0 s. In Fig. 3.16.b) we demonstrate T_e profiles predicted by RAPTOR, which are very close to Thomson measurements. For this simulation, we prescribe the time evolution of λ_{T_e} based on the

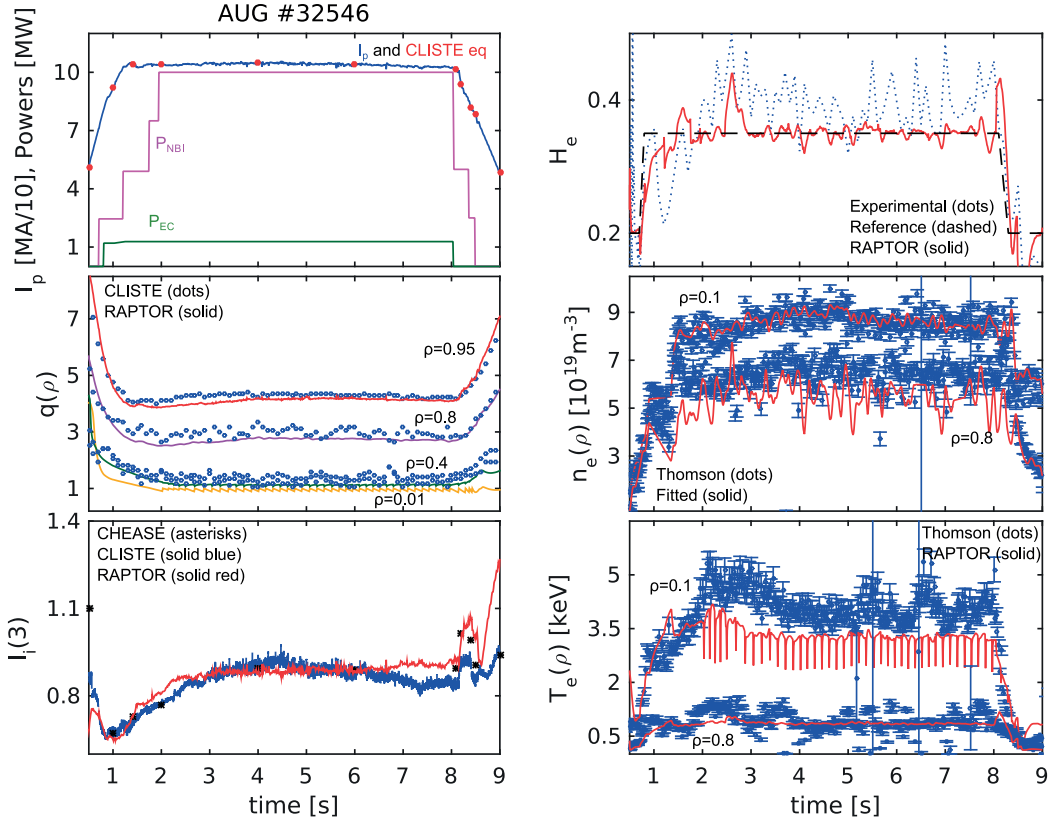


Figure 3.15: Prescribed time traces for the AUG shot #32546: the plasma current I_p , NBI P_{NBI} and ECRH P_{ECRH} heating powers ; the H_e -factor; the electron density n_e fitted from Thomson measurements. Predicted parameters: the safety factor $q(\rho)$ and the internal inductance I_i validated with CLISTE output; the electron temperature T_e checked with Thomson measurements.

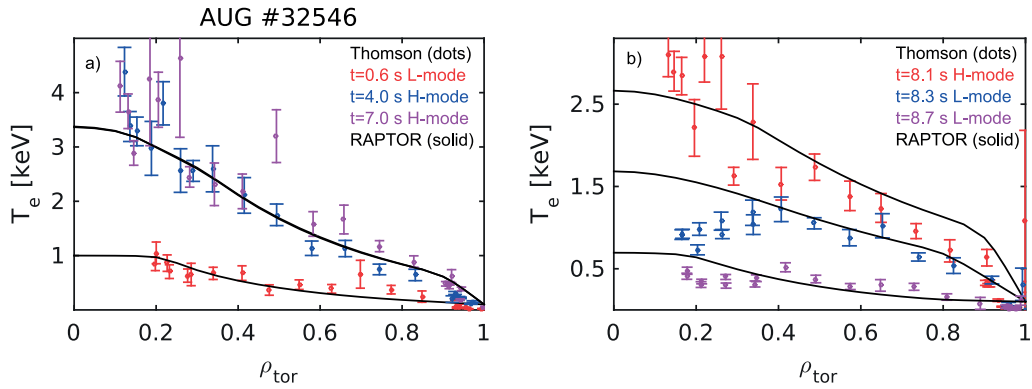


Figure 3.16: Electron temperature T_e profiles from Thomson measurements for the AUG shot #32546 and RAPTOR simulation results a) at $t = [0.6, 4, 7]$ s with $\lambda_{T_e} = 3.0/2.3/2.3$ for L-/H-/H-modes and b) at $t = [8.1, 8.3, 8.7]$ s with $\lambda_{T_e} = 1.2/1.2/3.0$ for T_e profiles flattening.

experimental measurements. However, as a further step of the model development, λ_{T_e} can be defined as a function of the electron heat flux [Ryter et al.(2003)]. Thus, if a strong reduction is observed from experiment (or predicted by a simulation), λ_{T_e} will be automatically decreased. We will also show a capability of the RAPTOR code to simulate hollow temperature profiles with modelling of JET plasmas in Subec. 3.4.2.

3.4 JET plasma modelling

This section is dedicated to simulations of JET plasma discharges. Since ASDEX Upgrade and JET tokamaks have similar aspect ratio and collisionality, we expect that the same transport model parameters will be appropriate for JET plasma modelling too. There are two main external heating sources for JET: NBI beams and ICRH waves. For JET discharges with central ICRH we expect to have rather long sawtooth period, much longer than the heat confinement time, because of fast ions stabilization with the NBI and ICR core heating [Angioni et al.(2002)]. For the following JET simulations, the critical shear is fixed at 0.4 to have a few big sawtooth crashes. The equilibrium data required by RAPTOR are provided by the equilibrium reconstruction code EFIT [Lao et al.(1985a)] and re-processed by the CHEASE code in the same way as for TCV and AUG.

3.4.1 An entire shot simulation

Here we present the simulation of the JET shot #92207 with long ramp-up and -down phases with dominant NBH and ICRH.

Prescribed parameters

A set of 19 EFIT equilibria is used to describe the discharge from 42 s to 62 s (Fig. 3.17.a). We approximate power density profiles for NBH with broad Gaussian curves with width $w_d = 0.4$ and central deposition. Power density profiles for ICRH have central deposition and width 0.15. For JET the PENCIL code [Stubberfield and Watkins(1987)] is used for calculation of NBI heating profiles and its absorption by various plasma species, and the PION code [Eriksson et al.(1998)] is used for ICRH. According to experimental signals stored in JET database, electrons absorb, on average, half of the total input power. Transitions from L- to H-mode and back are fixed at 47 s and 52 s correspondingly with duration 1 s to stay in agreement with the H_α signal. Simulation of the JET plasma with a 10 ms time step takes 4 min on a standard PC.

The transport parameters λ_{T_e} and λ_{n_e} are equal to 3.0/2.3 and 1.0/0.5 for L-/H-mode as for AUG simulations. The H_e -factor from the experimental databases is rather close to L-/H-values used for AUG discharges too. However, H-mode is characterized by two values: 0.35 (as for AUG H-mode) for maximum NBI power and 0.25 after 50.5 s with a half of the NBI power Fig. 3.17.b. It might be related to the power redistribution between electrons and ions

Chapter 3. Entire shot simulations with the RAPTOR code

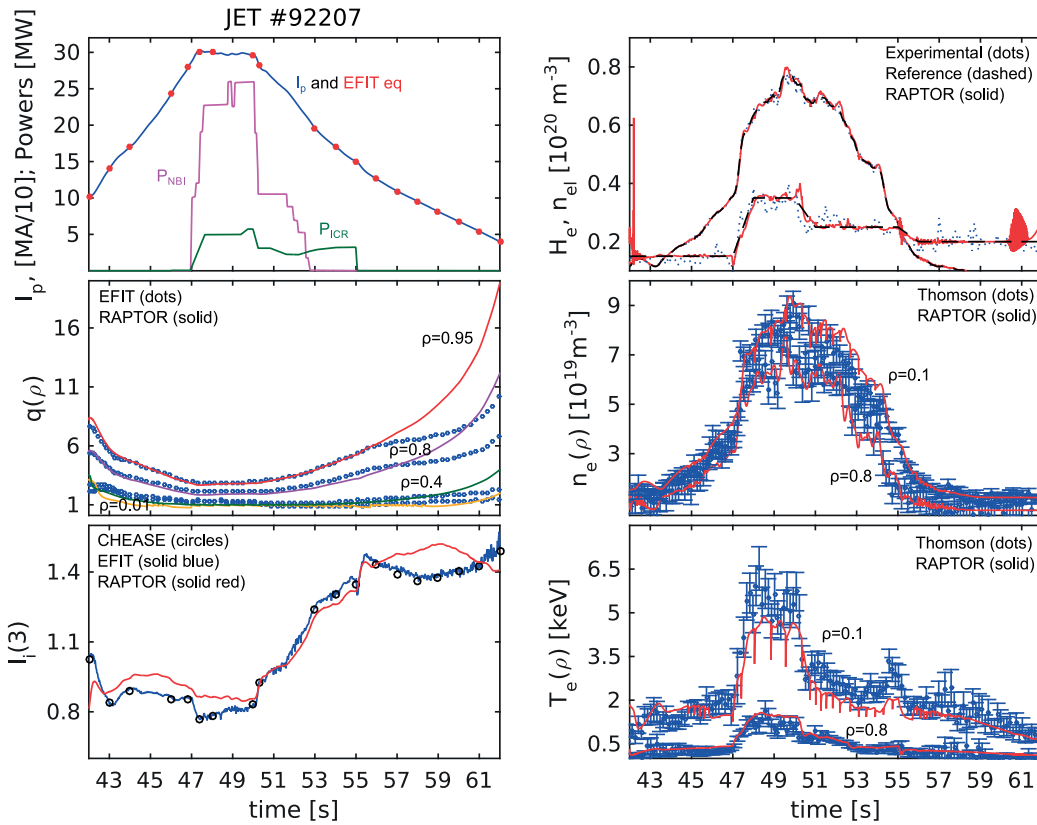


Figure 3.17: Prescribed time traces for the JET shot #92207: the plasma current I_p , the NBI power P_{NBI} and the ICR power P_{ICR} ; the line-averaged density n_{el} and the H_e -factor. Predicted parameters: the safety factor $q(\rho)$ and the internal inductance l_i validated with EFIT output; the electron density n_e and temperature T_e checked with Thomson measurements at $\rho = 0.1$ and around the pedestal area $\rho = 0.8$.

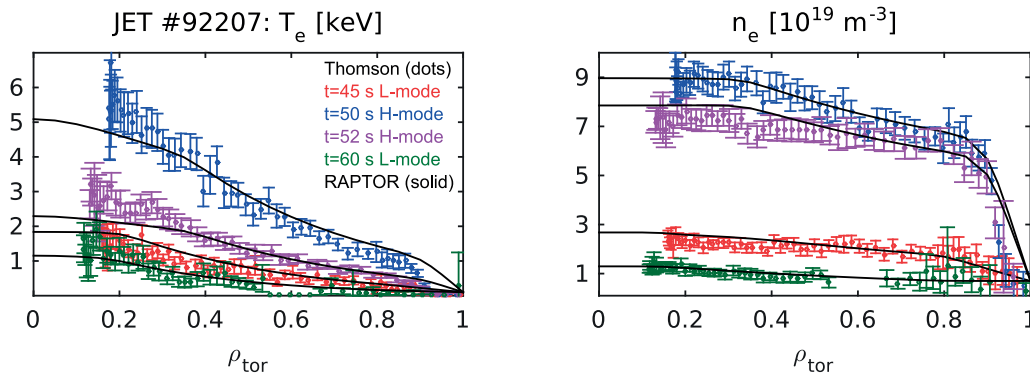


Figure 3.18: Electron temperature T_e and density n_e from Thomson measurements for JET shot #92207 and RAPTOR simulation results at $t = [45, 50, 52, 60]$ s.

after a huge drop in the NBI power. According to PENCIL calculations, after the NBI drop 60% of absorbed power goes to electrons, but it would be worth analysing in more details. In particular, electron and ion heating can be estimated with analytical formulas which include dependence on the beam energy and the electron temperature [Wesson(2004)] (and references therein related to the chapter focused on NBH), thus helping to get a correct fractions of the absorbed power. The absorbed power ratio can be written as:

$$\frac{P_i}{P_e} \sim \frac{T_e^{3/2}}{w_b} \quad (3.5)$$

where w_b is the beam energy. Thus, with higher electron temperature more NBH power is absorbed by ions.

Predicted parameters

Firstly, as for TCV and AUG, we check the time evolution of the safety factor q at various radial coordinates and l_i . As it can be seen from Fig. 3.17, up to the middle of the ramp-down phase there is good agreement between RAPTOR and EFIT simulation results. However, starting from 56 s, q from RAPTOR increases much faster than the one from EFIT. Further analysis is required to understand the main reasons, leading to the strong change in slope of q profiles provided by EFIT and to check the input parameters assumed for EFIT late phase.

With Thomson measurements we can verify the time evolution of the electron temperature T_e and density n_e profiles presented in Fig. 3.18. The prescribed shapes and pedestal position corresponds to experimental observations. We also see that RAPTOR provides a good prediction for the profiles at the very edge where we lack experimental measurements.

Influence of ρ_{inv} definition

Note that as well as for TCV and AUG plasmas modelling, the inversion radius ρ_{inv} is defined as a radial coordinate of $q = 1$ surface before a sawtooth crash. Thus transport between ρ_{inv} and $\rho = 0$ is defined by a constant electron heat diffusivity χ_{ST} equal to 5 [m²/s] for JET plasmas. We have a few big sawtooth crashes and it takes around 0.5 s for the shear to reach its critical value 0.4. For this simulation ρ_{inv} is around 0.35. In Fig. 3.18 it can be mentioned that T_e profiles simulated with RAPTOR within ρ_{inv} are more flat than profiles observed with the Thomson scattering system.

If we fix the inverse radius at $\rho_{inv} = 0.2$, i.e. assume that $\rho_{inv} < \rho_{q=1}$ the electron heat diffusivity χ_e is partly defined with the logarithmic gradient λ_{T_e} inside the sawtooth affected area (the reconnection radius), obtained temperature profiles match the experimental measurements much better in time and space as shown in Fig. 3.19. The transport model can be extended for this case with a special radial-dependent λ_{T_e} for the region inside ρ_{inv} to vary the T_e profile gradually from λ_{T_e} to a flat profile. Note that a more detailed study with coherent averaging of profiles just before and right after the sawtooth crashes should be performed.

Chapter 3. Entire shot simulations with the RAPTOR code

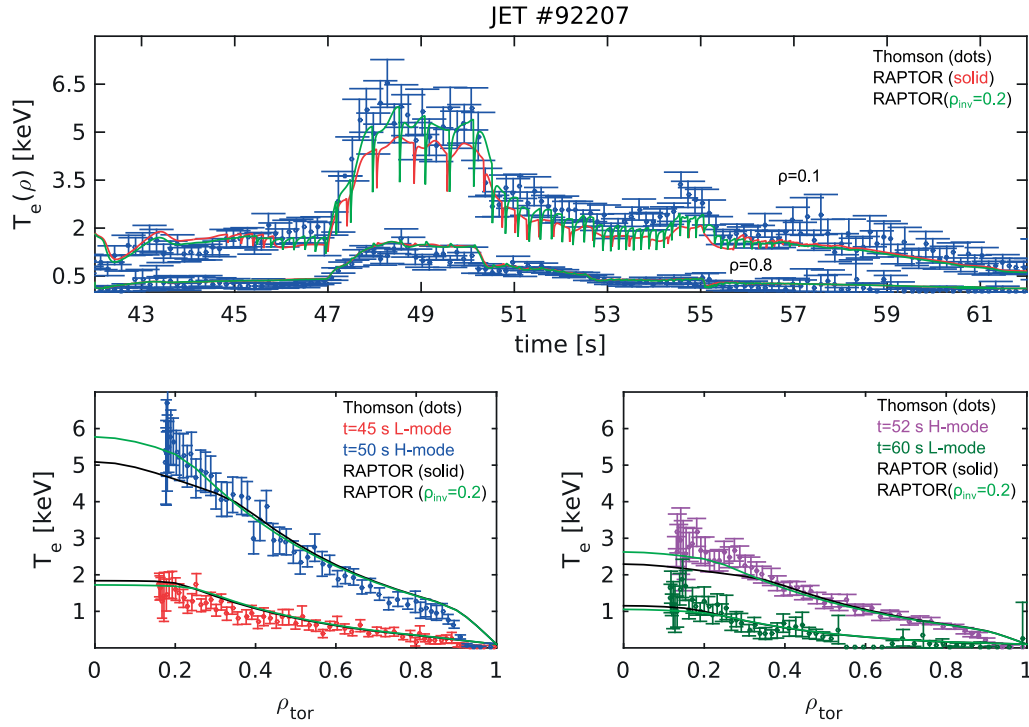


Figure 3.19: Electron temperature time traces and profiles simulated with RAPTOR in case of time-varying ρ_{inv} (red in the top plot and black in the bottom plots) and fixed $\rho_{inv} = 0.2$ (green) for the JET shot #92207. Experimental Thomson measurements are marked by dots (blue in the top plot and other colors in the bottom plots).

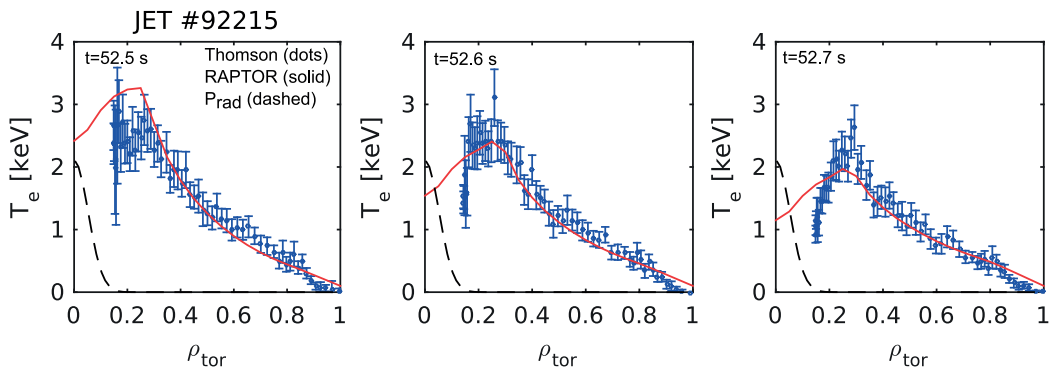


Figure 3.20: Electron temperature profiles for the JET shot #92215 simulated with RAPTOR with extra central radiated power for the time period 52-53 s. Thomson measurements are marked in blue dots. Normalized profile for the radiated power density P_{rad} is marked in dashed black line.

3.4.2 Simulation of hollow profiles for the electron temperature

Another important issue for profiles modelling, and JET plasmas in particular, is the generation of hollow electron temperature profiles. Such profiles are usually formed in case of strong central radiation following impurity accumulation, thus cooling of the plasma core which may lead to a plasma disruption [De Vries et al.(2014)]. Since in the RAPTOR code we do not have a proper model for impurity transport and accumulation, the radiated power is modeled mainly with the Bremsstrahlung model. We can add manually an external source of the radiated power to simulate increased radiation for electrons because of impurity accumulation.

In Fig. 3.20, predictive simulation of hollow profiles for the JET shot #92215 is presented. A constant source of radiated power (4.5 MW in total) is added in the plasma center. According to the JET experimental signals, integrated Bremsstrahlung radiation at 52-53 s is around 0.2 MW, close to the values obtained with RAPTOR. Total radiated power measured by bolometers is around 8 MW. For simulation we use 4.5 MW, assuming that half of radiated power is generated by electrons through interaction with heavier plasma species. More accurate estimation of distribution of the radiated power between plasma compounds requires profiles of impurities.

Since for the T_e diffusion equation P_{rad} is a sink, negative heat flux is generated in the plasma center. For L-mode plasma simulation we use $\lambda_{T_e} = 2.0$ instead of 3.0 to match experimental profiles. It can be explained by a reduction of the heat flux because of a strong sink in the center.

3.5 Summary

In this chapter we demonstrate the capabilities of the RAPTOR code to predict the evolution of the poloidal flux and the electron temperature and density in space and time. Thanks to the code upgrades, presented in Chapter 2, the influence of the plasma equilibrium and geometry on plasma profiles is taken into account during simulations of entire plasma discharges, i.e. from ramp-up to ramp-down. The gradient-based transport model, described in Sec. 2.6, enable fast simulations of a plasma in low (L) and high (H) confinement modes with a small set of prescribed parameters, most of them a constant over the entire discharge. With the simulations presented in this chapter, we are aiming to reach several goals: validation of the new transport models implemented into the RAPTOR code; determination of typical ranges for transport parameters for realistic simulations of TCV, AUG and JET plasma profiles; analysis of special cases for which they do not match.

With the transport coefficients, described in Sec. 2.6, the shape of the plasma profiles for electrons in the “stiff” region is characterized by a constant logarithmic gradient. Since there are no scaling laws to estimate the height of the pedestal for T_e and n_e profiles, it is defined with integrated parameters prescribed from experiments: the confinement factor for electron energy H_e for T_e profiles and the line-averaged density n_{el} for n_e profiles. Assuming that there is no local improvement or degradation in electron energy confinement, we can fix H_e for L-

and H-mode separately. But for n_{el} full time evolution is required.

Starting with TCV simulations, presented in Sec. 3.2, we validate transport models for T_e and n_e , since initially they have been developed for TCV plasmas [Sauter et al.(2014), Kim et al.(2016)]. Typical gradients λ_{T_e, n_e} for the “stiff” region have been defined and successfully tested in L- and H-mode plasmas. We have found that $\lambda_{T_e} = 3.2/2.3$ and $\lambda_{n_e} = 2.0/1.0$ for L-/H-mode give the best match with Thomson measurements. Also H_e factor has been fixed at 0.35 and 0.45 for L- and H-mode correspondingly. RAPTOR simulation results have been validated with LIUQE output and Thomson measurements, showing very good agreement for various plasma parameters and heating conditions. With similar approach, for AUG plasmas we have defined typical values of λ_{T_e, n_e} , where $\lambda_{T_e} = 3.0/2.3$ and $\lambda_{n_e} = 1.0/0.5$ for L-/H-mode. The values of λ_{T_e} obtained for AUG are very similar as for TCV, as expected, while the values of λ_{n_e} a factor of two smaller, both in L- and H-modes. The latter might be explained by the fact that the ratio T_e/T_i is lower for AUG than for TCV and the critical R/L_{n_e} is lower as well. A more detailed analysis would be worth while but is out of scope of this work. It is important to note that the model works equally well on AUG as on TCV, for entire discharges. This is the case for JET as well. For AUG simulations, H_e is fixed at 0.2/0.35 for L-/H-modes, while for JET it is 0.2 for L-mode and 0.35/0.25 for H-mode. The last variation comes from NBI heating, which higher level leads to higher H_e , what might be related to the energy exchange between electrons and ions. This effect can be included into RAPTOR simulations at a later stage using Eq. 3.5 for the absorbed power ratio. For JET simulations, the same values of λ_{T_e, n_e} as for AUG have been obtained, confirming the validity of this new model. With the few parameters, RAPTOR simulation results match the experimental profiles very well (from center to the very edge) in ramp-up, flat-top and ramp-down phases, for TCV, ASDEX Upgrade and JET L- and H-modes and transition phases.

In this chapter, we have also discussed several special cases when the set of parameters described above is not valid. NTMs can change locally T_e and n_e profiles, leading to heat and particle confinement degradation. Here we do not simulate NTMs by RAPTOR, therefore profiles of the transport coefficients are not affected by their presence. It results in some difference in T_e and n_e profiles shape predicted by RAPTOR and measured by the Thomson diagnostic, as it has been shown with TCV H-mode simulations in Subsec. 3.2.2. This problem can be solved by consistent simulations of NTMs and plasma kinetic profiles (under development). Off-axis heating leads to heat confinement degradation (as compared to scaling laws), thus an option to have H_e factor depending on the radial deposition of ECRH has been added, as described in Subsec. 3.2.3. In case of strong impurity accumulation, T_e and n_e profiles can become flat or even hollow, as it has been shown for AUG and JET shots in Subsec. 3.3.2 and 3.4.2. We can reproduce shape of T_e profiles by adjusting λ_{T_e} . Profiles flattening is caused by a reduction of the heat flux in the “stiff” region, thus, the heat flux can be used as an indicator defining periods of reduced λ_{T_e} . Of course this could be coupled to the neural network transport models like QuaLiKiz [Bourdelle et al.(2016)] which is providing expected heat flux.

Thus, we conclude that with the obtained λ_{T_e, n_e} , realistic shape for T_e and n_e profiles can be predicted for TCV, AUG and JET plasmas including the pedestal regions. Future upgrades of the model are related to proper NTMs simulation and implementation of the radial-dependent λ_{T_e, n_e} to take into account strong changes in the heat flux. To define the pedestal height, parameters based on experiments, H_e and n_{el} , are required. However, if the μ_{T_e, n_e} is known from a simulation, and there is an experiment with similar density evolution, then for modelling of this experiment, known μ_{T_e, n_e} can be used. Thus we can save CPU time, required for calculations, since the PI controller to estimate μ_{T_e, n_e} is not needed anymore. One could also use, in H-modes, information about the expected pedestal height and width from EPED-like models [Snyder et al.(2011), Meneghini et al.(2017)].

4 Optimization of the ramp-down phase

Development of non-disruptive operational scenarios is an important issue for future machines like ITER. Because of the large amount of energy stored in burning plasmas, significant heat fluxes to the first wall of a machine are expected during disruptions and can lead to serious damages of the first wall. Moreover, the vacuum vessel can experience critical electromagnetic forces produced by large poloidal currents generated in the machine structures [Wesson(2004), ITER Physics Expert Groups(1999b)]. Since the construction of future tokamaks allows only a very limited amount of disruptions at the full plasma current I_p , one of the most important research directions for existing machines is the development of specific techniques for disruption avoidance and plasma control. Design of feedback controllers and their integration into tokamaks magnetic and kinetic control systems is an essential part of ongoing experimental plasma research [Humphreys et al.(2015), Moreau et al.(2011), Barton et al.(2015)]. For a successful operation of a tokamak, a plasma must be well controlled during all stages of the discharge: ramp-up, flat-top and ramp-down. Stabilization of the plasma shape and position and a proper kinetic pressure/power balance have to be reached during the initial stage of a plasma discharge while the plasma thermal energy increases with plasma current. Various problems, like ensuring of MHD stability and sufficient growth of the plasma density, have to be solved to bring a plasma to a desired state at the end of this stage and, thus, at the beginning of the flat-top phase. Scenario development for most existing tokamaks is focusing on flat-top, the high performance phase of a plasma discharge, where the main plasma characteristics like MHD stability and particle and heat confinement are investigated. For ITER, the burning plasma will be developed during the flat-top phase, thus specific techniques for the plasma burning start and termination have to be determined. The main goal of the last stage of a plasma discharge is a safe plasma shut-down, which includes the termination from the burning phase in case of presence of fusion during the main phase. This thesis contributes to the development of termination scenarios for TCV, AUG and JET tokamaks.

Plasma disruptions are the most undesirable events during the ramp-down phase. Therefore the main goal of the development of termination scenarios is to find a route to ramp down si-

Chapter 4. Optimization of the ramp-down phase

multaneously the plasma current I_p , thermal energy and particle density while keeping plasma position and shape well controlled and avoiding any disruptions. The forces, acting on the vacuum vessel, are proportional to I_p^2 in case of disruptions which is why the plasma current has to be reduced quickly [ITER Physics Expert Groups(1999b)]. Presently termination scenarios for different tokamaks are designed with the help of experimental and numerical studies. Full discharge simulations with the DINA [Khayrutdinov and Lukash(1993), Favez et al.(2002)] code coupled with CRONOS [Basiuk et al.(2003)] and CORSICA [Crotinger et al.(1997)] have been performed for ITER [Kim et al.(2009), Casper et al.(2014)]. Termination phase studies with the JETTO [Cenacchi et al.(1988)] code and the JINTRAC suite of codes [Romanelli et al.(2014)] have been obtained for JET [Nunes et al.(2011), Bizzaro et al.(2016), Koechl et al.(2017)]. For better understanding of transport in the current ramp phases, numerical studies with the ASTRA code [Pereverzev and Yushmanov(2002)] have been performed for the ASDEX Upgrade tokamak (AUG) [Fable et al.(2013), Fietz et al.(2013)]. However, these numerical and experimental tests have been carried out only for a few particular cases without a systematic study of various ramp-down trajectories. Thus a trajectory, optimal in terms of the phase duration, plasma geometry etc., can be easily missed.

This chapter is dedicated to the development and testing of an automated numerical algorithm for an optimization of the ramp-down phase of a tokamak plasma. The goal of the present optimization procedure is to minimize the plasma current as fast as possible while avoiding any disruptions but staying well below technical limits specific for a machine. Note that the goal is implemented through the minimization of a cost function. We will show that it is relatively easy to change this cost function to match different desired goals. From theory, scientists know about general physical issues which can lead to plasma instabilities and result in plasma disruptions. These physical issues are common to most tokamaks. However, each machine also has some special technical characteristics and a specific operating domain with well controlled plasma. Thus, a combination of physical and technical characteristics, which will be discussed in detail below in Sec. 4.1, defines an operational domain which is safe in the sense that the plasma is non-disruptive. We will show that the RAPTOR code, with updates presented in Chapter 2 and validated in Chapter 3, can be used for a ramp-down optimization for the TCV, AUG and JET tokamaks. Due to its short wall-clock simulation time, the RAPTOR code is an efficient tool for automated ramp-down optimization, since many termination trajectories can be tested in a reasonable time (hours). Thanks to extensions in the RAPTOR code, developed as a part of this thesis, we can predict evolution of the plasma state during the ramp-down phase taking into account dynamics of the plasma geometry and electron heat and particle profiles. Our numerical study of this problem shows that a fast decrease of the plasma elongation during the current ramp-down can help in reducing the plasma internal inductance, thus reducing the risk of developing of a plasma vertical instability. This effect is also very important for the ITER operation in future as it was shown in the experimental studies of the ITER demonstration discharges [Sips et al.(2009)]. An early transition from H- to L-mode allows to reduce the drop in poloidal beta which is also important for plasma MHD stability and control. We show how these complex nonlinear interactions can be optimized

automatically using relevant cost functions and constraints for various tokamaks.

The chapter is organized as follows. Firstly in Sec. 4.1, we discuss the main problems during ramp-down. Then the optimization algorithm is presented in Sec. 4.2. In particular, optimization parameters and the cost and constraint functions are defined. Then we present results of the numerical optimization for TCV in Sec. 4.3, AUG in Sec. 4.4 and JET in Sec. 4.5, in addition discussing performed and possible experimental tests. Sec. 4.6 is dedicated to testing sensitivity of the optimized trajectories to the transport model parameters and geometrical quantities. In Sec. 4.7 the chapter summary is provided.

4.1 Overview of the ramp-down issues for a tokamak plasma

The power sources and plasma current decrease during the termination phase causing fast changes in plasma state, supplemented by a strong coupling between physical parameters and technical requirements. One of the difficulties is the control of the plasma position. While the plasma current decreases, the internal inductance increases leading to a smaller efficiency of the vertical control system. If the internal inductance increases too quickly, so that the vertical control system can no longer stabilize the vertical instability, then the plasma will disrupt, typically with a vertical displacement event (VDE). VDEs are characterized as the most dangerous plasma events for ITER [Putvinski et al.(1997)]. However a proper evolution of plasma shaping can reduce the growth of the internal inductance. Simulations of ITER plasma [Kim et al.(2009)] and experiments on JET [Nunes et al.(2011)] have shown a strong effect of elongation on the internal inductance behavior.

In addition to the vertical control, the radial position control has to be carefully implemented. A rate of change in a vertical magnetic field is limited by the rate of change in currents in the poloidal field coils. By definition from [Shafranov(1966), Wesson(2004)] the vertical magnetic field is approximately given by

$$B_v = \frac{\mu_0 I_P}{4\pi R} \left(\ln \left(\frac{8R}{a\kappa^{0.5}} \right) + \beta_p + 0.5l_i(3) - 1.5 \right) \quad (4.1)$$

Since it is a function of plasma current, internal inductance, elongation and β_{pol} , radial position control can be lost in case of rapid changes in the mentioned parameters. As a consequence, plasma position and shape control systems should be developed using knowledge of the evolution of the plasma profiles, i.e. integration of magnetic and kinetic control is required.

For a good performance, plasmas are generally operated in a high confinement mode (H-mode). During the termination phase, with the reduction in the plasma current and mostly auxiliary power, it comes back to a low confinement mode (L-mode). Because of the transition from H- to L-mode, the plasma experiences a fast decrease of energy and pressure. In particular, it can lead to a significant drop in β_{pol} , faster than can be compensated by reducing the vertical field and the plasma can make contact with the inner wall [Lister et al.(2013)]. In

Chapter 4. Optimization of the ramp-down phase

[Leonov et al.(2010)] two scenarios of ITER plasma termination were demonstrated: with H-L transition and in pure H-mode. It was shown that the internal inductance in the first case stays lower, whereas the drop in β_{pol} was smaller in the second case. Therefore the moment of the H-L transition is quite important for a plasma position control and for a safe termination and it has to be specifically defined as will be shown in Sec 4.4. It should be mentioned that a fast growth of radiated power can also lead to H-L transition [ITER Physics Expert Groups(1999a)].

During the plasma current ramp-down, the electron density has to be decreased to avoid disruptions caused by reaching the Greenwald density limit which depends on the plasma current. At the same time, the power load on the divertor has to be controlled. The dependence of the SOL and divertor parameters, like divertor power load, normalized neutral pressure and divertor neutral pressure, on the fueling scenario was shown in [Imbeaux et al.(2011)]. The core density can be controlled by pellets injection, whereas edge density is influenced by neutral gas puffing. In particular during the termination of an ITER plasma, transition from a regime with 80% of gas puff and 20% of core fueling to one with only pellet injection allows plasmas to stay attached with the normalized neutral pressure lower than one. However the control of density and its simulation is left for future studies. At this stage we assume that the density control system can provide the required line-averaged density. We only enforce a constraint such that it does not violate the Greenwald density limit or a fraction of it for safety margin. Note that this would lead to a constraint on the I_p ramp rate since the particle confinement time is relatively long up to 5-10 times greater than the energy confinement time [Becker(1988)].

Efficient tools for a systematic analysis of plasma disruptions have been developed in recent years. Multi-machine disruption database collect the information through analysing experimental data [De Vries et al.(2012), De Vries et al.(2014)] and provided by automated algorithms of disruptions detection and prediction [Pau et al.(2017)]. This approach allows to extend our knowledge on physical processes of disruptions and to define special issues, which are common for existing machines and might be used for the non-disruptive scenario development on future devices. In particular for the ramp-down phase, i.e. in case of fast changes in the plasma shape and equilibrium, machine operational limits can be extracted from the disruption database.

We are also interested in a proper control of plasma instabilities to avoid such unfavorable events for a plasma performance and a machine, like strong heat and particle confinement degradation because of the impurity accumulation or a massive power exhaust to the divertor plates. The latter can be controlled with a gas puff or pellet injection, changing ELMs frequency [Horton et al.(2004)]. Also the efficiency of a fast vertical plasma motion (vertical kicks) in ELMs frequency control has been demonstrated on JET [De la Luna et al.(2016)]. The sawtooth destabilization by proper heating scenarios may prevent an impurity accumulation in the plasma core [Nave et al.(2003)].

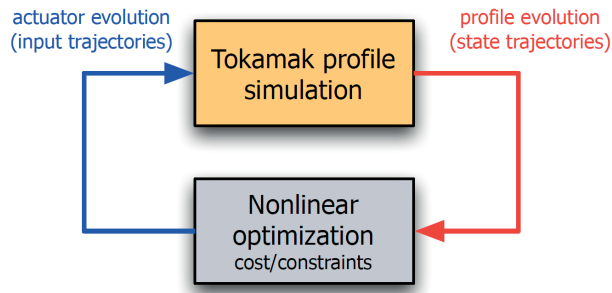


Figure 4.1: The scheme of the nonlinear procedure for the actuator trajectories optimization. Reproduced from [Felici(2011)].

4.2 Formulation of the optimization problem

An optimization of the plasma discharge can be defined as the determination of an optimal time evolution of the plasma parameters to lead a plasma to a desired state keeping it within the specific limits: physical ones (to avoid appearance of physical events which can lead to instabilities and then to disruptions) and technical ones (to be able to use the results of the optimization on a real machine). The parameters to optimize are related to those controllable inputs that have the capability of significantly changing the plasma state. Such actuators can act on a plasma either from inside (like the power of auxiliary heating and the noninductive current drive, particle injection) or from outside (like a gas flux, plasma shaping parameters). The profile of the poloidal flux ψ is strongly influenced by the plasma current density (for which the ohmic part depends on $T_e^{3/2}$ through the plasma conductivity), whereas the electron temperature profile T_e depends mainly on power density profiles, impurity accumulation and geometrical quantities. Here we define the optimization goal through the minimization of a cost function. The latter can include a wide range of plasma parameters: plasma current, plasma elongation, EC, NBI heating or current drive power, electron density, etc.

An optimization of the ramp-up phase of the plasma discharge with plasma current and EC heating as actuators has already been carried out with the RAPTOR code [Felici et al.(2012)]. In particular, the simulation showed that a plasma current overshoot with early heating allows to get a V_{loop} radial profile close to stationary state and a safety factor profile appropriate for a hybrid scenario operation. In the present work for the ramp-down optimization, we use the same method as in [Felici et al.(2012)].

In Fig. 4.1 a scheme of the optimization procedure is presented. Input trajectories are the parameters for which we need to find an optimal time evolution, so they can also be called optimization parameters. Various plasma actuators (like the plasma current I_p , input powers, geometrical quantities) used by RAPTOR as prescribed parameters can be included to the set of optimization parameters. These parameters are sent to the “Tokamak profile simulator”, it is the RAPTOR code in our case. As a result, the simulator provides the plasma state trajectories. For RAPTOR, solving the diffusion equations Eq. 2.36-2.40, we can obtain the poloidal flux $\psi(\rho, t)$, the electron and ion temperatures $T_{e,i}(\rho, t)$ and densities $n_{e,i}(\rho, t)$ and

Chapter 4. Optimization of the ramp-down phase

calculate various plasma parameters, like the internal inductance $l_i(\rho, t)$ and normalized pressure $\beta_N(\rho, t)$, based on these quantities. Then there is an optimization box, where MATLAB intrinsic optimization algorithms are applied to the proposed plasma state.

Firstly, a specific cost function has to be defined to represent the goal of the optimization. The optimization algorithm minimizes the cost function value to reach a specific plasma state. For the optimization of the ramp-up phase for example, it can be a specific profile for the safety factor q at the end of ramp-up. Thus, the cost function value reflects how close the q profile from RAPTOR is to the reference profile. The constraint function shows if the plasma with provided state trajectories is within the required limits or not. The optimization algorithm calculates cost and constraint functions for the current plasma state and also their derivatives over optimization parameters to define the optimization direction. And as a result it gives updated values for the optimization parameters which will provide the lowest value for the cost function to have plasma within the required constraints. This optimization procedure can be applied for any part of the discharge, in this work we focus on the optimization of the ramp-down phase.

4.2.1 Optimization parameters

First, a set of parameters to be optimized has to be defined. In this work, we focus on three plasma parameters: the plasma current I_p , the plasma boundary elongation κ_b and the time instant of the transition from H- to L-mode t_{HL} .

Typically, in case of a ramp-up optimization, we are interested in reaching a specific plasma state, in particular characterized by the safety factor q profile [Felici et al.(2012), Xu et al.(2013)]. Global and local heat and particle confinement are defined by the plasma state at the beginning of the flat-top phase, thus it is very sensitive to the q profile shape [Challis et al.(2002)]. During the ramp-up phase, the safety factor q profile evolves under the influence of the ramp-up rate of the plasma current and various current drive sources. In contrast to ramp-up, during the ramp-down phase we are not necessarily interested in a specific shape of q -profile. It is more important to avoid rational surfaces at high currents ($q_{95} \approx 3$) to avoid generation of MHD instabilities. The main goal for ramp-down to find an optimal trajectory is to decrease the plasma current. Thus, for the optimization we use the total plasma current I_p but not a profile as an optimization parameter.

As it was mentioned above in Sec. 4.1, growth of the plasma internal inductance can be well controlled with an appropriate plasma shaping. Therefore, geometrical quantities like the elongation κ , the triangularity δ , the minor radius a are essential parameters for the ramp-down optimization. As it was discussed in Sec. 2.2, RAPTOR uses prescribed equilibrium data generated by an external equilibrium-reconstruction code. To test ramp-down trajectories with various plasma shapes, the optimization algorithm has to update these equilibrium data automatically. Thus, we need analytical relations to describe connections between geometrical quantities and the equilibrium parameters required by RAPTOR. Because of strong

nonlinear relations between these parameters, analytical formulas are difficult to develop, and an independent study, similar to the numerical analysis described in [Sauter(2016)], is required but it is out of scope of this work. To simplify the optimization procedure, the plasma boundary elongation κ_b is the only geometrical optimization parameter, whereas the plasma triangularity and the minor radius are assumed to be fixed at the reference values during the optimization. The reference values for the geometrical quantities used in Eqs. 2.36-2.40 are defined according to provided CHEASE equilibrium data. These profiles are scaled proportionally to the plasma boundary elongation κ_b during the optimization of its trajectory. We can verify the optimized trajectory when we recompute the geometrical profiles with CHEASE solution using the optimized elongation and the RAPTOR pressure and current density profiles. Note that a strong reduction in the plasma elongation with fixed plasma triangularity and minor radius are hardly achievable in real experiments. At this stage, the optimization algorithm does not allow variation in these parameters, but it should be included at the next step allowing more realistic prediction of the plasma shape evolution.

A plasma state is rather sensitive to the transition from H- to L-mode, and a time instant of this transition has to be carefully defined, especially for big devices like ITER [Imbeaux et al.(2011), Leonov et al.(2010)]. Therefore, t_{HL} has been chosen as an extra optimization parameter in case of the current ramp-down in H-mode. We define the H- to L-mode transition as a time instant when the input power $P_{in} \leq P_{LH}$ where P_{LH} represents a threshold power for L-H transition, calculated according to the scaling law, presented in Eq. 2.59. This law does not take into account the plasma energy hysteresis during the H-L transition [Hinton(1991)]. In this work, we simulate the H-L transition with the P_{in} drop from $1.1P_{LH}$ to $0.9P_{LH}$. The time evolution of plasma profiles from H- to L-modes is described on time scales used for TCv, AUG and JET simulations described in Chapter 3. Prescribed power trajectories are updated with t_{HL} during the optimization in the way to have the input power higher than P_{LH} before the transition and lower than P_{LH} after it.

In the optimization algorithm, the input vector of the time-dependent actuator trajectories $[I_p(t), \kappa_b(t), t_{HL}]$ is parametrized by a vector containing a discrete set of scalar parameters. The trajectory $u_i(t)$ for the i th actuator is written as

$$u_i(t) = \sum_j^{n_i} P_{ij}(t) p_{i,j} \quad (4.2)$$

where $P_{ij}(t)$ is a scalar function of time (piecewise linear or piecewise constant function with a finite support and maximum $P_{ij}(t) = 1$), the scalar $p_{i,j}$ gives the weight of the associated function, n_i is the number of parameters which define the i th actuator trajectory. For example, we need to find an optimal trajectory for the $I_p(t)$ 2 s ramp-down from its flattop value (≈ 1 MA) to much lower value (≈ 100 kA). The ramp down phase is discretized in time by n_{I_p} points and defined time instants t_{knot} . The vector p_{I_p} contains n_{I_p} elements which correspond to I_p values at time instants t_{knot} . The optimization algorithm starts from p_{I_p} with I_p reference values. Using $P_{ij}(t)$, the time-dependent trajectory $I_p(t)$ is constructed from p_{I_p} . More details

Chapter 4. Optimization of the ramp-down phase

can be found in [Felici et al.(2012)].

4.2.2 The cost function

Depending on a problem, different cost functions can be used. Here it is defined as a sum of the time integrals of the total plasma current I_p , the total input power P_{tot} and the boundary elongation κ with weights ν_{I_p} , $\nu_{P_{tot}}$, ν_{κ_b} :

$$J = \nu_{I_p} \frac{\int_{t_{RD}}^{t_{end}} I_p(t) dt}{\int_{t_{RD}}^{t_{end}} I_p^{ref}(t) dt} + \nu_{P_{tot}} \frac{\int_{t_{RD}}^{t_{end}} P_{tot}(t) dt}{\int_{t_{RD}}^{t_{end}} P_{tot}^{ref}(t) dt} + \nu_{\kappa_b} \frac{\int_{t_{RD}}^{t_{end}} \kappa_b(t) dt}{\int_{t_{RD}}^{t_{end}} \kappa_b^{ref}(t) dt} \quad (4.3)$$

Here the optimization parameters have different scales. A typical scale for I_p and P_{tot} is 10^6 , whereas for κ_b it is 10^0 . Therefore terms in Eq. 4.3 are normalized with their corresponding reference values, and $J = 1$ at the first iteration of the optimization algorithm when choosing ν_{I_p} , $\nu_{P_{tot}}$ and ν_{κ_b} such that their sum is 1.

In this particular task, we integrate over the ramp-down phase, i.e. from the start of the I_p ramp-down t_{RD} to the end of a plasma shot t_{end} . The optimization goal is to decrease the plasma current and/or input power and/or the plasma elongation as fast as possible to reduce the amount of energy stored in the plasma and forces, related to I_p and the shape, in order to reduce the risks related to a disruption during the ramp-down phase [Sugihara et al.(2007), Lehnen et al.(2013)]. Variation in the weights ν_{I_p} , $\nu_{P_{tot}}$, ν_{κ_b} can change the search direction of the optimal solution and, thus, lead to different optimized trajectories.

Other options can be easily added to the cost function. For the ramp-down optimization, the terms like a time integral of the plasma thermal energy or I_p^2 or the magnetic field B_0 can be tested. The latter will be important for tokamaks working with variation in the magnetic field B_0 during a plasma discharge.

4.2.3 The constraint function and other optimization limits

As it was mentioned in Sec. 4.1, there are plenty of physical and technical issues important for a safe termination. At this stage, it is not possible to take all of them into account in the present optimization. We have to define a set of the most crucial parameters which RAPTOR can predict. The constraints used in this work can be divided into physical and technical ones:

Physical constraints:

- The line-averaged electron density n_{el} lower than 90% of $n_{GR} = I_p(t)/\pi a^2$ (Greenwald density limit [Greenwald(2002)]).

The Greenwald density limit n_{GR} depends on the optimization parameter I_p , therefore it is updated at each iteration within the cycle presented in Fig. 4.1. The electron

density $n_e(\rho, t)$ has to be updated with the line-averaged density n_{el} to keep it within the required level $0.9n_{GR}$. There are two options to take this constraint into account. If RAPTOR, i.e. the ‘‘Tokamak profile simulator’’ block in Fig. 4.1, solves diffusion equations for the poloidal flux ψ and the electron temperature T_e and uses a prescribed electron density $n_e(\rho, t)$, then these prescribed profiles are scaled proportionally to n_{el} . If the electron density is a predicted parameter, the transport coefficients for electrons, described in Subsec. 2.6.2, are constructed using the updated n_{el} as a reference.

- The safety factor q_{95} greater than q_{95} at the beginning of the ramp-down phase to ensure that the plasma shape (elongation) does not change faster than the plasma current I_p .
- The normalized pressure β_N below a certain limit (MHD limit).
- Any other constraints based on the physical quantities simulated by RAPTOR can be added.

Technical constraints:

- The ramp-down rate of the plasma current dI_p/dt .

RAPTOR is not a full tokamak plasma solver, like DINA [Khayrutdinov and Lukash(1993), Favez et al.(2002)], therefore we do not consider currents in the external coils which define the capability of a machine to control plasmas. Here we define a constraint on dI_p/dt , i.e. a complex parameter reflecting collective limitations on the machine coils system. Thus, typical dI_p/dt values for a machine can be estimated from experimental databases. Also dI_p/dt maximum can be computed from the characteristics of the coil systems and passive conductors.

- The ramp-down rate of the plasma boundary elongation $d\kappa_b/dt$.

The plasma shape control is limited by poloidal coils installed on a machine. Again as for I_p , here we set a constraint on the rate of change in the plasma boundary elongation κ_b to represent constraints on the shaping coils.

- Limit plasma internal inductance $l_i(3)$ for vertical position control;

One could compute the ideal growth rate [Hofmann et al.(1997)] and limit its maximum value. This can also be done as a part of the post-shot analysis of the experimental data.

- Limit the maximum rate of change of the vertical magnetic field dB_v/dt for radial position control;
- Other technical constraints specific for a machine.

Further extension of the constraints set can be continued with the help of collected disruption statistics on the existing machines, in particular for JET [De Vries et al.(2014)] and AUG [Pautasso et al.(2007)].

Chapter 4. Optimization of the ramp-down phase

Here upper and lower boundaries for the elements of the vector p (Eq. (4.2)) as well as limits on ramp rates for I_p and κ are specified through linear inequality constraints:

$$A_{ineq}p \leq b_{ineq} \quad (4.4)$$

A constraint on the highest/lowest value of any other parameter ($\beta_N(t)$, $l_i(3)(\rho, t)$, etc) can be specified in the same way as it has been described in [Felici et al.(2012)], where integral constraints are formulated [Teo et al.(1991)]. In this case the i th state a constraint of the form $c_i(t, x(t)) \leq 0$, where x denotes an optimization parameter, is rewritten as

$$C_i = \left(\int_{t_f}^{t_i} (\max[0, c_i(t, x(t))])^2 dt - \epsilon \right) \leq 0 \quad (4.5)$$

where a relaxation $\epsilon \approx 10^{-6}$ is defined to ensure that $\frac{\partial C_i}{\partial x} \neq 0$, which is a required property for a well-posed optimization problem [Nocedal and Wright(2006)].

4.2.4 Summary for the optimization algorithm

Just as in [Felici et al.(2012)], we use the MATLAB function called `fmincon`, based on the method of Sequential Quadratic Programming (SQP) [Nocedal and Wright(2006)], to solve the nonlinear constrained optimization problem.

To define the search direction of the optimal solution, the SQP algorithm requires an estimate of the local gradient of the cost and constraint functions over a current plasma state. In the presented algorithm, the MATLAB optimization solver uses numerical gradients calculated by finite differences. This is the main difference with the method used in [Felici et al.(2012)], where the analytical gradients of the cost function have been calculated for this purpose. The reason is in the difficulty of an analytical description of the plasma state gradients in terms of plasma geometry and confinement state. In [Felici et al.(2012)] the plasma actuators, like the plasma current $I_p(t)$ and input powers $P_{in}(t)$, have been used as optimization parameters. Derivatives of the plasma state profiles $\psi(\rho, t)$ and $T_e(\rho, t)$ on $I_p(t)$ and $P_{in}(t)$ can be derived analytically, thus one could obtain these gradients as a by-product of the implicit time-solver of the PDE. However here, we require gradients with respect to geometric terms such as $g_2(\rho, t)$, $g_3(\rho, t)$ etc. (described in Appendix A), which are not calculated by the PDE solver. Thus the gradients are calculated with the help of the MATLAB optimization toolbox. The main disadvantage of finite differences usage is an increase of the CPU time required for an optimal solution search. Nevertheless the optimization procedure still can be finished within a reasonable amount of time (couple of hours) thanks to the high speed of the RAPTOR solver.

Note that in general there is a finite probability that the solution found by the SQP algorithm is a local optimum but not a global one. A proper choice of initial conditions, optimization parameters and constraints may help to avoid his problem. Also other optimization algorithms, constructed specifically with a low risk of missing a global optimum (like a genetic

algorithm [Goldberg(1989)], can be tried but generally they are more time-consuming. In our particular case, an optimization of the ramp-down phase is complicated by a huge set of various constraints of plasma parameters which strongly limits a searching area of the optimal solution. Therefore any improvement in the reference trajectories obtained with the help of the optimization algorithm is very useful for a plasma ramp-down scenario development.

4.2.5 Simple 2D optimization

In order to illustrate the optimization problem, a simple example with two optimization parameters is presented: an optimization of the plasma current I_p and the boundary elongation κ_b at one time instant. In Fig. 4.2 a ramp-down optimization for an AUG-like plasma is demonstrated. Plasma parameters I_p and κ_b are fixed at $t = 0$ s and $t = 1.5$ s and optimized at $t = 0.5$ s. The cost function J_{I_p} is a time integral of the plasma current I_p , i.e weights in Eq. 4.3 are defined as follows: $v_{I_p} = 1$, $v_{P_{tot}} = 0$ and $v_{\kappa_b} = 0$. Constraints are imposed on the ramp-down rate of the plasma current ($dI_p/dt \geq -1.9$ [MA/s]), normalized beta ($\beta_N \leq 2.7$) and the plasma internal inductance ($l_i(3) \leq 1.2$). Maximum and minimum values for the optimization parameters are fixed at 0.1/1.0 MA for I_p and 1.0/1.9 for κ_b . The reference trajectories of the plasma current I_p and boundary elongation κ to be optimized and for other parameters are marked in black in Fig. 4.2. The black dot on the first contour plot corresponds to reference values of I_p and κ_b at $t = 0.5$ s, i.e. an initial state of the input vector of optimization parameters $p = [I_p(t = 0.5) \ \kappa_b(t = 0.5)] = [1.0 \ 1.8]$.

In case of unconstrained optimization, I_p and κ_b take the lowest allowed values at $t = 0.5$ s (dark yellow line/dot in Fig. 4.2), thus the cost function is minimized. To keep I_p lower than reference while adding the constraint on β_N (blue line/dot), the plasma elongation has to be increased in comparison to the reference case. The yellow area in the third contour plot corresponds to I_p and κ_b values at $t = 0.5$ s which full trajectories lead to β_N higher than 2.8. The optimization with additional constraint on $l_i(3)$ significantly reduces an area of I_p and κ_b available values. In case of optimization with constraints on β_N and $l_i(3)$ a fast current ramp-down can be reached with faster decrease in the plasma elongation κ_b (red line). As it can be seen from the last contour plot, the constraint on the internal plasma inductance is the most stringent one. We have a very limited set of $[I_p(t = 0.5), \kappa_b(t = 0.5)]$ to have l_i within the required limit, since its behavior strongly depends on the combination of $I_p(t = 0.5)$ and $\kappa_b(t = 0.5)$.

Here, we present the optimization of two parameters $[I_p(t = 0.5), \kappa_b(t = 0.5)]$ as a simple example, whereas a set of optimization points has to be used to obtain an optimal trajectory which leads to a true minimum of the cost function within the required constraints.

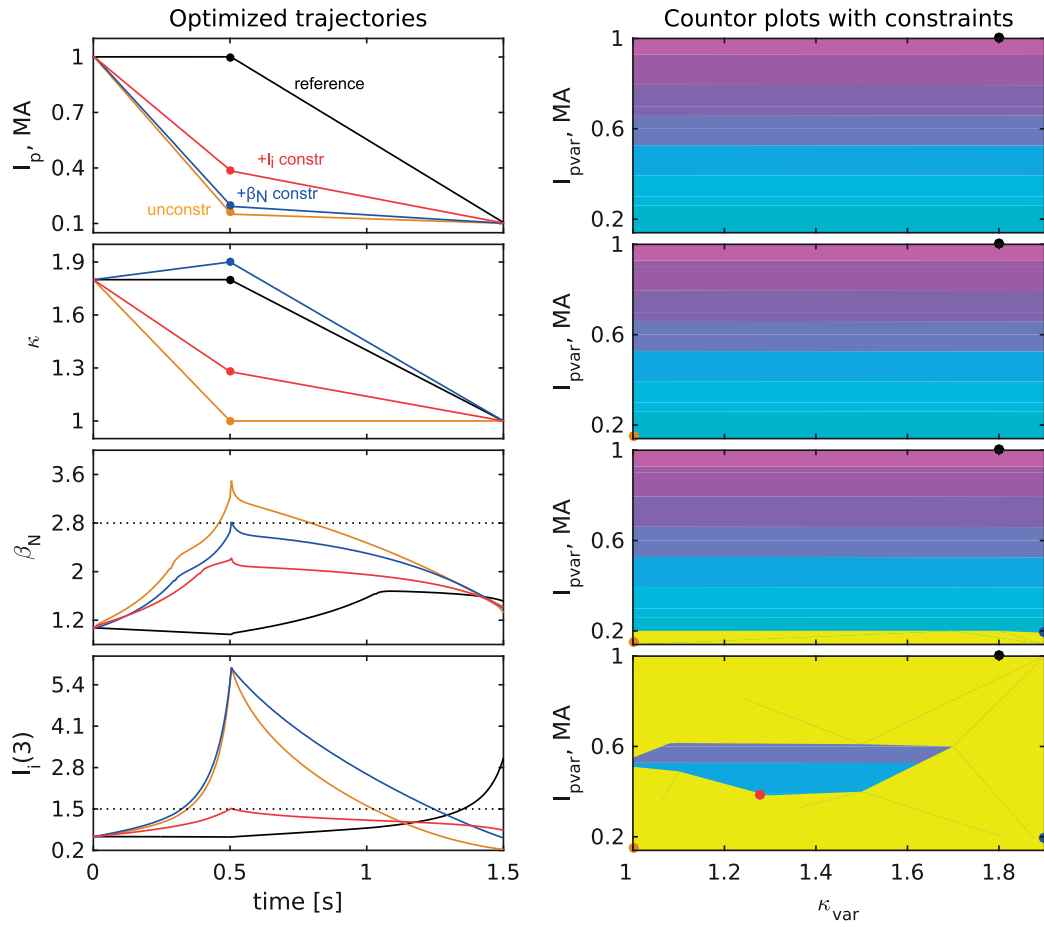


Figure 4.2: A simple ramp-down optimization for AUG-like plasma. Time evolution of the plasma current I_p , the plasma boundary elongation κ_b , normalized beta β_N and the plasma internal inductance $l_i(3)$ are demonstrated for the reference case (black), unconstrained optimization (dark yellow), optimization with the constraint on β_N (blue), on β_N and $l_i(3)$ (red). The contours for the cost function J_{I_p} are shown with the colored circles corresponding to I_p and κ_b values at $t = 0.5$ s. J_{I_p} increases with the plasma current. An area where a constrained parameter violates the constraint is yellow-marked.

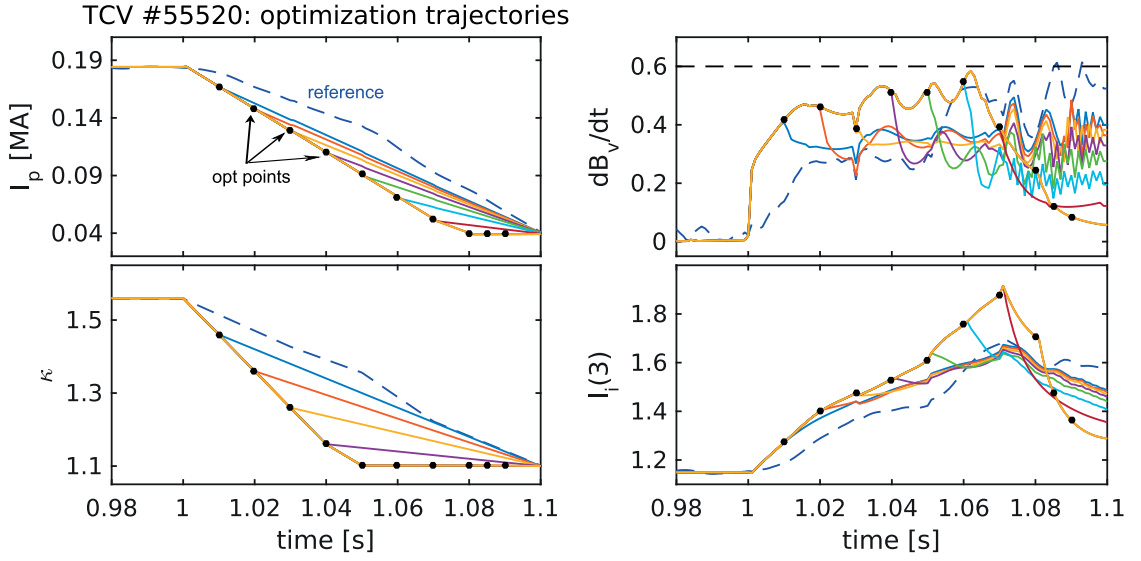


Figure 4.3: Ramp-down optimization for the TCV shot #55520. Time traces for plasma current I_p , plasma boundary elongation κ , rate of change in vertical magnetic field dB_v/dt and plasma internal inductance $l_i(3)$ are presented for the reference case (blue dashed) and various optimized trajectories (colorful solid) with the optimization points (black dots) on the optimal trajectory.

4.3 Ramp-down optimization for TCV

We start with an optimization of the ramp-down phase of TCV plasmas. On TCV we are limited in the radial position control. Therefore for the optimization of a TCV plasma, a constraint on the rate of change in the vertical magnetic field dB_v/dt is the main technical constraint in addition to constraints on the ramp-down rates of the plasma current dI_p/dt and the plasma boundary elongation $d\kappa_b/dt$. The exact values of the technical limits have been obtained after analyzing several TCV termination trajectories and have been set in the following way: $dB_v/dt \leq 0.6$ [T/s], $dI_p/dt \geq -1.9$ [MA/s] and $d\kappa_b/dt \geq -10$ s^{-1} .

4.3.1 Numerical optimization

Reference trajectories for the ramp-down phase have been obtained with the RAPTOR simulation of the TCV shot #55520, discussed in Subsec. 3.2.1, and are demonstrated for the plasma current I_p , the boundary elongation κ_b , the rate of change in the magnetic field dB_v/dt and the internal inductance l_i in Fig. 4.3 in dashed blue line. For RAPTOR simulation the poloidal flux ψ and the electron temperature T_e have been predicted, whereas the electron density n_e is a prescribed parameter and ions profiles are scaled from electrons. It is an ohmic L-mode shot, therefore the transport parameters λ_{T_e} and H_e are fixed at the L-mode values, 3.2 and 0.35 correspondingly. The optimization parameters are the plasma current I_p and the boundary elongation κ_b . The cost function is defined according to Eq. 4.3 with $v_{I_p} = 1$, $v_{P_{tot}} = 0$ and

Chapter 4. Optimization of the ramp-down phase

$v_{\kappa_b} = 0$. The physical constraint is imposed on the safety factor $q_{95} \geq 3.3$ (minimum value for the reference case). We do not consider constraints on the electron density, since in the L-mode plasma the line-averaged density is far from the Greenwald density limit. Shot #55520 has been terminated down to $I_p = 40$ kA and $\kappa_b = 1.1$, thus the final point for I_p and κ_b trajectories is fixed at the reference values which also define minimal allowed values for I_p and κ_b .

Plasma current and elongation trajectories have been optimized in series of 10 points: starting from the reference trajectories, I_p and κ have been optimized first at $t = 1.01$ s, then starting from the last optimized trajectory I_p and κ_b have been optimized at $t = [1.01, 1.02]$ s and so on up to the final set of 10 optimization points. The reference and optimized (with number of optimization points varied from 1 to 10) trajectories of I_p , κ_b , dB_v/dt and $l_i(3)$ are shown in Fig. 4.3. This optimization shows that faster ramp-down in I_p can be performed while keeping dB_v/dt at the safe level with proper plasma shaping forced by a faster than reference decrease in κ_b . A faster growth in the internal inductance l_i is generated with the optimized trajectory but TCV plasmas can be stable for much higher l_i .

Note that increasing the number of optimization points will not decrease the cost function anymore and the set of 5 optimization points $t = [1.01, 1.04, 1.05, 1.07, 1.08]$ s is sufficient to get the same optimized trajectory. To avoid possible local minima, we have checked that the optimized trajectory is the same if the sequence of optimization points is taken in a different order.

4.3.2 An experimental test

A next step for validation of the optimization procedure is a test of the optimized trajectories on a machine. The optimized trajectories from Subsec. 4.3.1 have been tested on TCV in the shot #55672. The waveforms for the plasma current I_p and the plasma boundary elongation κ_b have been programmed according to these trajectories. To compare the optimized trajectories, we simulate the TCV shot #55672 with the same transport model for the RAPTOR code.

In Fig. 4.4 optimized trajectories for the TCV shot #55520 (dashed blue - reference, solid red - optimized trajectories) and RAPTOR simulations for the TCV shot #55672 (black dashed) are presented. For the internal inductance l_i and the boundary elongation κ_b LIUQE experimental time traces (blue circles) are plotted too. In #55672 a non-disruptive termination has been obtained with a faster ramp-down in I_p and a slightly slower decrease in κ than requested. The difference in the optimized and experimentally obtained plasma elongation can be a consequence of the assumption of fixed triangularity and minor radius in the optimization algorithm, since in the experiment these parameters have been slightly reduced with the decrease of the plasma elongation. Note that the predicted (from the optimization) and the simulated time evolution of l_i and dB_v/dt are very similar. Moreover LIUQE output for l_i is very close to RAPTOR simulations. The constraint parameter dB_v/dt , obtained in the experiment, stays mostly within the required limit with a few sawtooth crashes violating it.

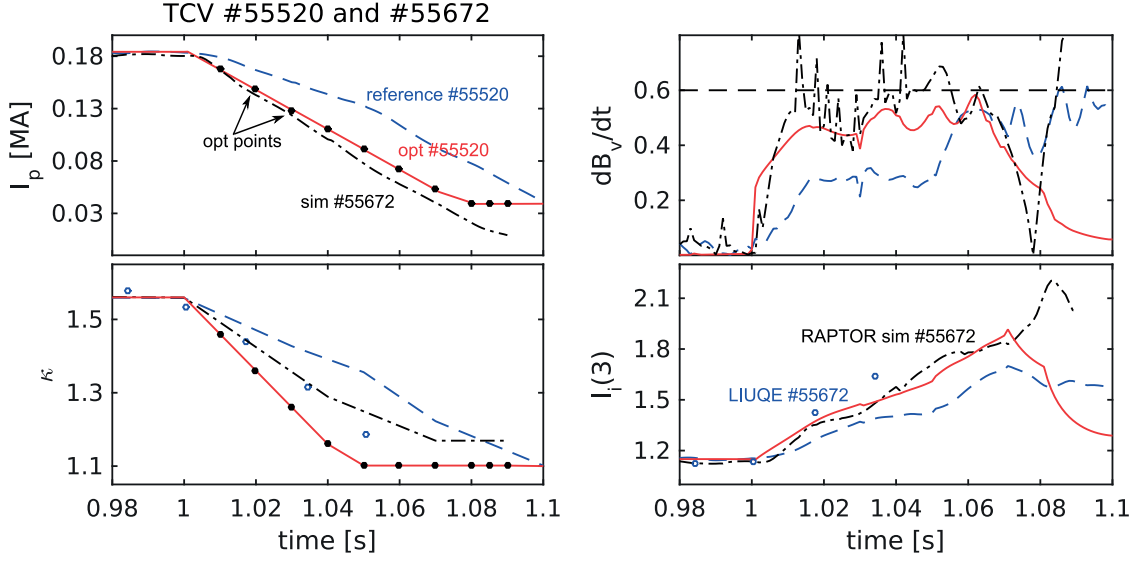


Figure 4.4: Time traces of I_p , κ_b , $I_i(3)$ and $T_e(\rho = 0.1)$ for the reference (dashed blue) and optimized TCV shot #55520 (solid red), from the experimental data base for the TCV shot #55672 (blue circles) and RAPTOR simulation of #55672 (dot-dashed black).

We can conclude that a fast ramp-down of both I_p and κ_b has been successfully tested on the TCV tokamak for L-mode plasmas, following the presented simulations with the RAPTOR code. Further experimental tests are required to check capabilities of the shaping control system.

4.4 Ramp-down optimization for ASDEX Upgrade

Here we discuss an optimization of the ramp-down phase for the ASDEX Upgrade tokamak. After analyzing of several ramp-down trajectories for AUG plasmas, the maximum plasma current ramp-down rate is set to 0.7 [MA/s]. However according to more systematic analysis of the ramp-down phase presented in [Pau et al.(2017)], a bit faster I_p ramp-down with $\max(dI_p/dt) = 0.8$ [MA/s] can be accepted by the control system.

4.4.1 Numerical optimization

As a reference for the optimization procedure, we consider the ramp-down phase of the AUG shot #33589. RAPTOR simulation with predicted ψ and T_e and prescribed n_e provides reference trajectories for various physical quantities presented in Fig. 4.5 (blue dot-dashed). The transport parameters λ_{T_e} and H_e are fixed at typical H-/L-mode values for AUG, 2.3/3.0 and 0.2/0.4 correspondingly. For the numerical optimization, the additional physical constraints have been imposed on the internal plasma inductance $I_i(3) \leq 1.4$ (maximum value for the reference case), normalized beta $\beta_N \leq 1.1$ (maximum value for the reference case), safety factor $q_{95} \geq 4.4$ (minimum value for the reference case) and on the line-averaged electron

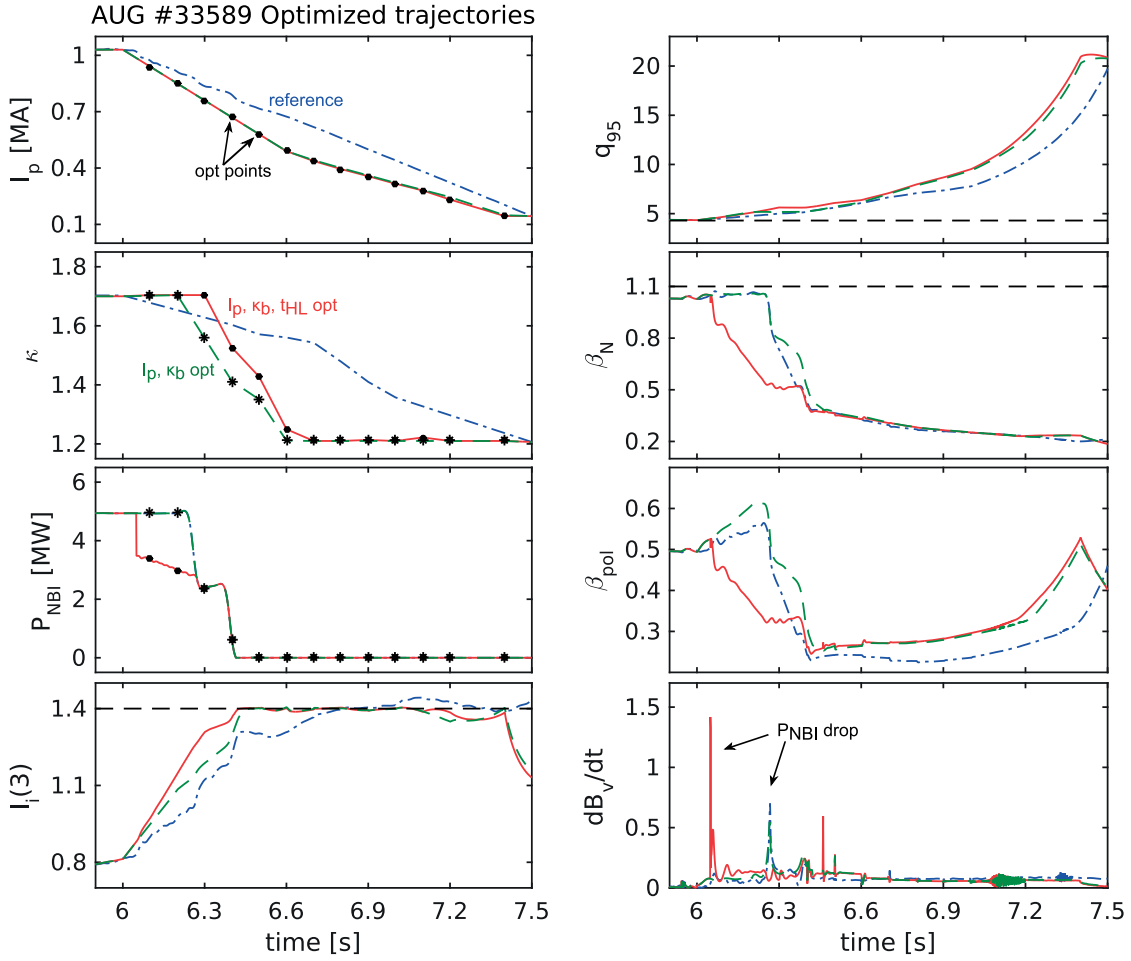


Figure 4.5: Ramp-down optimization for the AUG shot #33589. There are presented the reference trajectories (blue dot-dashed), results of the optimization of I_p and κ_b only (green dashed) and with t_{HL} as an additional optimization parameter (red solid). Time traces for the following parameters are shown: the plasma current I_p , the boundary elongation κ_b , NBI power P_{NBI} , plasma internal inductance $l_i(3)$ and 1.4 limit, the safety factor q_{95} and 4.4 limit, normalized beta β_N and 1.1 limit, poloidal beta β_{pol} , the rate of change in the vertical magnetic field dB_v/dt . Optimization points are marked by the black dots (optimization of I_p and κ_b) and asterisks (optimization of I_p , κ_b and t_{HL}).

density n_{el} to keep it within the Greenwald density limit.

I_p and κ_b optimization

First, the plasma current I_p and the plasma boundary elongation κ have been optimized with 13 points with $v_{I_p} = 1$ and $v_{P_{tot}} = v_{\kappa_b} = 0$ for the cost function defined in Eq. 4.3 (dashed green lines on Fig. 4.5). The input power and time instant of the H-L transition is kept as in the reference. The optimal solution shows that with a proper reduction of the plasma elongation κ_b , the plasma current I_p ramp-down can be performed faster than the reference while keeping the internal plasma inductance l_i at a safe level and other parameters within the required limits.

I_p, κ_b and t_{HL} optimization

Then the instant of the H- to L-mode transition t_{HL} has been added to the set of the optimization parameters. In this optimization example, the cost function is defined as Eq. 4.3 with $v_{I_p} = 0.5$, $v_{\kappa_b} = 0$ and $v_{P_{tot}} = 0.5$, i.e. the goal of the optimization is to minimize both the plasma current and the input power. Since the prescribed input power does not include the ohmic power, which is calculated by RAPTOR itself, P_{tot} is equal to the input NBI power. To simulate the transition from H- to L-mode, P_{tot} is updated at each iteration of the optimization loop to have it higher than the threshold P_{LH} before t_{HL} and lower after t_{HL} . For this optimization at t_{HL} , P_{NBI} power level drops to $P_{LH}(t_{HL})$ and linearly decreases to $0.9P_{LH}$ assuming that there might be 10% fraction from the ohmic power.

The reference t_{HL} is 6.26 s, the optimized value is 6.05 s. Slightly different time evolution of κ_b and an early drop of the input power give the same time evolution for the plasma current (which is limited by the allowed ramp-down rate) and keep the plasma inductance l_i within the required limit. Also, the early H-L transition case yields a smaller drop in poloidal beta β_{pol} than in the reference case, which can be important for MHD stability and the radial position control. It also helps to decrease the density faster and to avoid density limit while decreasing I_p . The set of the optimization points can be limited by the first 7 points (from 6.1 s to 6.7 s) and the last one (7.4 s) to get the same optimized trajectories for I_p , κ_b and t_{HL} .

There is no limit on the rate of change in vertical magnetic field dB_v/dt and as can be seen from Fig. 4.5, an earlier drop in NBI power produces higher peaking of dB_v/dt . Further analysis of experimental data and the machine characteristics is required for understanding and specifying a relevant limit for dB_v/dt (i.e. if there are disruptions caused by loss of radial position control for AUG simulations). In particular, limit on the rate of change in the plasmas shape, i.e. $d\kappa/dt$ in our case, has to be defined from the experimental database.

4.4.2 Experimental tests

The Discharge Control System (DCS) for the ASDEX Upgrade tokamak, based on feedback control algorithms, processes raw signals from plasma diagnostics to reconstruct various

Chapter 4. Optimization of the ramp-down phase

plasma quantities like the plasma geometry and fluxes distribution in space and time, plasma kinetic profiles and heat fluxes, etc. [Treutterer et al.(2014)]. DCS command outputs are confined by strict limits preventing damages of the machine. For example, currents in the AUG divertor coils $OH2u$ and $OH2o$ have upper and lower limits which are defined by coils suppression forces. Specific limits can be related to changes in the plasma energy, heating and other dynamic plasma characteristics.

AUG standard ramp-down segment

For the plasma ramp-down, a programmed soft-landing procedure has been developed [Treutterer et al.(2014)]. During this procedure, the plasma current is decreased with the plasma shape slowly changing from diverted (and high elongated) to a circular one and a staged shutdown of the additional heating. However, there is a common problem with plasma disruptions in H-modes. In Fig. 4.6 several ramp-down trajectories are demonstrated. It can be seen that plasmas in H-mode stay highly elongated much longer than plasmas in L-mode and disrupts much earlier. Therefore, for the improvement of the AUG ramp-down standard procedure, the optimized ramp-down trajectories, developed as part of this thesis, have been started to be tested on the machine.

Experimental tests of the optimized trajectories

In Fig. 4.7, results of experimental tests with programmed ramp-down are demonstrated. The AUG shot #34450 has a standard ramp-down (the DCS segment programmed for “soft-landing”). Shots #34449, #34489, #34490 have programmed I_p , κ_b and powers different than in the standard ramp-down. Shots #34450 and #34449 have termination in L-mode, whereas #34489 and #34490 have stayed in H-mode during the ramp-down phase until the disruption.

As it is shown in Fig. 4.7, shots #34450 (blue) and #34449 (red) have similar I_p ramp-down rates. However, the second one has a faster decrease in the plasma elongation leading to a slower increase in the plasma internal inductance l_i . Also some compensation in the l_i growth might come from NBI heating which starts at 0.07 s. Shots #34489 (green) and #34490 (yellow) have different ramp-down rates in I_p , but l_i and κ_b trajectories are very similar. With lower NBI heating (4 MW instead of 6 MW) a faster I_p ramp-down with same l_i is possible.

However, because of the technical machine requirements, it was not possible to run experiments with programmed trajectories with the ramp-down phase longer than $0.5 \div 0.7$ s. Currents in the coils the $OH2u$ and $OH2o$ have reached their limits at 0.5 s for #34449 and at 0.7 s for #34489/#34490. After that DCS has switched automatically to the standard ramp-down procedure. Nevertheless, from these tests we can see a positive effect on the l_i evolution coming from the proper decrease in the plasma elongation and heating power. Note that all our programmed ramp-down cases so far have been limited only by these coils limit due to the way the shape is controlled during the ramp-down. A better programmed shape evolution, to be design using the predicted plasma parameters evolution during the ramp-down phase, would allow to avoid these problems and test further the termination strategies.

4.4. Ramp-down optimization for ASDEX Upgrade

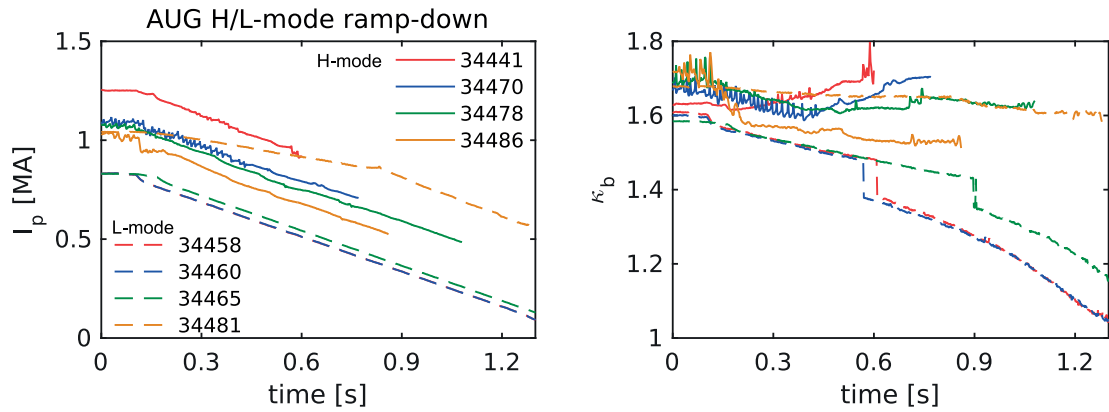


Figure 4.6: AUG ramp-down trajectories for plasmas in L- (dashed) and H-mode (solid) at the end of flat-top. Experimental signals are provided by the CLISTE code.

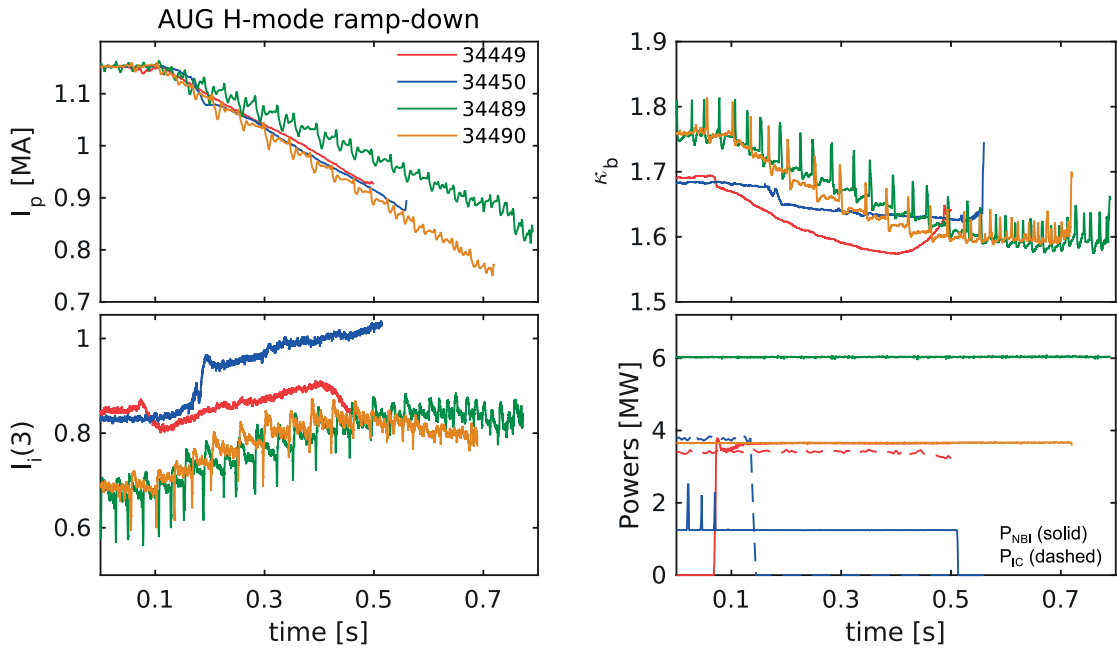


Figure 4.7: Ramp-down trajectories for the plasma current I_p , the boundary elongation κ_b , the plasma internal inductance l_i and auxiliary heating powers, P_{NBI} (solid) and P_{IC} (dashed) for AUG shots; #34450 (standard ramp-down) and #34449, #34489, #34490 (programmed ramp-down). Experimental signals are provided by the CLISTE code.

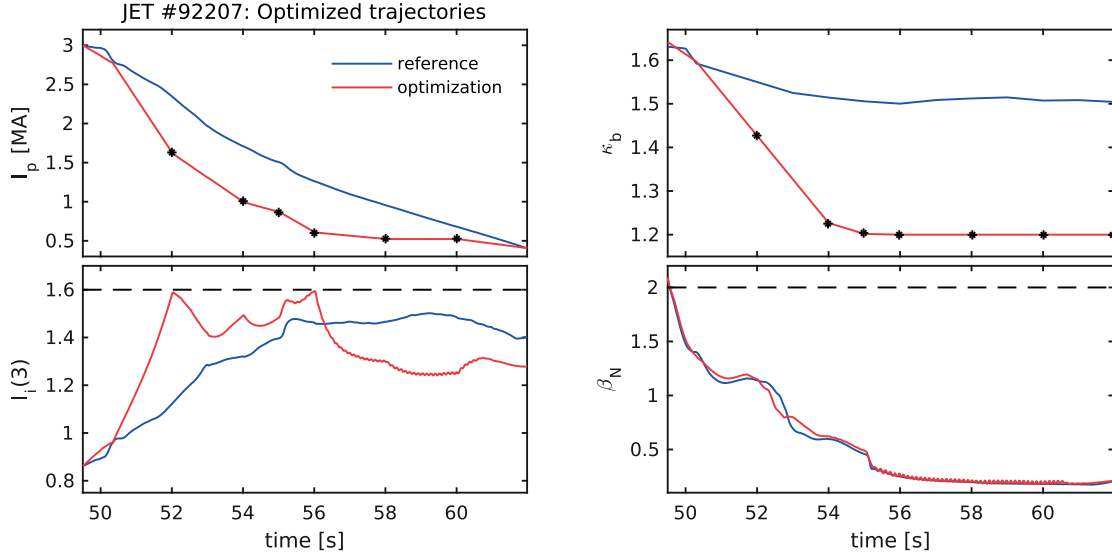


Figure 4.8: Ramp-down optimization for the JET shot #92207. The reference trajectories are in the blue color, the optimized trajectories are in red. Results of the optimization of I_p and κ_b at optimization points (black dots) $t_{knot} = [52, 54, 55, 56, 58, 60]$ s (and 62 s for κ_b only) are shown. Time traces for the following parameters are presented: the plasma current I_p , the boundary elongation κ_b , plasma internal inductance $l_i(3)$ and 1.6 limit, normalized beta β_N and 2.0 limit.

4.5 Ramp-down optimization for JET

In order to continue testing the optimization algorithm, an optimization of the JET #92207 ramp-down phase has been performed. This shot has early H-L transition (at 52 s), therefore here we do not consider t_{HL} as an optimization parameter. This ramp-down phase has almost constant plasma elongation κ_b , and it is interesting to see an influence of the κ_b decrease on the plasma state evolution. The cost function is defined according to Eq. 4.3 with $v_{I_p} = 0.9$, $v_{P_{tot}} = 0$, $v_{\kappa_b} = 0.1$. We set technical constraints on maximum ramp-down rates in I_p and κ_b similar to [Nunes et al.(2011)]: $dI_p/dt \geq -0.7$ [MA/s] and $d\kappa_b/dt \geq -0.1$ s^{-1} . Additional constraints are imposed on the plasma internal inductance $l_i \leq 1.6$ (close to maximum l_i values reached in JET ramp-downs in [Nunes et al.(2011)]) and $\beta_N \leq 2.0$ (maximum reached at the end of the flat-top phase). Optimization points are fixed at $t_{knot} = [52, 54, 55, 56, 58, 60]$ s. Since we need to allow the optimization algorithm to reduce κ_b , the final point in the ramp-down trajectory at 62 s is also an optimization point for κ_b , but $I_p(t = 62$ s) is fixed at the reference value. The low limit for κ_b equals to 1.2.

With the optimization results presented in Fig. 4.8, we can conclude that reducing κ_b allows to have a faster ramp-down in I_p with similar l_i and β_N evolution. However, for further JET ramp-down optimizations, we need to include more parameters and specify the set of constraints more precisely. The heating scenario during the ramp-down phase can change the

evolution of the internal inductance, for example additional NBI heating will slow down an increase in l_i [Nunes et al.(2011)]. The low limit in κ_b , considered here, might be rather low for JET plasmas, forcing it to the limiter state. Further analysis of the experimental trajectories with the help of the disruption databases [De Vries et al.(2014), Pau et al.(2017)] will help to improve the optimization task. It should be mentioned that even if JET plasmas are not limited by VDEs related to high l_i values, keeping a small l_i evolution during the ramp-down allows to stay further away from ideal limits, which is in general favorable. In addition, reducing the plasma shaping (the plasma elongation κ and triangularity δ), will rapidly reduce the forces in case of disruption during the termination phase.

4.6 Ramp-down trajectories sensitivity

4.6.1 Trajectories sensitivity to transport parameters

TCV and AUG demonstration cases in Subsec. 4.3.1 and 4.4.1 show that there is a room for optimizing plasma ramp-down scenarios and that the dynamic dependencies make it difficult to “guess” the best trajectory. Note that if a specific safe (q_{95}, l_i) domain should be prescribed, it can easily be added to the constraints. On the other hand, optimizing the trajectories as proposed here allow to easily get the correct balance between I_p reduction, κ_b reduction and H-L transition to control l_i , dB_v/dt and β_{pol} . For example the first part can be understood since decreasing I_p at the same rate as the plasma surface will tend to keep the q profile self-similar, hence will not increase l_i significantly. Of course, the resulting optimized trajectory can be tested in more complex codes like DINA-CRONOS. In this way an overall accurate optimization can be obtained faster.

Another important issue requiring a careful study is related to the sensitivity of the optimized trajectories to the transport model parameters. In particular, increased core gradient λ_{T_e} and/or H_e factor lead to higher internal inductance l_i because the electron temperature profile and, as a consequence, the current density profile becomes more peaked. If l_i is used as a constraint for the I_p optimization then the plasma current I_p optimized with higher λ_{T_e} will decrease slower to keep l_i within the required limit. For the sensitivity test, a set of optimizations on the plasma current I_p and the plasma boundary elongation κ for the AUG shot #33589 with varied transport model parameters has been performed (Fig. 4.9). To compare with the reference transport model used in Sec. 4.4 with $\lambda_{T_e} = 2.3/3.0$ and $H_e = 0.2/0.4$ for the H- and L-modes respectively, we vary λ_{T_e} and H_e by $\pm 20\%$. To analyze the influence on the plasma elongation κ_b in a meaningful way it has also been included into the cost function with 0.2 weight, i.e. according to Eq. 4.3:

$$J = 0.8 \frac{\int_{t_{RD}}^{t_{end}} I_p(t) dt}{\int_{t_{RD}}^{t_{end}} I_p^{ref}(t) dt} + 0.2 \frac{\int_{t_{RD}}^{t_{end}} \kappa_b(t) dt}{\int_{t_{RD}}^{t_{end}} \kappa_b^{ref}(t) dt} \quad (4.6)$$

The optimization points are defined on the interval from 6.1 to 7.4 with 0.1 s step, i.e. 14

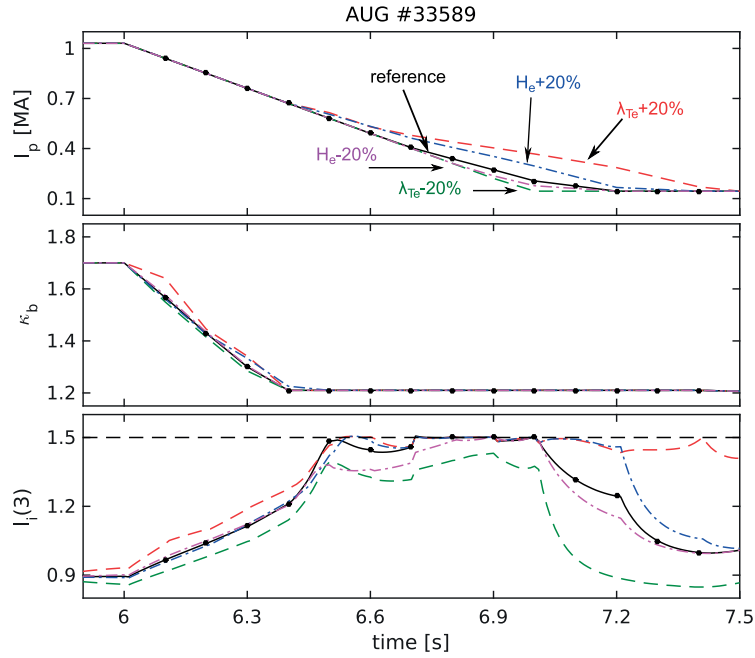


Figure 4.9: Test of the sensitivity of the I_p and κ optimized trajectories to the transport model parameters λ_{Te} and H_e . The optimized trajectories are obtained with the reference transport model (black solid) from Sec. 4.4, $\lambda_{Te} + 20\%$ (red dashed), $\lambda_{Te} - 20\%$ (green dashed), $H_e + 20\%$ (blue dot-dashed) and $H_e - 20\%$ (magenta dot-dashed). The optimization points are marked by the black dots.

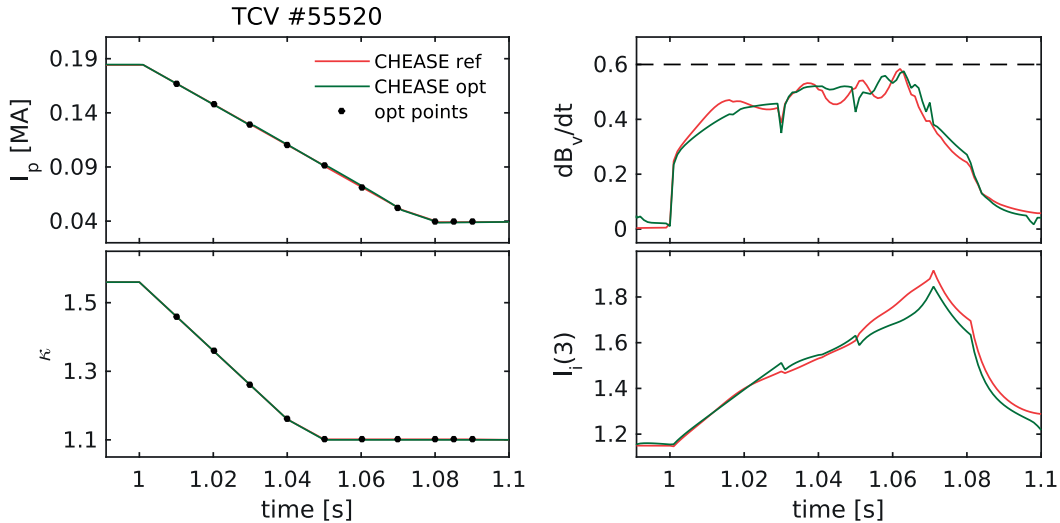


Figure 4.10: Testing the sensitivity of the optimized trajectories on CHEASE equilibria. Optimized trajectories obtained with reference (red) and CHEASE equilibria reconstructed with RAPTOR plasma profiles (green) are demonstrated for the plasma current I_p , the boundary elongation κ_b , dB_v/dt and the internal inductance l_i .

points in total. Only two constraints are defined for this test: $dI_p/dt \geq -0.9$ [MA/s] and $l_i(3) \leq 1.5$. As it can be seen from Fig. 4.9, increased transport parameters λ_{T_e} and H_e lead to slower current ramp-down as it was expected. Whereas in case of decreased λ_{T_e} and H_e the optimized trajectories for I_p are constrained mainly by the limit on dI_p/dt . Fig. 4.9 shows that the optimized trajectory is not too sensitive to the transport model. There is also no big difference in the optimized trajectories for κ_b . However, it should be mentioned that additional constraints can better demonstrate effects of transport model parameters on the optimized plasma elongation. For example, β_N is proportional to the volume averaged pressure, therefore it depends on the plasma energy and plasma volume. Increased λ_{T_e} leads to higher thermal energy and, to keep β_N within the required limit, the optimization algorithm can ask for a higher volume, i.e. higher kappa. Such sensitivity study can be very useful for real-time control and preparation of discharges, providing not just a trajectory for a plasma actuator but an area where a plasma is known to be within the physical/technical limits for a wide range of transport parameters.

4.6.2 Trajectories sensitivity to the geometry interpolation

In this work, since RAPTOR does not have an equilibrium solver, the geometrical terms have to be updated at every optimization iteration, as it has been mentioned in Subsec. 4.2.1. To check the sensitivity of the optimized trajectories on this assumption, we rerun the CHEASE code with profiles provided by RAPTOR to get new equilibria. Pressure and current density profiles, simulated by RAPTOR after optimization in I_p and κ_b in Subsec. 4.3.1, are used by CHEASE to reconstruct new equilibria with optimized I_p and κ_b . Then we rerun the optimization with the same parameters as in Subsec. 4.3.1 but with new geometrical quantities. Also reference trajectories for I_p and κ_b in this case are the same as the optimized trajectories obtained with old CHEASE equilibria in Subsec. 4.2.1. New optimized trajectories are demonstrated in Fig. 4.10. I_p and κ stay similar, confirming the minimum found in Subsec. 4.3.1. There are some differences in l_i and dB_v/dt trajectories obtained with initial and reconstructed CHEASE equilibria. However, globally they follow the same directions and stay within the required limits.

For further improvement of the optimization procedure, instead of the simple interpolation of the geometrical quantities, equilibrium reconstruction can be included at every iteration of the optimization loop. Using optimized I_p and κ_b trajectories and pressure and current density profiles simulated by RAPTOR, new equilibria can be calculated by CHEASE. It probably will slow down the optimization process, but will improve consistency between plasma geometry and dynamics.

4.7 Summary

In this chapter we have introduced the automatic optimization algorithm and demonstrated its applications for an optimization of the ramp-down phase of a plasma discharge. It has been

Chapter 4. Optimization of the ramp-down phase

developed in [Felici(2011), Felici et al.(2012)] and extended with new cost and constraint terms during this work. The algorithm by itself can be applied to any phase of a plasma discharge. In [Felici(2011), Felici et al.(2012)] it has been used for an optimization of the ramp up phase, where the optimization goal has been defined as reaching the specific plasma state at the end of the phase. For the ramp-down optimization, it is more important to define a full trajectory for plasma actuators, described in Subsec. 4.2.1, guiding plasma from the high energetic state at the end of the flat top phase to the low dense and colder plasma. Therefore, cost terms related to plasma integrated quantities (the plasma current, the input power, the plasma elongation), defined in Subsec. 4.2.2, have been implemented to the algorithm. During the ramp-down phase, because of rapid simultaneous changes in the plasma equilibrium, density and heat confinement, plasma stability limits can be easily violated. Moreover technical requirements for a machine, explained by safety reasons and control capabilities of the external magnetic coils, impose additional restrictions on the plasma ramp-down trajectories. It is not possible to take into account all physical and technical limits, described in Sec. 4.1. We concentrated on a few of them, related to the main stability limits and know technical limits for TCV, AUG and JET tokamaks, described in details in Subsec. 4.2.3.

The numerical optimization of the ramp-down phase for TCV L-mode plasmas in Sec. 4.3 has shown that a faster decrease in the plasma current is possible with a simultaneous reduction in the plasma elongation. The following experimental test confirmed that trajectories obtained with the help of the optimization algorithm bring the plasma to the low temperature and density state faster than the reference case and without disruptions. In addition, the time evolution of the plasma state during this fast ramp-down followed very well the predicted trajectory, validating RAPTOR simulations and the optimization procedure. The numerical optimization of the AUG ramp-down phase in Sec. 4.4 has been complemented by searching an optimal time instant of the H-L transition. The plasma internal inductance stays low even in case of a fast current ramp-down with the corresponding decrease in the plasma elongation. Also, it was found that with an earlier reduction in the input power, thus with an earlier H-L transition, β_{pol} experiences a smaller drop, which might be important for plasma MHD stability. Experimental tests on AUG have been complicated because of technical limits of the machine, nevertheless we have observed a positive effect of the plasma shaping. Preliminary numerical optimization for JET plasmas in Sec. 4.5 have been carried out in similar way as for TCV and AUG tokamaks but requires further development of the set of physical and technical constraints.

The future research directions on the ramp-down optimization are related to adding new physical and technical constraints. In the presented optimizations the electron density n_e has been considered as a prescribed (TCV, AUG) or predicted (JET) parameter. The Greenwald density limit has been the upper constraint for the line averaged electron density, thus for n_e too. However, there were no technical limits related directly to the density control. A constraint related to dn_e/dt , determined by plasma properties and allowed by a machine control system, will be an additional limit on n_e by itself, and therefore on the I_p ramp-down trajectory. Developing the impurity model in the RAPTOR code will allow to include physical constraints

on the radiated power, to avoid the generation of strong hollow temperature profiles which can lead to the plasma radiative collapse and the following plasma disruption. Further study of optimal trajectories sensitivity to the transport model parameters is required. As it has been shown in Subec. 4.6.1, that optimal trajectories are somewhat sensitive to the chosen set of the transport model parameters. Tests of the trajectories provided by RAPTOR with more sophisticated code, like ASTRA [Pereverzev and Yushmanov(2002)], are also required to verify dynamics of the plasma state. Since RAPTOR focuses on simulations of the plasma state evolution, the optimization algorithm uses plasma physical parameters only. Testing the optimized trajectories with full tokamak codes, like DINA [Khayrutdinov and Lukash(1993)], will allow to check their consistency with a machine technical requirements. Ramp-down specifications for ITER can be defined with the help of multi-machine analysis and numerical simulations [De Vries et al.(2018)]. However the results and proof-of-principle presented here demonstrate the capabilities of the present method and show already interesting directions for imposing termination strategies.

5 Conclusion

In this thesis we focus on the improvement of the RAPTOR code to extend its predictive capabilities, allowing for realistic simulations of plasma profiles on global time scales, and to contribute to the development of plasma termination scenarios.

5.1 Summary on the RAPTOR code updates

In order to develop a fast plasma simulator compatible with real-time plasma control, a new rapid transport simulator RAPTOR has been introduced in [Felici(2011), Felici et al.(2011)]. It has been developed for off-line and real-time predictions of coupled evolution of the poloidal flux and the electron temperature. To save calculation time, the code does not reconstruct the plasma equilibrium by itself but requires prescribed equilibria. Also it has simplified models for calculation of the transport coefficients and description of the heating profiles. In [Felici(2011), Felici et al.(2011)], transport equations have been determined in case of a fixed plasma equilibrium. This condition may lead to inaccurate prediction of the evolution of plasma profiles in case of rapid changes in plasma equilibrium and geometry, which naturally take place during the phases of current ramp-up and ramp-down. In Chapter 2, we have given a brief overview on the main features of the code and its upgrades related to the extension of the predictive capabilities of the code.

In particular, the RAPTOR transport model has been supplemented with new diffusion equations. At this moment, it includes diffusion equations for the poloidal flux, electron and ion temperatures, and density of various plasma species, allowing coupled simulations for all plasma species, presented in Sec 2.3. The diffusion equations have been extended with time-varying terms, thus RAPTOR is able to take into account the evolution of the plasma geometry and equilibrium. A special procedure for processing the equilibrium data has been developed, as discussed in Sec. 2.2. An equilibrium data file in EQDSK/EXPEQ format, provided by an equilibrium reconstruction code (like LIUQE [Hofmann et al.(1988)] for TCV, CLISTE [Schneider et al.(2000)] for AUG or EFIT [Lao et al.(1985a)] and EQUINOX [Mazon et al.(2010)] for JET), can be used by the CHEASE code to construct a data set in the

Chapter 5. Conclusion

format, compatible with the RAPTOR code. If equilibrium data files are provided for several time instants, we assume a linear time evolution of the plasma quantities between them. In addition to CHEASE data files, this preparation procedure of the equilibrium data can also use ASTRA [Pereverzev and Yushmanov(2002)] data files. In real-time, there is an option to get an output of a real-time equilibrium reconstruction code like RT-LIUQE [Moret et al.(2015)] for TCV. Predictive simulations of the diffusion of the plasma current are coupled with plasma kinetic profiles for self-consistent simulations of the time evolution of the plasma state. We have proved the validity of the code upgrades with several verification tests. In Sec. 2.4, we check RAPTOR simulations in case of time-varying geometry with the help of the ASTRA code. In Sec. 2.5 to prove the validity of the new transport equations for plasma particles (Eq. 2.32 and ion temperature (Eq. 2.24), we have performed benchmarks versus the CRONOS code [Artaud et al.(2010)] and ITER data for particle transport [Na et al.(2016)].

To improve predictive capabilities of the code over the entire plasma discharge, transport models capable to simulate transitions between low (L) and high (H) confinement modes and to simulate up to the plasma boundary ($\hat{\rho} = 1$) are required. Also these models have to be simple and fast to keep high calculation speed. We have implemented in the RAPTOR code a new model, based on [Kim et al.(2016)], which provides transport coefficients for the electron temperature and density. In this model the plasma profiles are assumed to be “stiff” in the core region (excluding ITBs), which is defined between ρ_{inv} ($q = 1$ radial position defining the plasma region affected by sawtooth crashes) and ρ_{ped} (radial position of the pedestal for L- and H-modes [Sauter et al.(2014)]). Stiffness of profiles reflects their ability to resist to changes in the heat flux [Garbet et al.(2004), Sauter et al.(2014)] and weak dependence on the global confinement properties. However, the model developed in [Kim et al.(2016)] is not suitable for modelling plasma experiencing fast transitions between L- and H-modes, because some of its parameters are averaged over several confinement times. The gradient-based transport model, described in Sec. 2.6, uses a PI controller to allow fast switching between L- and H-modes, taking into account such characteristic changes in plasma profiles as varying width of the pedestal and core profiles flattening. Thus heat and particle transport coefficients, described with Eqs. 2.52, 2.60, 2.61, evolve on characteristic plasma time scales. The gradient-based transport model requires prescribed parameters like the energy confinement factor, effective scalelengths for temperature/density, and the line averaged density. They are usually known from an experiment, thus can be easily checked and constrained with experimental measurements. They are also easily known in real-time, thus the model can be adapted if required, keeping its real-time predictive capabilities. In this work we focus on the electron heat and particle transport, however, there is also an option for future tests on the ion heat diffusivity, described in Subsec. 2.6.3.

The developed gradient-based transport model is rather promising for off-line and real-time plasma modelling, since it predicts well plasma profiles on long plasma time scales but still is simple enough to keep the high calculation speed. In this work, the model is used for off-line predictive plasma simulations. To be used in real-time, the model still has to be optimized, since the PI controller requires additional Newton iterations for the solution convergence.

5.2. Summary on realistic plasma profiles simulations with the RAPTOR code

However, useful options for its future application in real-time can already be mentioned. Since the model describes the plasma behavior typical for a confinement mode/machine, any deviation between predicted and measured plasma profiles can be used as an alarm for the control system. Thus, for example, periods of degraded plasma confinement can be determined, informing about the presence of NTMs, impurity accumulation or of failure of some diagnostics.

Development of real-time controllers, capable of realistic prediction of the plasma behavior, is an essential task for safe operation of future tokamaks. Complex codes like CRONOS [Artaud et al.(2010)], developed for plasma integrated modelling, include many precise physical modules, which take significant processing time. With RAPTOR we are aiming to develop a fast and reliable plasma simulator which can be used for plasma supervision and forecasting in real-time [Humphreys et al.(2015)]. The code upgrades, implemented as part of this thesis, improve predictive capabilities of the code in case of time-varying plasma geometry. New diffusion equations with fast transport models open more opportunities for development of real-time controllers. An implementation of fast transport models for plasma impurity will be useful for off-line simulations of the plasma radiated power and development of real-time controllers related to impurity accumulation.

5.2 Summary on realistic plasma profiles simulations with the RAPTOR code

To validate the gradient-based transport model, implemented in the code as part of this thesis, we have performed simulations over the entire plasma discharge for TCV, AUG and JET tokamaks. This model requires a few prescribed parameters, which can be defined from experimental measurements. Thus, another goal was to define typical ranges of the transport parameters for various machines and confinement regimes. The shape of the plasma profiles for electrons in the “stiff” region is characterized by a constant logarithmic gradient λ_{T_e, n_e} , which is related to the inverse scale length $R/L_{T_e, n_e}$. Therefore, λ_{T_e, n_e} can be defined from experimental data and verified with gyrokinetic simulations. To defined the height of the pedestal for T_e and n_e we use integrated parameters like the confinement factor for electron energy H_e for T_e profiles and the line-averaged density n_{el} for n_e profiles, obtained from the experimental measurements. We have defined H_e for L- and H-mode, assuming that there is no local improvement or degradation in electron energy confinement.

Testing λ_{T_e, n_e} for TCV and AUG plasmas with predictive simulations for ψ , T_e and n_e we have determined its typical values for L- and H-modes. For TCV in Sec 3.2, $\lambda_{T_e} = 3.2/2.3$ and $\lambda_{n_e} = 2.0/1.0$ for L-/H-modes have given the best match with Thomson measurements over several entire discharge simulations (that is many measurements). Whereas for AUG in Sec. 3.3, we have obtained $\lambda_{T_e} = 3.0/2.3$ and $\lambda_{n_e} = 1.0/0.5$ for L-/H-mode. Note that λ_{T_e} are similar for TCV and AUG and stay in a good agreement with theoretical predictions of gyrokinetic studies [Jenko et al.(2005)] and experimental observations [Ryter et al.(2001)]. Difference in

Chapter 5. Conclusion

λ_{n_e} can come from different T_e/T_i ratio for TCV and AUG plasmas, but such a significant difference would be worth studying in more details. For JET plasmas in Sec. 3.3, same λ_{T_e, n_e} as for AUG have been used, showing that the main differences between these two machines is well encapsulated by the confinement scaling law and effective line-averaged density. With fixed λ_{T_e, n_e} and prescribed H_e and \bar{n}_e , we have obtained very good agreement with experimental signals for TCV, AUG and JET. Simulations have been performed for plasmas with various geometry and heating scenarios, confirming the wide validity of the applied transport models.

We have also shown several special cases when the obtained set of λ_{T_e, n_e} is not valid. Since we have not used coupled simulations of the plasma profiles and NTMs, their effect is not taken into account on the profiles of the transport parameters, as has been shown in Subsec. 3.2.2. Thus, T_e and n_e profiles simulated by RAPTOR are not affected by NTMs, which can lead to a difference in predicted and measured profiles. However, if NTMs are simulated, profiles of the transport coefficients will be locally changed, leading to modification of the plasma profiles. A special case of ECRH heating scenario has been considered for TCV plasma in Subsec. 3.2.3, where off-axis heating leads to heat confinement degradation. With an additional option, allowing to modify H_e factor as function of the radial deposition of ECRH, we have obtained realistic evolution of T_e and n_e profiles. Impurity accumulation can lead to generation of hollow temperature and density profiles, strongly decreasing λ_{T_e, n_e} . For AUG and JET plasmas in Subsec. 3.3.2 and 3.4.2, we have reduced λ_{T_e} and introduced a power density sink, related to radiated power, to simulate flattened and hollow T_e profiles. For density transport further data analysis is required.

We have demonstrated capability of the RAPTOR code to predict time and space evolution of T_e and n_e profiles for TCV, AUG and JET plasmas, including the pedestal regions, over all discharge phases from ramp-up to ramp-down. Several directions for the transport model development can be mentioned. Since in RAPTOR we approximate radial profiles for the input power densities by Gaussian curves, simulations with power density profiles provided by the codes like TRANSP [Hawryluk(1980)]/TORBEAM [Poli et al.(2001)] can help to clarify influence of this assumption. Coupled simulations of the plasma profiles with NTMs will be an important improvement for predictive capabilities of RAPTOR and thus prediction of heat and particle profiles. Significant differences between the constant characteristic gradient in the “stiff” region λ_{T_e, n_e} predicted by RAPTOR and obtained in real-time can be used for controllers/detector as an indicator of reduction in the heat flux caused by increased plasma radiation/impurities accumulation. Also an option to adjust λ_{T_e, n_e} , depending on the heat flux, and to have it radial-dependent will allow automatically to take into account strong central radiation, for example. Coupling with the neural network transport models like QuaLiKiz [Bourdelle et al.(2016), Citrin et al.(2017), Felici et al.(2018)] will allow to get information on expected heat flux, thus to check λ_{T_e, n_e} . For further testing of the model in real-time, typical values for the edge gradient μ_{T_e, n_e} from TCV, AUG and JET simulations can be used. Also μ_{T_e, n_e} can be estimated with the help of special codes like EPED [Snyder et al.(2011)]. It is planned to continue working on the model development for ions transport. Since the gradient-based model for ion heat transport is already implement in the RAPTOR code, further analysis of the

experimental data is required.

5.3 Summary on the numerical ramp-down optimization

As part of this thesis, an automatic optimization procedure have been developed for the final stage of the plasma discharge, which is characterized by simultaneous decrease in the plasma current, pressure and volume. The difficulty of the plasma termination phase is in a limited operational range to decrease plasma energy and density in a controlled way and without plasma disruptions. Machine operational requirements or plasma stability limits can be easily reached because of rapid changes in various plasma parameters. Since future fusion reactors, and ITER in particular, can withstand only a limited amount of disruptions, it is important to develop nondisruptive termination scenarios. In recent years, development of appropriate termination scenarios is carried out with the help of numerical [Kim et al.(2009), Casper et al.(2014), De Vries et al.(2018)] and experimental studies on various machines [Nunes et al.(2011), Bizzaro et al.(2016)]. However, with optimization algorithms, searching a termination trajectory can be performed automatically.

In [Felici(2011), Felici et al.(2012)] an automatic optimization procedure has been developed for the ramp-up phase of a plasma discharge. Cost and constraint functions define the goal of the optimization and the area, where an optimal solution can be found. We have extended this algorithm in order to perform an optimization of the plasma ramp-down phase. Cost function terms related to plasma integrated quantities (the plasma current, the input power, the plasma elongation) are defined in Subsec. 4.2.2. Thus, the optimization goal is defined as to find a way to ramp-down the plasma current, the plasma elongation (thus, the plasma volume) or the input power as fast as possible, i.e. to reduce stored plasma energy and forces acting on the vessel in case of a disruption during the ramp-down phase. From the wide set of plasma physical constraints and machine technical limits, described in sec. 4.1, we have chosen a few of them, concentrating on the parameters which can be taken into account or predicted by the RAPTOR code, as discussed in Subsec. 4.2.3. Exact values of the limited parameters depend on a machine. In this thesis we have tested the optimization procedure for TCV, AUG and JET plasmas.

We have mainly studied an influence of the plasma current, the plasma elongation and H-L transition on the time evolution of the plasma internal inductance and other related quantities. In the numerical optimization of the ramp-down phase for TCV L-mode plasmas in Sec. 4.3, we have shown that the rate of change in the vertical magnetic field can be kept low with a faster decrease in the plasma current if there is a reduction in the plasma elongation. In the successful experimental test of the optimized trajectories, the plasma state has evolved similar to RAPTOR predictions, validating the optimization procedure. It is also important to determine an appropriate scenario to ramp-down additional heating power, since plasma might be rather sensitive to the transition from H- to L-mode. Therefore, the AUG ramp-down phase in Sec. 4.4 is optimized in terms of the plasma current, the plasma elongation and the

Chapter 5. Conclusion

time instant of the H-L transition. We have found that faster decrease in the plasma elongation allows for a faster ramp-down of the plasma current, while the plasma internal inductance stays low. An earlier H-L transition leads to smaller drop in β_{pol} , reducing risks of the growth of a plasma MHD instability. In order to improve standard termination procedure for AUG, we have tried to test the optimized trajectories experimentally. Because of machine technical requirements, protecting the vessel from a fast ramp-down of the currents in the coils forming the central solenoid, it was not possible to test full optimized trajectories. However, we have observed that faster than usual ramp-down in the plasma current can be performed with a proper plasma shaping and reduction of the additional heating power. Similar optimization has been tested for the JET ramp-down phase in Sec. 4.5, however it will be worth to develop an extended set of physical and technical constraints to specify a safe operation range for the machine.

The optimized trajectories also depend on the model which is used for plasma simulations. In Subec. 4.6.1, we have shown that variations in the prescribed transport parameters may lead to slightly different evolution of the plasma state, thus providing different optimized trajectories. An information about variations in the optimized trajectories for a wide set of transport parameters can be used by real-time controllers to define an area where a plasma is known to be within the physical/technical limits. Since RAPTOR does not have an equilibrium reconstruction solver, recalculation of the plasma equilibrium by, for example, the CHEASE code during the optimization loop will provide more accurate information about evolution of the plasma geometrical parameters. However, even with the simple scaling on the plasma elongation, used for this work, we have obtained a good representation of the plasma geometry, as it has been shown in Subsec. 4.6.2.

The optimization procedure can be improved with an extended set of the physical and technical constraints. It will allow to defined an area for searching the optimal trajectory more accurately for a specific machine. With further development of the RAPTOR code, physical limits related to the impurity accumulation and an increase in the radiated power, for example, can be taken into account. The optimized trajectories also can be tested with more complex codes, like ASTRA [Pereverzev and Yushmanov(2002)] and DINA [Khayrutdinov and Lukash(1993)], to verify dynamics of the plasma state and to check their consistency with the machine technical requirements. With this work, we have demonstrated the capability of the optimization algorithm, based on RAPTOR plasma simulations, to provide reliable plasma ramp-down trajectories.

A Equilibrium quantities required by RAPTOR

To solve the transport equations Eqs. 2.16-2.32, RAPTOR requires the following set of geometrical parameters to be prescribed on a normalized toroidal radial grid $\hat{\rho}$:

$$\begin{aligned}\hat{\rho} &= \sqrt{\Phi/\Phi_b} \\ V'_{\hat{\rho}} &= \frac{\partial V}{\partial \hat{\rho}} \\ g_0 &= \langle \nabla V \rangle, \quad g_1 = \langle (\nabla V)^2 \rangle, \quad g_2 = \left\langle \frac{(\nabla V)^2}{R^2} \right\rangle, \quad g_3 = \left\langle \frac{1}{R^2} \right\rangle. \\ F &= RB_{\phi}\end{aligned}$$

where Φ and Φ_b are the toroidal magnetic flux and its boundary value, V and $V'_{\hat{\rho}}$ denote to the plasma volume and its radial derivative, R is the main plasma radius, F is the poloidal current function, B_{ϕ} is the toroidal magnetic field. Information on these parameters is provided by external equilibrium codes.

Geometric coefficients from equilibrium code quantities

Equilibrium codes like LIUQE [Hofmann et al.(1988), Moret et al.(2015)], CHEASE [Lütjens et al.(1996)] return contour integrals C_i over flux surface quantities. Here, we provide the definition of the C_i coefficients in SI units:

$$\{C_0, C_1, C_2, C_3, C_4\} = \oint \left\{ \frac{1}{R}, 1, \frac{1}{R^2}, B_p^2, R^2 B_p^2 \right\} \frac{dl_p}{B_p} \quad (\text{A.1})$$

Definitions for $\frac{\partial V}{\partial \psi}$ and B_p in terms of COCOS [Sauter and Medvedev(2013)]:

$$B_p = \frac{1}{(2\pi)^{e_{B_p}}} \cdot \frac{|\nabla \psi|}{R} = \frac{\sigma_{B_p} \sigma_{I_p}}{(2\pi)^{e_{B_p}}} \cdot \frac{|\nabla \psi|}{R} \quad (\text{A.2})$$

$$\frac{\partial V}{\partial \psi} = \oint \sigma_{B_p} \sigma_{I_p} \cdot \frac{2\pi R}{|\nabla \psi|} dl_p = (2\pi)^{(1-e_{B_p})} \sigma_{B_p} \sigma_{I_p} \oint \frac{dl_p}{B_p} \quad (\text{A.3})$$

Appendix A. Equilibrium quantities required by RAPTOR

C_i coefficients in terms of COCOS:

$$C_0 = \oint \frac{1}{R} \frac{dl_p}{B_p} = (2\pi)^{e_{Bp}} \oint \frac{dl_p}{|\nabla\psi|} \quad (\text{A.4})$$

$$C_1 = \oint \frac{dl_p}{B_p} = (2\pi)^{e_{Bp}} \oint \frac{R dl_p}{|\nabla\psi|} \quad (\text{A.5})$$

$$C_2 = \oint \frac{1}{R^2} \frac{dl_p}{B_p} = (2\pi)^{e_{Bp}} \oint \frac{dl_p}{R|\nabla\psi|} \quad (\text{A.6})$$

$$C_3 = \oint B_p^2 \frac{dl_p}{B_p} = \oint B_p dl_p = \frac{1}{(2\pi)^{e_{Bp}}} \oint \frac{|\nabla\psi|}{R} dl_p \quad (\text{A.7})$$

$$C_4 = \oint R^2 B_p^2 \frac{dl_p}{B_p} = \oint R^2 B_p dl_p = \frac{1}{(2\pi)^{e_{Bp}}} \oint R |\nabla\psi| dl_p \quad (\text{A.8})$$

If one wants to normalize with the coefficients l_d for distance and l_B for magnetic field, one would get

$$C_0^{norm} = l_B \oint \frac{1}{R} \frac{dl_p}{B_p} = l_B C_0 \quad (\text{A.9})$$

$$C_1^{norm} = \frac{l_B}{l_d} \oint \frac{dl_p}{B_p} = \frac{l_B}{l_d} C_1 \quad (\text{A.10})$$

$$C_2^{norm} = l_d l_B \oint \frac{1}{R^2} \frac{dl_p}{B_p} = l_d l_B C_2 \quad (\text{A.11})$$

$$C_3^{norm} = \frac{1}{l_d l_B} \oint B_p^2 \frac{dl_p}{B_p} = \frac{1}{l_d l_B (2\pi)^{2e_{Bp}}} \oint \frac{(\nabla\psi)^2}{R^2} \frac{dl_p}{B_p} = \frac{1}{l_d l_B} C_3 \quad (\text{A.12})$$

$$C_4^{norm} = \frac{1}{l_d^3 l_B} \oint R^2 B_p^2 \frac{dl_p}{B_p} = \frac{1}{l_d^3 l_B (2\pi)^{2e_{Bp}}} \oint (\nabla\psi)^2 \frac{dl_p}{B_p} = \frac{1}{l_d^3 l_B} C_4 \quad (\text{A.13})$$

The system (A.9)-(A.13) provides the general definition of $C_0^{norm} - C_4^{norm}$ for any coordinate conventions and any normalization. The C_i coefficients are obtained with $l_d = l_B = 1$.

Flux surface averaged quantities from contour integrals

We rewrite $\frac{\partial V}{\partial\psi}$, g_1 , g_2 , g_3 , $\frac{\partial V}{\partial\rho}$ in terms of $C_0 - C_4$, introduced in Eqs. A.4-A.8 and in terms of $C_0^{norm} - C_4^{norm}$, defined in Eqs. A.9-A.13:

$$\frac{\partial V}{\partial\psi} = (2\pi)^{(1-e_{Bp})} \sigma_{Bp} \sigma_{Ip} C_1 = (2\pi)^{(1-e_{Bp})} \sigma_{Bp} \sigma_{Ip} \frac{l_d}{l_B} C_1^{norm} \quad (\text{A.14})$$

$$\begin{aligned} g_1 &= \langle (\nabla V)^2 \rangle = \left(\frac{\partial V}{\partial\psi} \right)^2 \cdot \langle (\nabla\psi)^2 \rangle = (2\pi)^{2(1-e_{Bp})} \oint \frac{dl_p}{B_p} \cdot \oint (\nabla\psi)^2 \frac{dl_p}{B_p} \\ &= (2\pi)^{2(1-e_{Bp})} C_1 \cdot (2\pi)^{2e_{Bp}} C_4 = 4\pi^2 C_1 C_4 = 4\pi^2 l_d^4 \cdot C_1^{norm} C_4^{norm} \end{aligned} \quad (\text{A.15})$$

$$\begin{aligned}
g_2 &= \left\langle \frac{(\nabla V)^2}{R^2} \right\rangle = \left(\frac{\partial V}{\partial \psi} \right)^2 \cdot \left\langle \frac{(\nabla \psi)^2}{R^2} \right\rangle = (2\pi)^{2(1-e_{Bp})} \oint \frac{dl_p}{B_p} \cdot \oint \frac{(\nabla \psi)^2 dl_p}{R^2 B_p} \\
&= (2\pi)^{2(1-e_{Bp})} C_1 \cdot (2\pi)^{2e_{Bp}} C_3 = 4\pi^2 C_1 C_3 = 4\pi^2 l_d^2 \cdot C_1^{norm} C_3^{norm}
\end{aligned} \tag{A.16}$$

$$g_3 = \left\langle \frac{1}{R^2} \right\rangle = \oint \frac{1}{R^2} \frac{dl_p}{B_p} / \oint \frac{dl_p}{B_p} = \frac{C_2}{C_1} = \frac{1}{l_d^2} \frac{C_2^{norm}}{C_1^{norm}} \tag{A.17}$$

$$\begin{aligned}
\frac{\partial V}{\partial \hat{\rho}} &= \frac{\partial V}{\partial \psi} \frac{\partial \psi}{\partial \Phi} \frac{\partial \Phi}{\partial \hat{\rho}} = (2\pi)^{(1-e_{Bp})} \sigma_{Bp} \sigma_{Ip} C_1 \cdot \frac{(2\pi)^{e_{Bp}}}{\sigma_{Ip} \sigma_{Bp} F C_2} \cdot 2\Phi_b \hat{\rho} = 4\pi \frac{C_1}{F C_2} \Phi_b \hat{\rho} \\
&= 4\pi \frac{l_d}{l_B} C_1^{norm} \frac{1}{F^{norm} C_2^{norm} \sigma_{B_0}} \cdot \Phi_b^{norm} l_d^2 l_B \sigma_{B_0} \hat{\rho} = 4\pi l_d^3 \frac{C_1^{norm}}{F^{norm} C_2^{norm}} \Phi_b^{norm} \hat{\rho}
\end{aligned} \tag{A.18}$$

where $\hat{\rho} = \sqrt{\Phi/\Phi_b}$. The toroidal flux is defined in the following way:

$$\Phi(\psi) = \int_{S_t} \mathbf{B} \cdot \mathbf{e}_\phi dS = \frac{1}{2\pi} \int_V \mathbf{B} \cdot \nabla \phi dV = \frac{1}{2\pi} \int_V \frac{F}{R^2} dV \tag{A.19}$$

Using the definition for \int_V ,

$$\int_V = (2\pi)^{(1-e_{Bp})} \sigma_{Bp} \sigma_{Ip} \int d\psi \oint \frac{dl_p}{B_p} \tag{A.20}$$

we derive $\partial\Phi(\psi)/\partial\psi$ in the following way:

$$\frac{\partial \Phi}{\partial \psi} = \frac{1}{(2\pi)^{e_{Bp}}} \sigma_{Bp} \sigma_{Ip} \oint \frac{F}{R^2} \frac{dl_p}{B_p} = \frac{1}{(2\pi)^{e_{Bp}}} \sigma_{Bp} \sigma_{Ip} F C_2 \tag{A.21}$$

Thus, if an equilibrium reconstruction code provides the contour integrals in form of C_i or C_i^{norm} and its COCOS is known, then geometrical quantities required by RAPTOR can be defined in the following way:

	SI units	RAPTOR in SI	Normalized
$\frac{\partial V}{\partial \psi}$	$(2\pi)^{1-e_{Bp}} \sigma_{Bp} \sigma_{Ip} C_1$	C_1	$(2\pi)^{1-e_{Bp}} \sigma_{Bp} \sigma_{Ip} \frac{l_d}{l_B} C_1^{norm}$
g_1	$4\pi^2 C_1 C_4$	$4\pi^2 C_1 C_4$	$4\pi^2 l_d^4 C_1^{norm} C_4^{norm}$
g_2	$4\pi^2 C_1 C_3$	$4\pi^2 C_1 C_3$	$4\pi^2 l_d^2 C_1^{norm} C_3^{norm}$
g_3	C_2/C_1	C_2/C_1	$\frac{1}{l_d^2} C_2^{norm} / C_1^{norm}$
$\frac{\partial V}{\partial \hat{\rho}}$	$4\pi \frac{C_1}{F C_2} \Phi_b \hat{\rho}$	$4\pi \frac{C_1}{F C_2} \Phi_b \hat{\rho}$	$4\pi l_d^3 \frac{C_1^{norm}}{F^{norm} C_2^{norm}} \Phi_b^{norm} \hat{\rho}$

RAPTOR has $COCOS = 11$ $l_d = 1$, $l_B = 1$, $e_{Bp} = 1$, $\sigma_{Bp} = 1$, $\sigma_{Ip} = 1$, $\sigma_{R\phi Z} = 1$ $\sigma_{\rho\theta\phi} = 1$, $\sigma_{B_0} = 1$. Contour integrals in SI units can be defined with CHEASE quantities with $COCOS = 2$: $l_d = R_0$,

Appendix A. Equilibrium quantities required by RAPTOR

$l_B = B_0$, $e_{Bp} = 0$, $\sigma_{Bp} = 1$, $\sigma_{I_p} = 1$, $\sigma_{\rho\theta\phi} = 1$, $\sigma_{B_0} = 1$, where

$$C_0 = \frac{1}{B_0} C_0^{CH}, C_1 = \frac{R_0}{B_0} C_1^{CH}, C_2 = \frac{1}{R_0 B_0} C_2^{CH}, C_3 = R_0 B_0 C_3^{CH}, \quad (\text{A.22})$$

$$C_4 = R_0^3 B_0 C_4^{CH}, F = R_0 B_0 F^{CH}, \Phi_b = R_0^2 B_0 \Phi_b^{CH} \quad (\text{A.23})$$

Other plasma quantities related to magnetic flux can be defined with C_i contour integrals. Here, we write expressions for the safety factor q and the plasma current I_p .

$$q = \frac{\sigma_{Bp} \sigma_{\rho\theta\phi}}{(2\pi)^{1-e_{Bp}}} \frac{\partial\Phi}{\partial\psi} = \sigma_{I_p} \sigma_{\rho\theta\phi} \frac{1}{2\pi} F C_2 = \sigma_{I_p} \sigma_{\rho\theta\phi} \sigma_{B_0} \frac{1}{2\pi} F^{norm} C_2^{norm} \quad (\text{A.24})$$

Using the I_p definition similar to the ASTRA code:

$$I_p = \int j_\phi dS_\phi = \frac{\sigma_{Bp}}{(2\pi)^{e_{Bp}-1} \mu_0} G_2 \frac{\partial\psi}{\partial\rho} \quad (\text{A.25})$$

where

$$G_2 = \frac{V'}{4\pi^2} \left\langle \left(\frac{\nabla\rho}{r} \right)^2 \right\rangle \quad (\text{A.26})$$

we can rewrite I_p in RAPTOR terms:

$$I_p = \frac{\sigma_{Bp}}{(2\pi)^{e_{Bp}+2}} \frac{1}{2\mu_0 \Phi_b} F \frac{g_2 g_3}{\hat{\rho}} \frac{\partial\psi}{\partial\hat{\rho}} = \frac{\sigma_{Bp}}{(2\pi)^{e_{Bp}+2}} \frac{1}{\mu_0} \frac{F}{q} g_2 g_3 \quad (\text{A.27})$$

and its toroidal density:

$$j_{tor} = 2\pi R_0 \frac{\partial I_p l}{\partial V} = \frac{\sigma_{Bp}}{(2\pi)^{e_{Bp}+2}} \frac{2\pi R_0}{2\mu_0 \Phi_b V'_\rho} \frac{\partial}{\partial\hat{\rho}} \left[F \frac{g_2 g_3}{\hat{\rho}} \frac{\partial\psi}{\partial\hat{\rho}} \right] \quad (\text{A.28})$$

If series of contour integrals are known for several time instants, parameters $\frac{\partial V}{\partial\psi}$, g_1 , g_2 , g_3 , $\frac{\partial V}{\partial\hat{\rho}}$ are calculated for each of them. Then to get the full time evolution, the parameters are interpolated linearly from their own time grid to RAPTOR time grid. At this moment RAPTOR interface allows to work with contour integrals provided by CHEASE [Lütjens et al.(1996)], ASTRA [Pereverzev and Yushmanov(2002)] and RT-LIUQE [Moret et al.(2015)]. Other codes, like EFIT [Lao et al.(1985a)] and CLISTE [Schneider et al.(2000)], have to provide equilibrium data files in EQDSK/EXPEQ format firstly. Then, these data files are reprocessed by the CHEASE code, and data files in CHEASE format are used by RAPTOR.

B Numerical implementation of the transport equations

In the RAPTOR code, the system of ODEs, constructed by Eqs. 2.16, 2.24 and 2.32, is solved by using the method of finite elements [Felici et al.(2011)]. As in [Felici et al.(2011)], the solution of an inhomogeneous equation of the form

$$m(\rho, t) \frac{\partial y}{\partial t} = \frac{\partial}{\partial \rho} \left[g(\rho, t) \frac{\partial y}{\partial \rho} \right] + k(\rho) j(\rho, t) \quad (\text{B.1})$$

can be written as $y(\rho, t) \approx \sum_{\alpha=1}^{n_{sp}} \hat{y}_{\alpha}(t) \Lambda_{\alpha}(\rho)$. Here Λ_{α} are the finite element basis functions.

In order to easily use the finite element method, the terms of Eqs. 2.16, 2.24 and 2.32 have to be regrouped to eliminate the term in front of the second order derivative, since an integration by part is used later.

The diffusion equation for the poloidal flux

The diffusion equation for the poloidal flux ψ Eq. 2.16 can be written in the following form:

$$m_{\psi} \frac{\partial \psi}{\partial t} = a_{\psi} \frac{\partial \psi}{\partial \hat{\rho}} + \frac{\partial}{\partial \hat{\rho}} d_{\psi} \frac{\partial \psi}{\partial \hat{\rho}} + s_{\psi} \quad (\text{B.2})$$

with

$$\begin{aligned} m_{\psi} &= 16\pi^2 \mu_0 \hat{\rho} \frac{\Phi_b^2 \sigma_{\parallel}}{F^2} \\ a_{\psi} &= 8\pi^2 \mu_0 \dot{\Phi}_b \Phi_b \frac{\sigma_{\parallel} \hat{\rho}^2}{F^2} \\ d_{\psi} &= \frac{g_2 g_3}{\hat{\rho}} \\ s_{\psi} &= -8\pi^2 \mu_0 \Phi_b \frac{V'}{F^2} \langle \mathbf{j}_{ni} \cdot \mathbf{B} \rangle \end{aligned}$$

where Φ_b is the toroidal flux at the plasma boundary, σ_{\parallel} is the plasma conductivity, \mathbf{j}_{ni} and \mathbf{B} denote to non-inductive current density and the magnetic field, F is the poloidal current

Appendix B. Numerical implementation of the transport equations

function; V'_ρ , g_2 , g_3 are plasma geometrical parameters, defined in Appendix A. Note that with respect to [Felici et al.(2012)] a new term a_ψ has been added to reflect the time dependence of the toroidal enclosed flux Φ .

If we write ψ as a sum of spatial basis functions

$$\psi(\rho, t) = \sum_{\alpha=1}^{n_{sp}} \Lambda_\alpha(\hat{\rho}) \hat{y}_\alpha(t) \quad (\text{B.3})$$

then the weak form, after projection on Λ_b and integration by parts can be written in the following way:

$$\begin{aligned} \sum_{\alpha=1}^{n_{sp}} \frac{d\hat{y}_\alpha(t)}{dt} \int_0^1 m \Lambda_\beta \Lambda_\alpha d\hat{\rho} &= \sum_{\alpha=1}^{n_{sp}} \hat{y}_\alpha \int_0^1 a_\psi \Lambda_\beta \frac{\partial \Lambda_\alpha}{\partial \hat{\rho}} d\hat{\rho} \\ - \sum_{\alpha=1}^{n_{sp}} \hat{y}_\alpha \int_0^1 d_\psi \frac{\partial \Lambda_\beta}{\partial \hat{\rho}} \frac{\partial \Lambda_\alpha}{\partial \hat{\rho}} d\hat{\rho} &+ \left[d_\psi \Lambda_\beta \frac{\partial \psi}{\partial \hat{\rho}} \right]_0^1 + \int_0^1 \Lambda_\beta s_\psi d\hat{\rho} \end{aligned} \quad (\text{B.4})$$

which gives the matrix form of Eq. B.2:

$$\mathbf{M}_\psi \frac{d\hat{\psi}}{dt} = (-\mathbf{D}_\psi + \mathbf{A}_\psi) \hat{\psi} + \mathbf{l} + \mathbf{s} \quad (\text{B.5})$$

The boundary term \mathbf{l} contains only the last element

$$d_\psi \Lambda_\beta \frac{\partial \psi}{\partial \hat{\rho}} \Big|_{\rho=1} = \frac{g_2 g_3}{\hat{\rho}} \frac{\partial \psi}{\partial \hat{\rho}} \Big|_{\rho=1} = \frac{16\pi^3 \mu_0 \Phi_b}{F} \Big|_{\rho=1} I_p \quad (\text{B.6})$$

The diffusion equation for the plasma energy

In the same way the diffusion equation for the plasma temperature, defined in Eq. 2.24, can be written:

$$m_{T_s} \frac{\partial T_s}{\partial t} = a_{T_s} \frac{\partial T_s}{\partial \hat{\rho}} + \frac{\partial}{\partial \hat{\rho}} d_{T_s} \frac{\partial T_s}{\partial \hat{\rho}} + h_{T_s} T_s + s_{T_s} \quad (\text{B.7})$$

with

$$m_{T_s} = \frac{3}{2} V'_{\hat{\rho}} n_s \quad (\text{B.8})$$

$$a_{T_s} = \frac{3}{2} \hat{\rho} n_s V'_{\hat{\rho}} \frac{\dot{\Phi}_b}{2\Phi_b} \quad (\text{B.9})$$

$$d_{T_s} = \frac{g_1}{V'_{\hat{\rho}}} n_s \chi_s \quad (\text{B.10})$$

$$h_{T_s} = \frac{\dot{\Phi}_b}{2\Phi_b} \hat{\rho} n_s \frac{\partial V'_{\hat{\rho}}}{\partial \hat{\rho}} - \frac{5}{2} n_s \frac{\partial V'_{\hat{\rho}}}{\partial t} - \frac{3}{2} V'_{\hat{\rho}} \frac{\partial n_s}{\partial t} \quad (\text{B.11})$$

$$s_{T_s} = V'_{\hat{\rho}} P_s \quad (\text{B.12})$$

where the index “s” denotes to plasma species like electrons or ions; n_s and T_s are density and temperature of the plasma species; g_1 is a geometrical quantity, defined in Appendix A; χ_s is the heat diffusion coefficient.

As in the equation for the toroidal flux, the term a_{T_s} reflects changes caused by the time-varying enclosed toroidal flux $\dot{\Phi}_b$. Also a new term h_{T_s} has been defined to take into account the influence of the time evolution of the electron density and plasma volume.

For the T_s equation, we write T_s as a sum of spatial basis functions

$$T_s(\hat{\rho}, t) = \sum_{\alpha=1}^{n_{sp}} \Lambda_{\alpha}(\hat{\rho}) \hat{z}_{\alpha}(t) \quad (\text{B.13})$$

and we obtain the weak form, after projection on Λ_b and integration by parts, as

$$\begin{aligned} \sum_{\alpha=1}^{n_{sp}} \frac{d\hat{z}_{\alpha}(t)}{dt} \int_0^1 m_{T_s} \Lambda_{\beta} \Lambda_{\alpha} d\hat{\rho} &= - \sum_{\alpha=1}^{n_{sp}} \hat{z}_{\alpha} \int_0^1 a_{T_s} \frac{\partial \Lambda_{\beta}}{\partial \hat{\rho}} \Lambda_{\alpha} d\hat{\rho} + [a_{T_s} \Lambda_{\beta} T_s]_0^1 \\ &- \sum_{\alpha=1}^{n_{sp}} \hat{z}_{\alpha} \int_0^1 d_{T_s} \frac{\partial \Lambda_{\beta}}{\partial \hat{\rho}} \frac{\partial \Lambda_{\alpha}}{\partial \hat{\rho}} d\hat{\rho} + \left[d_{T_s} \Lambda_{\beta} \frac{\partial T_s}{\partial \hat{\rho}} \right]_0^1 \\ &+ \sum_{\alpha=1}^{n_{sp}} \hat{z}_{\alpha} \int_0^1 h_{T_s} \Lambda_{\beta} \Lambda_{\alpha} d\hat{\rho} + \int_0^1 \Lambda_{\beta} s_{T_s} d\hat{\rho} \end{aligned} \quad (\text{B.14})$$

which gives the matrix form

$$\mathbf{M}_{T_s} \frac{d\hat{T}_s}{dt} = (-\mathbf{A}_{T_s} - \mathbf{D}_{T_s} + \mathbf{H}_{T_s}) \hat{T}_s + \mathbf{l} + \mathbf{s} \quad (\text{B.15})$$

with the boundary term

$$\mathbf{l} = [a_{T_s} \Lambda_{\beta} T_s]_{\hat{\rho}=1} + \left[d_{T_s} \Lambda_{\beta} \frac{\partial T_s}{\partial \hat{\rho}} \right]_{\hat{\rho}=1} = \left(\left(\frac{3}{2} \hat{\rho} n_s V'_{\hat{\rho}} \frac{\dot{\Phi}_b}{2\Phi_b} - \frac{5}{2} \Gamma_e g_0 \right) T_s + \frac{g_1}{V'_{\hat{\rho}}} n_s \chi_s \frac{\partial T_s}{\partial \hat{\rho}} \right) \Big|_{\hat{\rho}=1} \quad (\text{B.16})$$

Note that in the code the boundary term \mathbf{l} is fixed at a prescribed value.

Appendix B. Numerical implementation of the transport equations

The diffusion equation for the plasma particles

The diffusion equation for plasma particles “s” Eq. 2.32 can be written in the following way:

$$m_{n_s} \frac{\partial n_s}{\partial t} = \frac{\partial}{\partial \hat{\rho}} (a_{n_s} n_s) + \frac{\partial}{\partial \hat{\rho}} d_{n_s} \frac{\partial n_s}{\partial \hat{\rho}} + h_{n_s} n_s + s_{n_s} \quad (\text{B.17})$$

with

$$m_{n_s} = V'_{\hat{\rho}} \quad (\text{B.18})$$

$$a_{n_s} = \frac{\dot{\Phi}_b}{2\Phi_b} V'_{\hat{\rho}} \hat{\rho} - V_s g_0 \quad (\text{B.19})$$

$$d_{n_s} = \frac{g_1}{V'_{\hat{\rho}}} D_s \quad (\text{B.20})$$

$$h_{n_s} = -\frac{\partial V'_{\hat{\rho}}}{\partial t} \quad (\text{B.21})$$

$$s_{n_s} = V'_{\hat{\rho}} S_s \quad (\text{B.22})$$

where V_s and D_s denote the particle pinch velocity and diffusion coefficient respectively.

Now we write n_s as a sum of spatial basis functions

$$n_s(\hat{\rho}, t) = \sum_{\alpha=1}^{n_{sp}} \Lambda_{\alpha}(\hat{\rho}) \hat{y}_{\alpha}(t) \quad (\text{B.23})$$

Then, similar to T_s , the weak form is written in the following way:

$$\begin{aligned} \sum_{\alpha=1}^{n_{sp}} \frac{d\hat{y}_{\alpha}(t)}{dt} \int_0^1 m_{n_s} \Lambda_{\beta} \Lambda_{\alpha} d\hat{\rho} &= - \sum_{\alpha=1}^{n_{sp}} \hat{y}_{\alpha} \int_0^1 a_{n_s} \frac{\partial \Lambda_{\beta}}{\partial \hat{\rho}} \Lambda_{\alpha} d\hat{\rho} + [a_{n_s} \Lambda_{\beta} n_s]_0^1 \\ &- \sum_{\alpha=1}^{n_{sp}} \hat{y}_{\alpha} \int_0^1 d_{n_s} \frac{\partial \Lambda_{\beta}}{\partial \hat{\rho}} \frac{\partial \Lambda_{\alpha}}{\partial \hat{\rho}} d\hat{\rho} + \left[d_{n_s} \Lambda_{\beta} \frac{\partial n_s}{\partial \hat{\rho}} \right]_0^1 \\ &+ \sum_{\alpha=1}^{n_{sp}} \hat{y}_{\alpha} \int_0^1 h_{n_s} \Lambda_{\beta} \Lambda_{\alpha} d\hat{\rho} + \int_0^1 \Lambda_{\beta} s_{n_s} d\hat{\rho} \end{aligned} \quad (\text{B.24})$$

which gives the matrix form

$$\mathbf{M}_{n_s} \frac{d\hat{n}_s}{dt} = (-\mathbf{A}_{n_s} - \mathbf{D}_{n_s} + \mathbf{H}_{n_s}) \hat{n}_s + \mathbf{l} + \mathbf{s} \quad (\text{B.25})$$

with the boundary term

$$\mathbf{l} = [a_{n_s} \Lambda_{\beta} n_s]_{\hat{\rho}=1} + \left[d_{n_s} \Lambda_{\beta} \frac{\partial n_s}{\partial \hat{\rho}} \right]_{\hat{\rho}=1} = \left(\left(\frac{\dot{\Phi}_b}{2\Phi_b} V'_{\hat{\rho}} \hat{\rho} - V_s g_0 \right) n_s + \frac{g_1}{V'_{\hat{\rho}}} D_s \frac{\partial n_s}{\partial \hat{\rho}} \right) \Bigg|_{\hat{\rho}=1} \quad (\text{B.26})$$

Note that in the code, as well as for T_s , the boundary term \mathbf{l} is fixed at a prescribed value.

C The PI controller for the electron transport models

A controlled edge gradient μ_{T_e} , defined in Eq. 2.57, allows to get good predictive results even with fast L-H and H-L transition. The block diagram of the controller is presented in Fig C.1. For an error estimation as part of the PI-feedback control, the prescribed $H_e(t)$ is required. For feedforward control, we use a simple scaling law based on prescribed plasma current $I_p(t)$, total input power $P_{in}(t)$ and line-averaged electron density $n_{el}(t)$. The transport parameter μ_{T_e} obtained after the combination of feedforward and feedback outputs is used for $\chi_e(\rho)$ calculation and to solve for the electron temperature $T_e(\rho)$ profile. The H_e factor, based on this $T_e(\rho)$, is used for feedback control at the next step. A similar controller has been build for μ_{n_e} , but only a feedback part is used at this moment. An error in this case is defined as the difference between prescribed and simulated line-averaged electron densities $n_{el}(t)$. Gains K_p and K_i at this moment are defined by the user, assuming higher values of the gains in case of larger simulation time step. Higher values of the gains increase sensitivity of the controller, allowing it to react faster to changes in plasma heat and particle confinement properties, however it can lead to a stronger deviation from the reference in case of large time steps. For further improvement of the controller, these gains can be defined automatically based on the chosen time step. In the present work, typical gains for μ_{T_e} and μ_{n_e} PI controllers are around

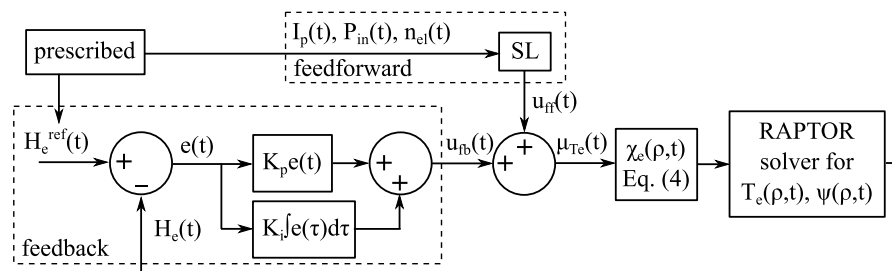


Figure C.1: The block diagram for the μ_{T_e} controller as a combination of PI feedback control with an error equal to $H_e^{ref} - H_e$ and feedforward control based on prescribed $I_p(t)$, $P_{in}(t)$ and $n_{el}(t)$.

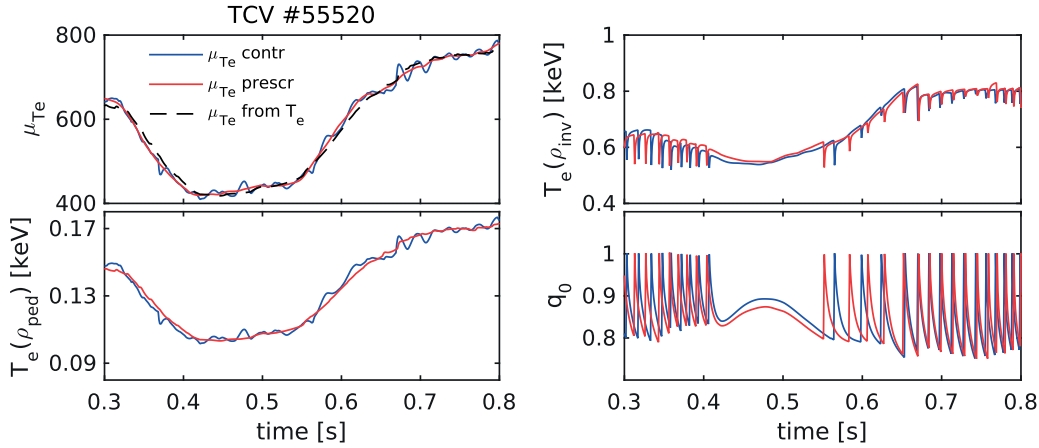


Figure C.2: Predictive simulations for T_e and ψ for the TCV shot #55520 in case of controlled and prescribed (smoothed) μ_{T_e} . Time evolution of the gradient μ_{T_e} , the electron temperature T_e at ρ_{ped} and $\rho_{inv} \approx 0.15$ and central safety factor q_0 are presented.

$1 \cdot 10^3$ and $5 \cdot 10^{19}$ for small time steps (like 1ms for TCV simulations) and $5 \cdot 10^3$ and $5 \cdot 10^{20}$ for larger time steps (like 10 ms for AUG and JET simulations).

In Fig. C.2, we demonstrate that the developed controller for μ_{T_e} does not disturb the physical result too much and even the frequencies of sawtooth oscillations are almost the same. The electron temperature T_e simulated with controlled μ_{T_e} (blue) is very close to the values obtained with prescribed μ_{T_e} (red), defined as a smoothed μ_{T_e} in the blue color. We also can check T_e gradient in the pedestal region (between 0.8 and 1.0 in this case), calculating it directly from the T_e profiles. This calculated gradient (black dashed) is very close to the prescribed μ_{T_e} , proving the correct implementation of the controller in the RAPTOR code.

The scaling law for the feed-forward controller

It is helpful if a reasonable feedforward value $\mu_{T_e}^{ff}$ can be provided. From the definition of the inverse scalelength R/L_{T_e} (Eq. 2.51), the constant gradient for the “pedestal” region can be written as

$$\mu_{T_e} = -\frac{dT_e}{d\rho} = -\frac{T_e(\rho_{ped}) - T_e^{BC}}{\rho_{ped} - \rho_{edge}} \quad (C.1)$$

where $T_e(\rho_{ped})$ is the pedestal electron temperature and T_e^{BC} is the prescribed electron temperature at the plasma edge. If an appropriate scaling law for the pedestal electron temperature (or electron pressure) is defined then μ_{T_e} can be easily found via the definition Eq. C.1.

A scaling law for the pedestal electron temperature has been defined from the central electron temperature using the constant logarithmic gradient of the “core” region λ_{T_e} :

$$T_e(\rho_{ped}) = T_{e0} \cdot e^{(\lambda_{T_e}(\rho_{ped} - \rho_{inv}))} \quad (C.2)$$

while the central temperature has been estimated from the $H_{98,y,2}$ scaling law for the energy confinement time [ITER Physics Expert Groups(1999a)] using typical values for the TCV plasma geometry parameters:

$$T_{e0}^{TCV} = 7.5 \cdot 10^3 \cdot (I_p[MA])^{0.93} \cdot (P_{tot}[MW])^{0.3} \cdot (n_{el}[10^{19}m^3])^{-0.6} \quad (C.3)$$

Inserting this into Eqs. C.2, C.1 yields the approximation for $\mu_{T_e}^{ff}$. For AUG and JET, we use the following expressions:

$$T_{e0}^{AUG} = 3.3 \cdot 10^3 \cdot (I_p[MA])^{0.93} \cdot (P_{tot}[MW])^{0.3} \cdot (n_{el}[10^{19}m^3])^{-0.6} \quad (C.4)$$

$$T_{e0}^{JET} = 4.1 \cdot 10^4 \cdot (I_p[MA])^{0.93} \cdot (P_{tot}[MW])^{0.3} \cdot (n_{el}[10^{19}m^3])^{-0.6} \quad (C.5)$$

Bibliography

- [Angioni et al.(2002)] C. Angioni et al. Neutral beam stabilization of sawtooth oscillations in JET. *Plasma Phys. Control. Fusion*, 44:205, 2002. <http://dx.doi.org/10.1088/0741-3335/44/2/305>.
- [Angioni et al.(2009)] C. Angioni et al. Particle transport in tokamak plasmas, theory and experiment. *Plasma Phys. Control. Fusion*, 51:124017, 2009. <http://dx.doi.org/10.1088/0741-3335/51/12/124017>.
- [Artaud et al.(2010)] J. F. Artaud et al. The CRONOS suite of codes for integrated tokamak modelling. *Nucl. Fusion*, 50:043001, 2010. <http://dx.doi.org/10.1088/0029-5515/50/4/043001>.
- [Artsimovich(1972)] L.A. Artsimovich. Tokamak devices. *Nucl. Fusion*, 12:215, 1972. <http://dx.doi.org/10.1088/0029-5515/12/2/012>.
- [Barton et al.(2015)] J. Barton et al. Physics-model-based nonlinear actuator trajectory optimization and safety factor profile feedback control for advanced scenario development in DIII-D. *Nucl. Fusion*, 55:093005, 2015. <http://dx.doi.org/10.1088/0029-5515/55/9/093005>.
- [Basiuk et al.(2003)] V. Basiuk et al. Simulations of steady-state scenarios for Tore Supra using the CRONOS code. *Nucl. Fusion*, 43:822–830, 2003. <http://dx.doi.org/10.1088/0029-5515/43/9/305>.
- [Becker(1988)] G. Becker. Empirical scaling laws for local transport in neutral beam heated plasmas. *Nucl. Fusion*, 28:1458, 1988. <http://dx.doi.org/10.1088/0029-5515/28/8/013>.
- [Bizzaro et al.(2016)] J. P. S. Bizzaro et al. Modelling the ohmic L-mode ramp-down phase of JET hybrid pulses using JETTO with Bohm–gyro-Bohm transport. *Plasma Phys. Control. Fusion*, 58:105010, 2016. <http://dx.doi.org/10.1088/0741-3335/58/10/105010>.
- [Blanken et al.(2018)] T. Blanken et al. Control-oriented modeling of the plasma particle density in tokamaks and application to real-time density profile reconstruction. *Fusion Eng. Design*, 126:87, 2018. <https://doi.org/10.1016/j.fusengdes.2017.11.006>.

Bibliography

- [Bourdelle et al.(2016)] C. Bourdelle et al. Core turbulent transport in tokamak plasmas: bridging theory and experiment with QuaLiKiz. *Plasma Phys. Control. Fusion*, 58: 014036, 2016. <http://dx.doi.org/10.1088/0741-3335/58/1/014036>.
- [Bowden et al.(1999)] M. D. Bowden et al. A Thomson scattering diagnostic system for measurement of electron properties of processing plasmas. *Plasma Sources Sci. Technol.*, 8: 203, 1999. <http://dx.doi.org/10.1088/0963-0252/8/2/002>.
- [Brambilla et al.(1999)] M. Brambilla et al. Numerical simulation of ion cyclotron waves in tokamak plasmas. *Plasma Phys. Control. Fusion*, 41:1, 1999. <https://doi.org/10.1088/0741-3335/41/1/002>.
- [Callen et al.(1987)] J. D. Callen et al. Neoclassical MHD equations, instabilities and transport in tokamaks. In *in Plasma Phys. and Contr. Nucl. Fusion Research 1986 (Proc. 11th Int. Conf. Kyoto, 1987), Vol. 2, IAEA (Vienna, Austria), 1987*.
- [Camenen et al.(2005)] Y. Camenen et al. Electron heat transport in shaped TCV L-mode plasmas. *Plasma Phys. Control. Fusion*, 47:1971, 2005. <http://dx.doi.org/10.1088/0741-3335/47/11/007>.
- [Canal(2013)] G.P. Canal. Fast seeding of NTMs by sawtooth crashes in TCV and their pre-emption using ECRH. *Nucl. Fusion*, 53:113026, 2013. <http://dx.doi.org/10.1088/0029-5515/53/11/113026>.
- [Carrera et al.(1986)] R. Carrera et al. Island bootstrap current modification of the nonlinear dynamics of the tearing mode. *Phys. Fluids*, 29:899, 1986. <https://doi.org/10.1063/1.865682>.
- [Casper et al.(2014)] T. Casper et al. Development of the ITER baseline inductive scenario. *Nucl. Fusion*, 54:013005, 2014. <http://dx.doi.org/10.1088/0029-5515/54/1/013005>.
- [Celata and Boyd(1977)] C.M. Celata and D.A. Boyd. Cyclotron radiation as a diagnostic tool for tokamak plasmas. *Nucl. Fusion*, 17:735, 1977. <http://dx.doi.org/10.1088/0029-5515/17/4/009>.
- [Cenacchi et al.(1988)] G. Cenacchi et al. *JETTO: a free-boundary plasma transport code, Rapporto ENEA RT/TIB (88)5, 1988*. <https://inis.iaea.org/search/search.aspx?origq=RN:19097143>.
- [Challis et al.(2002)] C. D. Challis et al. Influence of the q-profile shape on plasma performance in JET. *Plasma Phys. Control. Fusion*, 44:1031, 2002. <http://dx.doi.org/10.1088/0741-3335/44/7/301>.
- [Citrin et al.(2015)] J. Citrin et al. Real-time capable first principle based modelling of tokamak turbulent transport. *Nucl. Fusion*, 55:092001, 2015. <http://dx.doi.org/10.1088/0029-5515/55/9/092001>.

- [Citrin et al.(2017)] J. Citrin et al. Tractable flux-driven temperature, density, and rotation profile evolution with the quasilinear gyrokinetic transport model QuaLiKiz. *Plasma Phys. Control. Fusion*, 59:124005, 2017. <http://dx.doi.org/10.1088/1361-6587/aa8aeb>.
- [Coda et al.(2017)] S. Coda et al. Overview of the TCV tokamak program: scientific progress and facility upgrades. *Nucl. Fusion*, 57:102011, 2017. <http://dx.doi.org/10.1088/1741-4326/aa6412>.
- [Cooper and Wootton(1982)] W. A. Cooper and A. J. Wootton. β_p analysis for Tokamak plasma with anisotropic pressure and mass flow. *Plasma Phys.*, 24:1183, 1982. <http://dx.doi.org/10.1088/0032-1028/24/9/014>.
- [Coppi and Rewoldt(1974)] B. Coppi and G. Rewoldt. New trapped-electron instability. *Phys. Review Lett.*, 33:1329, 1974. <https://doi.org/10.1103/PhysRevLett.33.1329>.
- [Crotinger et al.(1997)] J. A. Crotinger et al. *Corsica: A Comprehensive Simulation of Toroidal Magnetic-Fusion Devices, Program LLNL Report UCRLID-126284*, 1997. <https://www.osti.gov/scitech/servlets/purl/522508>.
- [De la Luna et al.(2016)] E. De la Luna et al. Understanding the physics of ELM pacing via vertical kicks in JET in view of ITER. *Nucl. Fusion*, 56:026001, 2016. <https://doi.org/10.1088/0029-5515/56/2/026001>.
- [De Vries et al.(2012)] P. C. De Vries et al. The impact of the ITER-like wall at JET on disruptions. *Plasma Phys. Control. Fusion*, 54:124032, 2012. <http://dx.doi.org/10.1088/0741-3335/54/12/124032>.
- [De Vries et al.(2014)] P. C. De Vries et al. The influence of an ITER-like wall on disruptions at JET. *Phys. Plasmas*, 21:056101, 2014. <http://dx.doi.org/10.1063/1.4872017>.
- [De Vries et al.(2018)] P. C. De Vries et al. Multi-machine analysis of termination scenarios with comparison to simulations of controlled shutdown of ITER discharges. *Nucl. Fusion*, 58:026019, 2018. <http://dx.doi.org/10.1088/1741-4326/aa9c4c>.
- [Dunne et al.(2012)] M. G. Dunne et al. Measurement of neoclassically predicted edge current density at ASDEX Upgrade. *Nucl. Fusion*, 52:123014, 2012. <http://dx.doi.org/10.1088/0029-5515/52/12/123014>.
- [Erba et al.(1998)] M. Erba et al. Validation of a new mixed Bohm/gyro-Bohm model for electron and ion heat transport against the ITER, Tore Supra and START database discharges. *Nucl. Fusion*, 38:1013, 1998. <http://dx.doi.org/10.1088/0029-5515/38/7/305>.
- [Eriksson et al.(1993)] L.-G. Eriksson et al. Comparison of time dependent simulations with experiments in ion cyclotron heated plasmas. *Nucl. Fusion*, 33:1037, 1993. <https://doi.org/10.1088/0029-5515/33/7/I07>.

Bibliography

- [Eriksson et al.(1995)] L.-G. Eriksson et al. A model for calculating ICRH power deposition and velocity distribution. *Nucl. Fusion*, 33:1037, 1995. <https://doi.org/10.1088/0031-8949/52/1/014>.
- [Eriksson et al.(1998)] L.-G. Eriksson et al. ICRF heating of JET plasmas with the third harmonic deuterium resonance. *Nucl. Fusion*, 38:265, 1998. <http://dx.doi.org/10.1088/0029-5515/38/2/310>.
- [Fable et al.(2010)] E. Fable et al. The role of ion and electron electrostatic turbulence in characterizing stationary particle transport in the core of tokamak plasmas. *Plasma Phys. Control. Fusion*, 52:015007, 2010. <http://dx.doi.org/10.1088/0741-3335/52/1/015007>.
- [Fable et al.(2013)] E. Fable et al. Novel free-boundary equilibrium and transport solver with theory-based models and its validation against ASDEX Upgrade current ramp scenarios. *Plasma Phys. Control. Fusion*, 55:124028, 2013. <http://dx.doi.org/10.1088/0741-3335/55/12/124028>.
- [Favez et al.(2002)] J.-Y. Favez et al. Comparing TCV experimental VDE responses with DINA code simulations. *Plasma Phys. Control. Fusion*, 44:171, 2002. <http://dx.doi.org/10.1088/0741-3335/44/2/303>.
- [Felici(2011)] F. Felici. *Real-Time Control of Tokamak Plasmas: from Control of Physics to Physics-Based Control*. PhD thesis No 5203, EPFL, Lausanne, Switzerland, 2011. <http://infoscience.epfl.ch/record/168656>.
- [Felici et al.(2011)] F. Felici et al. Real-time physics-model-based simulation of the current density profile in tokamak plasmas. *Nucl. Fusion*, 51:083052, 2011. <http://dx.doi.org/10.1088/0029-5515/51/8/083052>.
- [Felici et al.(2012)] F. Felici et al. Non-linear model-based optimization of actuator trajectories for tokamak plasma profile control. *Plasma Phys. Control. Fusion*, 54:025002, 2012. <http://dx.doi.org/10.1088/0741-3335/54/2/025002>.
- [Felici et al.(2016)] F. Felici et al. Real-time model-based plasma state estimation, monitoring and integrated control in TCV, ASDEX-Upgrade and ITER. In *26th IAEA Fusion Energy Conference (Kyoto, Japan)*, 2016.
- [Felici et al.(2018)] F. Felici et al. Real-time-capable multichannel tokamak transport simulations using RAPTOR. *Nucl. Fusion*, to be submitted, 2018. incl. A. A. Teplukhina.
- [Fiedberg(1982)] J. P. Fiedberg. Ideal magnetohydrodynamic theory of magnetic fusion systems. *Rev. Modern Phys.*, 3:801, 1982. <https://doi.org/10.1103/RevModPhys.54.801>.
- [Fietz et al.(2013)] S. Fietz et al. Investigation of transport models in ASDEX Upgrade current ramps. *Nucl. Fusion*, 53:053004, 2013. <http://dx.doi.org/10.1088/0029-5515/53/5/053004>.

- [Fischer et al.(2003)] R. Fischer et al. Bayesian modelling of fusion diagnostics. *Plasma Phys. Control. Fusion*, 45:1095–1111, 2003. <http://stacks.iop.org/0741-3335/45/i=7/a=304>.
- [Garbet et al.(2004)] X. Garbet et al. Profile stiffness and global confinement. *Plasma Phys. Control. Fusion*, 46:1351, 2004. <https://dx.doi.org/10.1088/0741-3335/46/9/002>.
- [Goldberg(1989)] D. Goldberg. *Genetic Algorithms in Search, Optimization and Machine Learning*. MA: Addison-Wesley Professional, 1989.
- [Grad and Rubin(1958)] H. Grad and H. Rubin. Hydromagnetic equilibria and force-free fields. In *Proceedings of the 2nd UN Conf. on the Peaceful Uses of Atomic Energy Vol. 31. IAEA. Geneva, p. 190.*, 1958.
- [Greenwald(2002)] M. Greenwald. Density limits in toroidal plasmas. *Plasma Phys. Control. Fusion*, 44:R27, 2002. <https://dx.doi.org/10.1088/0741-3335/44/8/201>.
- [Hawryluk(1980)] R. J. Hawryluk. An empirical approach to tokamak transport. In *Physics of Plasmas Close to Thermonuclear Conditions (CEC, Brussels), Vol. 1., p. 19*, 1980.
- [Henderson et al.(2001)] M. A. Henderson et al. Poloidally asymmetric plasma response with ECH deposition near $q = 1$ in TCV. *Fusion Eng. Design*, 53:241, 2001. [https://doi.org/10.1016/S0920-3796\(00\)00493-2](https://doi.org/10.1016/S0920-3796(00)00493-2).
- [Hillesheim et al.(2013)] J. C. Hillesheim et al. Experimental characterization of multiscale and multifield turbulence as a critical gradient threshold is surpassed in the DIII-D tokamak. *Phys. Plasmas*, 20:056115, 2013. <https://doi.org/10.1063/1.4807123>.
- [Hinton(1991)] F. L. Hinton. Thermal confinement bifurcation and the L- to H-mode transition in tokamaks. *Phys. Fluids B: Plasma Phys.*, 3:696, 1991. <http://doi.org/10.1063/1.859866>.
- [Hinton and Hazeltine(1976)] F. L. Hinton and R. D. Hazeltine. Theory of plasma transport in toroidal confinement systems. *Rev. Modern Phys.*, 48:239, 1976. <http://doi.org/10.1103/RevModPhys.48.239>.
- [Hofmann et al.(1988)] F. Hofmann et al. Tokamak equilibrium reconstruction using Faraday rotation measurements. *Nucl. Fusion*, 28:1871, 1988. <http://dx.doi.org/10.1088/0029-5515/28/10/014>.
- [Hofmann et al.(1994)] F. Hofmann et al. Creation and control of variably shaped plasmas in TCV. *Plasma Phys. Control. Fusion*, 36:B227, 1994. <https://dx.doi.org/10.1088/0741-3335/36/12B/023>.
- [Hofmann et al.(1997)] F. Hofmann et al. Vertical instability in TCV: comparison of experimental and theoretical growth rates. *Nucl. Fusion*, 37:681, 1997. <http://dx.doi.org/10.1088/0029-5515/37/5/I10>.

Bibliography

- [Horton et al.(2004)] L. D. Horton et al. ITER-relevant H-mode physics at ASDEX Upgrade. *Plasma Phys. Control. Fusion*, 46:B511, 2004. <https://dx.doi.org/10.1088/0741-3335/46/12B/042>.
- [Horton and Hong(1988)] W. Horton and B. G. Hong. Toroidal electron temperature gradient driven drift modes. *Phys. Fluids*, 31:2971, 1988. <https://doi.org/10.1063/1.866954>.
- [Humphreys et al.(2015)] D. Humphreys et al. Novel aspects of plasma control in ITER. *Phys. of Plasma*, 22:021806, 2015. <http://dx.doi.org/10.1063/1.4907901>.
- [Imbeaux et al.(2011)] F. Imbeaux et al. Current ramps in tokamaks: from present experiments to ITER scenarios. *Nucl. Fusion*, 51:083026, 2011. <http://dx.doi.org/10.1088/0029-5515/51/8/083026>.
- [ITER Physics Expert Groups(1999a)] ITER Physics Expert Groups. *ITER Physics Basis, Chapter 2: Plasma confinement and transport*, 1999a. <http://dx.doi.org/10.1088/0029-5515/39/12/302>.
- [ITER Physics Expert Groups(1999b)] ITER Physics Expert Groups. *ITER Physics Basis, Chapter 3: MHD stability, operational limits and disruptions*, 1999b. <http://dx.doi.org/10.1088/0029-5515/39/12/303>.
- [Jackson et al.(2008)] G. L. Jackson et al. ITER startup studies in the DIII-D tokamak. *Nucl. Fusion*, 48:125002, 2008. <http://dx.doi.org/10.1088/0029-5515/48/12/125002>.
- [Jenko et al.(2001)] F. Jenko et al. Critical gradient formula for toroidal electron temperature gradient modes. *Phys. Plasmas*, 8:4096, 2001. <https://doi.org/10.1063/1.1391261>.
- [Jenko et al.(2005)] F. Jenko et al. Heat and particle transport in a tokamak: advances in nonlinear gyrokinetics. *Plasma Phys. Control. Fusion*, 47:B195, 2005. <http://dx.doi.org/10.1088/0741-3335/47/12B/S15>.
- [Kadomtsev(1975)] B. B. Kadomtsev. 1975 Fiz. Plasmy 1 710;. *Sov. J. Plasma. Phys*, 1:389, 1975.
- [Kallenbach et al.(2017)] A. Kallenbach et al. Overview of ASDEX Upgrade results. *Nucl. Fusion*, 57:102015, 2017. <http://dx.doi.org/10.1088/1741-4326/aa64f6>.
- [Kelley et al.(1972)] G.G. Kelley et al. Neutral-beam-injection heating of toroidal plasmas for fusion research. *Nucl. Fusion*, 12:169, 1972. <http://dx.doi.org/10.1088/0029-5515/12/2/004>.
- [Kessel(1994)] C. E. Kessel. Bootstrap current in a tokamak. *Nucl. Fusion*, 34:1221, 1994. <http://dx.doi.org/10.1088/0029-5515/34/9/I04>.
- [Khayrutdinov and Lukash(1993)] R. R. Khayrutdinov and V. E. Lukash. Studies of plasma equilibrium and transport in a tokamak fusion device with the inverse-variable technique. *J. Comp. Phys.*, 109:193, 1993. <http://dx.doi.org/10.1006/jcph.1993.1211>.

- [Kim(2015)] D. Kim. *Real-Time Control of Sawteeth and NTMs in TCV and ITER*. PhD thesis No 6539, EPFL, Lausanne, Switzerland, 2015. <http://infoscience.epfl.ch/record/205040>.
- [Kim et al.(2016)] D. Kim et al. Simple predictive electron transport models applied to sawtooth plasmas. *Plasma Phys. Control. Fusion*, 58:055002, 2016. <http://dx.doi.org/10.1088/0741-3335/58/5/055002>.
- [Kim et al.(2009)] S. H. Kim et al. Full tokamak discharge simulation of ITER by combining DINA-CH and CRONOS. *Plasma Phys. Control. Fusion*, 51:105007, 2009. <http://dx.doi.org/10.1088/0741-3335/51/10/105007>.
- [Kirk et al.(2004)] A. Kirk et al. ELM characteristics in MAST. *Plasma Phys. Control. Fusion*, 46:551, 2004. <http://dx.doi.org/10.1088/0741-3335/46/3/009>.
- [Kirneva et al.(2012)] N. A. Kirneva et al. Dependence of L-mode confinement on the electron cyclotron power deposition profile in the TCV tokamak. *Plasma Phys. Control. Fusion*, 54:015011, 2012. <http://dx.doi.org/10.1088/0741-3335/54/1/015011>.
- [Koch(2006a)] R. Koch. The Ion Cyclotron, Lower Hybrid and Alfvén wave heating methods. *Fus. Science Techn.*, 49 (2T):187, 2006a. <https://doi.org/10.13182/FST06-A1118>.
- [Koch(2006b)] R. Koch. Plasma heating by Neutral Beam Injection. *Fus. Science Techn.*, 49 (2T):167, 2006b. <https://doi.org/10.13182/FST06-A1116>.
- [Koechl et al.(2017)] F. Koechl et al. Modelling of transitions between L- and H-mode in JET high plasma current plasmas and application to ITER scenarios including tungsten behaviour. *Nucl. Fusion*, 57:086023, 2017. <https://doi.org/10.1088/1741-4326/aa7539>.
- [Lao et al.(1985a)] L. L. Lao et al. Reconstruction of current profile parameters and plasma shapes in tokamaks. *Nucl. Fusion*, 25:1611, 1985a. <http://dx.doi.org/10.1088/0029-5515/25/11/007>.
- [Lao et al.(1985b)] L. L. Lao et al. Separation of β_p and l_i in tokamaks of non-circular cross-section. *Nucl. Fusion*, 25:1421, 1985b. <http://dx.doi.org/10.1088/0029-5515/25/10/004>.
- [Lawson(1957)] J. D. Lawson. *Some criteria for a power producing thermonuclear reactor*, 1957. Proceedings of the Physical Society B70, 6.
- [Lehnen et al.(2013)] M. Lehnen et al. Impact and mitigation of disruptions with the ITER-like wall in JET. *Nucl. Fusion*, 53:093007, 2013. <http://dx.doi.org/10.1088/0029-5515/53/9/093007>.
- [Leonov et al.(2010)] M. Leonov et al. Study of ITER plasma current ramp-down scenarios with DINA and ASTRA codes. In *37th EPS Conf. on Plasma Phys. Control. Fusion (Dublin, Ireland)*, 2010. P2.182.
- [Lister et al.(2013)] J. Lister et al. Reducing radial movement in ITER H-L-mode back transitions. In *40th EPS Conf. on Plasma Phys. Control. Fusion (Espoo, Finland)*, 2013. P1.164.

Bibliography

- [Litaudon et al.(2017)] X. Litaudon et al. Overview of the JET results in support to ITER. *Nucl. Fusion*, 57:102001, 2017. <http://dx.doi.org/10.1088/1741-4326/aa5e28>.
- [Lütjens et al.(1996)] H. Lütjens et al. The CHEASE code for toroidal MHD equilibria. *Comp. Phys. Comm.*, 97:219–260, 1996. [http://dx.doi.org/10.1016/0010-4655\(96\)00046-X](http://dx.doi.org/10.1016/0010-4655(96)00046-X).
- [Ma et al.(1982)] C. H. Ma et al. Measurements of electron density and plasma current distributions in tokamak plasma. *Int. J. Infrared Milli Waves*, 3:263, 1982. <https://doi.org/10.1007/BF01007101>.
- [Martin et al.(2008)] Y. R. Martin et al. Power requirement for accessing the H-mode in ITER. *Jour. of Phys*, 123:012033, 2008. <http://dx.doi.org/10.1088/1742-6596/123/1/012033>.
- [Matsuda et al.(1989)] K. Matsuda et al. Ray tracing study of the electron cyclotron current drive in DIII-D using 60 GHz. *IEEE Trans. Plasma Scien.*, 17(1):6, 1989. <http://dx.doi.org/10.1109/27.21664>.
- [Mazon et al.(2010)] D. Mazon et al. *EQUINOX: A Real-Time Equilibrium Code and its Validation at JET*. World Scientific Book Series on Nonlinear Science Series B, 15, World Scientific, London, 2010.
- [Meneghini et al.(2017)] O. Meneghini et al. Self-consistent core-pedestal transport simulations with neural network accelerated models. *Nucl. Fus.*, 57:086034, 2017. <http://dx.doi.org/10.1088/1741-4326/aa7776>.
- [Merle et al.(2017)] A. Merle et al. Pedestal properties of H-modes with negative triangularity using the EPED-CH model. *Plasma Phys. Control. Fusion*, 59:10400, 2017. <http://dx.doi.org/10.1088/1361-6587/aa7ac0>.
- [Miyamoto(2005)] K. Miyamoto. *Plasma Physics and Controlled Nuclear Fusion*. Springer Series on Atomic, Optical, and Plasma Physics, Volume 38, Springer-Verlag Berlin Heidelberg, 2005.
- [Moreau et al.(2011)] D. Moreau et al. Plasma models for real-time control of advanced tokamak scenarios. *Nucl. Fus.*, 51:063009, 2011. <http://dx.doi.org/10.1088/0029-5515/51/6/063009>.
- [Moret et al.(2003)] J.-M. Moret et al. Fast single loop diamagnetic measurements on the TCV tokamak. *Rev. Scient. Instr.*, 74:4634, 2003. <http://dx.doi.org/10.1063/1.1614856>.
- [Moret et al.(2015)] J.-M. Moret et al. Tokamak equilibrium reconstruction code LIUQE and its real time implementation. *Fusion Eng. Des.*, 91:1–15, 2015. <http://dx.doi.org/10.1016/j.fusengdes.2014.09.019>.
- [Na et al.(2016)] Y.-S. Na et al. On benchmarking of simulations of particle transport in ITER. In *Proceed. 26th IAEA Fusion Energy Conf. (Naka, Japan), to be published in Nucl. Fus.*, 2016. Report EUROfusion WPJET1-CP(16) 15339.

- [Nave et al.(2003)] M. F. F. Nave et al. Role of sawtooth in avoiding impurity accumulation and maintaining good confinement in JET radiative mantle discharges. *Nucl. Fus.*, 43: 1204, 2003. <http://dx.doi.org/10.1088/0029-5515/43/10/023>.
- [Neu et al.(2007)] R. Neu et al. Plasma wall interaction and its implication in an all tungsten divertor tokamak. *Plasma Phys. Control. Fusion*, 49:B59, 2007. <http://dx.doi.org/10.1088/0741-3335/49/12B/S04>.
- [Nocedal and Wright(2006)] J. Nocedal and S. Wright. *Numerical Optimization*. Springer, Series in Operations Research and Financial Engineering, 2006.
- [Nunes et al.(2011)] I. Nunes et al. ITER similarity current ramp-down experiments at JET. In *38th EPS Conf. on Plasma Phys. Control. Fusion (Strasbourg, France)*, 2011. <http://ocs.ciemat.es/EPS2011PAP/pdf/P4.106.pdf>.
- [Ödholm et al.(1996)] A. Ödholm et al. Sawteeth-induced impurity transport in tokamak plasmas. *Phys. of Plasmas*, 3:956, 1996. <https://doi.org/10.1063/1.871800>.
- [Ou et al.(2007)] Y. Ou et al. Towards model-based current profile control at DIII-D. *Fusion Eng. Design*, 82:1153, 2007. <http://dx.doi.org/10.1016/j.fusengdes.2007.04.016>.
- [Pankin et al.(2004)] A. Pankin et al. The tokamak Monte Carlo fast ion module NUBEAM in the National Transport Code Collaboration library. *Comp. Phys. Comm.*, 159:157, 2004. <https://doi.org/10.1016/j.cpc.2003.11.002>.
- [Pau et al.(2017)] A. Pau et al. A tool to support the construction of reliable disruption databases. *Fusion Eng. Design*, 125:139, 2017. <https://doi.org/10.1016/j.fusengdes.2017.10.003>.
- [Pautasso et al.(2007)] G. Pautasso et al. Plasma shut-down with fast impurity puff on ASDEX Upgrade. *Nucl. Fus.*, 47:900, 2007. <http://dx.doi.org/10.1088/0029-5515/47/8/023>.
- [Peeters(2000)] A. G. Peeters. The bootstrap current and its consequences. *Plasma Phys. Control. Fusion*, 42:B231, 2000. <http://dx.doi.org/10.1088/0741-3335/42/12B/318>.
- [Pereverzev and Yushmanov(2002)] G. Pereverzev and P. Yushmanov. *ASTRA: Automated System for Transport Analysis (Max-Planck-Institut für Plasmaphysik and Rep. IPP 5 vol 98) (Garching: IPP)*, 2002.
- [Piron et al.(2015)] C. Piron et al. Real-time simulation of internal profiles in the presence of sawteeth using the RAPTOR code and applications to ASDEX Upgrade and RFX-mod. *Proc. of 42nd EPS Conf. on Plasma Phys. Control. Fusion, (Lisbon, Portugal)*, 39E:P1.145, 2015. <http://ocs.ciemat.es/EPS2015PAP/pdf/P1.145.pdf>.
- [Piron et al.(2017)] C. Piron et al. Integration of the state observer RAPTOR in the real-time MARTe framework at RFX-mod. *Fus. Eng. Design*, 123:616, 2017. <http://dx.doi.org/10.1016/j.fusengdes.2017.02.093>.

Bibliography

- [Pitzschke et al.(2012)] A. Pitzschke et al. Electron temperature and density profile evolution during the edge-localized mode cycle in ohmic and electron cyclotron-heated H-mode plasmas in TCV. *Plasma Phys. Control. Fusion*, 54:015007, 2012. <http://dx.doi.org/10.1088/0741-3335/54/1/015007>.
- [Pochelon et al.(1998)] A. Pochelon et al. Preliminary confinement studies during ECRH in TCV. In *In Second Europhysics Topical Conference on Radio Frequency Heating and Current Drive of Fusion Devices, vol. 22 (Brussels, Belgium)*, 1998. <http://ocs.ciemat.es/EPS2011PAP/pdf/P4.106.pdf>.
- [Polevoi et al.(1997)] A. R. Polevoi et al. *Benchmarking of the NBI block in ASTRA code versus the OFMC calculations Report JAERI—Data/Code 97-014*, 1997.
- [Poli et al.(2001)] E. Poli et al. TORBEAM, a beam tracing code for electron-cyclotron waves in tokamak plasmas. *Comp. Phys. Comm*, 136:90, 2001. [https://doi.org/10.1016/S0010-4655\(01\)00146-1](https://doi.org/10.1016/S0010-4655(01)00146-1).
- [Porcelli et al.(1996)] F. Porcelli et al. Model for the sawtooth period and amplitude. *Plasma Phys. Control. Fusion*, 38:2163, 1996. <http://dx.doi.org/10.1088/0741-3335/38/12/010>.
- [Putvinski et al.(1997)] S. Putvinski et al. Halo current, runaway electrons and disruption mitigation in ITER. *Plasma Phys. Control. Fusion*, 39:B157–B171, 1997. <http://dx.doi.org/10.1088/0741-3335/39/12B/013>.
- [Reimerdes et al.(2002)] H. Reimerdes et al. From current-driven to neoclassically driven tearing modes. *Phys. Review Lett.*, 88:105005, 2002. <http://dx.doi.org/10.1103/PhysRevLett.88.105005>.
- [Romanelli(1989)] F. Romanelli. Ion temperature-gradient-driven modes and anomalous ion transport in tokamaks. *Phys. Fluids*, 1:1018, 1989. <http://dx.doi.org/10.1063/1.859023>.
- [Romanelli et al.(2014)] M. Romanelli et al. JINTRAC: A system of codes for integrated simulation of tokamak scenarios. *Plasma and Fusion Research*, 9:3403023, 2014. <https://doi.org/10.1585/pfr.9.3403023>.
- [Romero et al.(2010)] J. A. Romero et al. Plasma internal inductance dynamics in a tokamak. *Nucl. Fus.*, 50:115002, 2010. <http://dx.doi.org/10.1088/0029-5515/50/11/115002>.
- [Ryter et al.(1994)] F. Ryter et al. H-mode results in ASDEX Upgrade. *Plasma Phys. Control. Fusion*, 36:A99, 1994. <http://dx.doi.org/10.1088/0741-3335/36/7A/011>.
- [Ryter et al.(2001)] F. Ryter et al. Experimental evidence for gradient length-driven electron transport in tokamaks. *Phys. Review Lett.*, 86:2325, 2001. <http://dx.doi.org/10.1103/PhysRevLett.86.2325>.
- [Ryter et al.(2003)] F. Ryter et al. Electron heat transport in ASDEX Upgrade: experiment and modelling. *Nucl. Fus.*, 43:1396, 2003. <http://dx.doi.org/10.1088/0029-5515/43/11/011>.

- [Sauter(2016)] O. Sauter. Geometric formulas for system codes including the effect of negative triangularity. *Fusion Eng. Design*, 112:633, 2016. <http://dx.doi.org/10.1016/j.fusengdes.2016.04.033>.
- [Sauter and C.(1999)] O. Sauter and Angioni C. Neoclassical conductivity and bootstrap current formulas for general axisymmetric equilibria and arbitrary collisionality regime. *Phys. of Plasmas*, 6:2834, 1999. <http://dx.doi.org/10.1063/1.873240>.
- [Sauter and Medvedev(2013)] O. Sauter and S. Yu. Medvedev. Tokamak coordinate conventions: COCOS. *Computer Phys. Comm.*, 184:293, 2013. <http://dx.doi.org/10.1016/j.cpc.2012.09.010>.
- [Sauter et al.(1997)] O. Sauter et al. Beta limits in long-pulse tokamak discharges. *Phys. of Plasmas*, 4:1654, 1997. <https://doi.org/10.1063/1.872270>.
- [Sauter et al.(1998)] O. Sauter et al. Sawtooth period simulations of TCV discharges. In *Proc. Joint Varenna-Lausanne Int. Workshop on Theory of Fusion Plasmas, Varenna, Italy, August, 1999*, 1998.
- [Sauter et al.(2001)] O. Sauter et al. Steady-state fully noninductive operation with electron cyclotron current drive and current profile control in the tokamak à configuration variable (TCV). *Phys. of Plasmas*, 8:2199, 2001. <https://doi.org/10.1063/1.1355317>.
- [Sauter et al.(2002a)] O. Sauter et al. Marginal β -limit for neoclassical tearing modes in JET H-mode discharges. *Plasma Phys. Control. Fusion*, 44:1999, 2002a. <http://dx.doi.org/10.1088/0741-3335/44/9/315>.
- [Sauter et al.(2002b)] O. Sauter et al. Control of Neoclassical Tearing Modes by sawtooth control. *Phys. Review Lett.*, 88:105001, 2002b. <http://dx.doi.org/10.1103/PhysRevLett.88.105001>.
- [Sauter et al.(2002c)] O. Sauter et al. Erratum: Neoclassical conductivity and bootstrap current formulas for general axisymmetric equilibria and arbitrary collisionality regime in *Phys. of Plasmas* 6, 2834 (1999). *Phys. of Plasmas*, 9:5140, 2002c. <https://doi.org/10.1063/1.1517052>.
- [Sauter et al.(2010)] O. Sauter et al. On the requirements to control neoclassical tearing modes in burning plasmas. *Plasma Phys. Control. Fusion*, 52:025002, 2010. <http://dx.doi.org/10.1088/0741-3335/52/2/025002>.
- [Sauter et al.(2014)] O. Sauter et al. On the non-stiffness of edge transport in L-mode tokamak plasmas. *Phys. of Plasmas*, 21:055906, 2014. <http://dx.doi.org/10.1063/1.4876612>.
- [Schneider et al.(2000)] W. Schneider et al. ASDEX Upgrade MHD equilibria reconstruction on distributed workstations. *Fusion Eng Design*, 48:127, 2000. [http://dx.doi.org/10.1016/S0920-3796\(00\)00109-5](http://dx.doi.org/10.1016/S0920-3796(00)00109-5).

Bibliography

- [Shafranov(1958)] V. D. Shafranov. On magnetohydrodynamical equilibrium configurations. In *Soviet Journal of Experimental and Theoretical Physics* 6, pp. 545–+, 1958.
- [Shafranov(1966)] V. D. Shafranov. Plasma equilibrium in a magnetic field. *Rev. Plasma Phys.*, 2:103, 1966.
- [Shimada et al.(2007)] M. Shimada et al. *Progress in ITER Physics Basis, Chapter 1: Overview and summary*, 2007. <http://dx.doi.org/10.1088/0029-5515/47/6/S01>.
- [Sips et al.(2009)] A. C. C. Sips et al. Experimental studies of ITER demonstration discharges. *Nucl. Fus.*, 49:085015, 2009. <http://dx.doi.org/10.1088/0029-5515/49/8/085015>.
- [Snyder et al.(2011)] P. B. Snyder et al. A first-principles predictive model of the pedestal height and width: development, testing and ITER optimization with the EPED model. *Nucl. Fus.*, 51:103016, 2011. <http://dx.doi.org/10.1088/0029-5515/51/10/103016>.
- [Strait(1994)] E. J. Strait. Stability of high beta tokamak plasmas. *Phys. of Plasmas*, 1:1415, 1994. <https://doi.org/10.1063/1.870691>.
- [Stubberfield and Watkins(1987)] P. M. Stubberfield and M. L. Watkins. *Multiple PENCIL beam Report*. JET Joint Undertaking, Abingdon, Oxfordshire DPA(06)/87, 1987.
- [Sugihara et al.(2007)] M. Sugihara et al. Disruption scenarios, their mitigation and operation window in ITER. *Nucl. Fus.*, 47:337, 2007. <http://dx.doi.org/10.1088/0029-5515/47/4/012>.
- [Teo et al.(1991)] K. L. Teo et al. *A unified computational approach to optimal control problems*. Pitman Monographs and Surveys in Pure and Applied Mathematics. John Wiley and Sons Inc., 1991.
- [Teplukhina et al.(2017)] A. A. Teplukhina et al. Simulation of profile evolution from ramp-up to ramp-down and optimization of tokamak plasma termination with the RAPTOR code. *Plasma Phys. Control. Fusion*, 59:124004, 2017. <https://dx.doi.org/10.1088/1361-6587/aa857e>.
- [Tonks and Langmuir(1929)] L. Tonks and I. Langmuir. General theory of the plasma of an arc. *Phys. Rev.*, 34:876, 1929. <https://doi.org/10.1103/PhysRev.34.876>.
- [Treutterer et al.(2014)] W. Treutterer et al. ASDEX Upgrade Discharge Control System — A real-time plasma control framework. *Fus. Eng. Design*, 89:146, 2014. <http://dx.doi.org/10.1016/j.fusengdes.2014.01.001>.
- [Troyon et al.(1984)] F. Troyon et al. MHD-limits to plasma confinement. *Plasma Phys. Control. Fusion*, 26:209, 1984. <https://dx.doi.org/10.1088/0741-3335/26/1A/319>.
- [Urano(2014)] H. Urano. Pedestal structure in H-mode plasmas. *Nucl. Fus.*, 54:116001, 2014. <http://dx.doi.org/10.1088/0029-5515/54/11/116001>.

- [van Dongen et al.(2014)] J. van Dongen et al. Numerical optimization of actuator trajectories for ITER hybrid scenario profile evolution. *Plasma Phys. Control. Fusion*, 56:125008, 2014. <https://dx.doi.org/10.1088/0741-3335/56/12/125008>.
- [von Goeler et al.(1974)] S. von Goeler et al. Studies of internal disruptions and $m = 1$ oscillations in tokamak discharges with soft—X-Ray techniques. *Phys. Review Lett.*, 33:1201, 1974. <https://doi.org/10.1103/PhysRevLett.33.1201>.
- [Weiland et al.(2017)] M. Weiland et al. Real-time simulations of the NBI fast-ion distribution function. In *Proc. the 15th IAEA Technical Meeting on Energetic Particles in Magnetic Confinement Systems (IAEA 2017 TM EP, Princeton, NJ, USA)*, 2017. Submitted to Nucl. Fus.
- [Wesson(2004)] J. Wesson. *Tokamaks*. Oxford Science Publications, New York (USA), 2004.
- [Westerhof(2006)] E. Westerhof. Electron cyclotron waves. *Fus. Science Techn.*, 49 (2T):195, 2006. <https://doi.org/10.13182/FST06-A1119>.
- [Witrant et al.(2007)] E. Witrant et al. A control-oriented model of the current profile in tokamak plasma. *Plasma Phys. Control. Fusion*, 49:1075, 2007. <https://doi.org/10.1088/0741-3335/49/7/009>.
- [Wolf(2003)] R. C. Wolf. Internal transport barriers in tokamak plasmas. *Plasma Phys. Control. Fusion*, 45:R1–R91, 2003. <https://doi.org/10.1088/0741-3335/45/1/201>.
- [Xu et al.(2013)] C. Xu et al. Computing open-loop optimal control of the q-profile in ramp-up tokamak plasmas using the minimal-surface theory. *Plas. Scien. Tech.*, 15:403, 2013. <http://dx.doi.org/10.1088/1009-0630/15/5/02>.
- [Zucca et al.(2009)] C. Zucca et al. Current density evolution in electron internal transport barrier discharges in TCV. *Plasma Phys. Control. Fusion*, 51:015002, 2009. <https://dx.doi.org/10.1088/0741-3335/51/1/015002>.

Acknowledgements

Four years in SPC were a great journey to plasma physics, and I would like to dedicate a few warm words to my colleagues and friends.

First of all, I am deeply grateful to my supervisor Olivier Sauter. Working with a person who has such a broad knowledge in plasma physics, numerical modelling and experimental research, was a great benefit, and I could not ask for a better teacher. His constant support and enthusiasm have helped me to gain experience in various aspects of scientific and daily life. I am thankful for his everyday readiness for discussions and endless optimism moving me forward during these four years.

My sincere thanks to Federico Felici, main RAPTOR developer and control expert. I was always rather far from control engineering tasks, but thanks to Federico and his doubtless competence I have got an opportunity to extend my knowledge in this field. His valuable advices and fruitful collaborative work on the RAPTOR code development have been an essential part of this thesis. I am very grateful for his priceless contribution to my research.

I would like to thank members of the RAPTOR team. It was a pleasure to collaborate with SPC colleagues Mengdi, Trang, Francesco, and Christian, our colleagues from the Netherlands Thomas, Bert and Maximilian, and many other team members and collaborators who worked for RAPTOR improvements and control problems. Our RAPTOR meetings and weeks of the MST1 campaign were always very productive and expanding horizons. Apart from long working hours and late dinners (oh pizza in the control room!), our numerous social events, like the Carnival in Eindhoven, summer evenings in Beer Garten(s) and Swiss fondues were not forgettable. I was very happy to be a part of this team enjoying a friendly atmosphere and an effective teamwork. “Many hands make light work” – this is certainly about us.

I am very grateful to the jury members on my private defense, the president Prof. Frédéric Mila, and the experts, Dr. Emmanuel Joffrin, Dr. Thomas Pütterich, and Dr. Jean-Marc Moret, for their time, questions and practical advices on improving this thesis. It was a great advantage to have three scientists from three tokamaks and to get their qualified opinion on the various aspects of my research. Also I would like to thank Jean-Marc Moret for detailed discussions on TCV plasma modelling and control issues, Thomas Pütterich for his support and priceless help during experiments on ASDEX Upgrade, and Emmanuel Joffrin for his valuable comments on

Bibliography

JET plasma modelling tasks.

My working days would not be the same without SPC doctoral and post-doctoral community. Their endless enthusiasm and infinite interests in physics were always a source of inspiration for me. Being a part of this solid group was a great and beneficial experience. It was a pleasure to have such nice office mates, Madhu and Rogerio. I would like to thank SPC scientific staff for their valuable advices and sharing sacral knowledge of plasma physics. Special thanks to Antoine Merle for taking all my questions seriously and detailed explanations of various know-hows. I really appreciated the everyday support from the SPC administration. My research could not be done without many working hours of numerous members of experimental and technical teams of the TCV, ASDEX Upgrade and JET tokamaks. I am deeply grateful to everyone for their priceless job.

It was never easy to find a proper work-life balance. I was very lucky to meet so many nice people in Lausanne and surroundings. Exploring Swiss Alps and kilometres of mountain trails passed together were a valuable and memorable experience. Parties, BBQs, fondues would not be so enjoyable, and even possible, without you, my dear friends. I understood that world is very small when met Olga in Lausanne and I appreciate 10 years of our friendship. Special thanks to Eugene for staying an enthusiastic party organizer, to Svyatoslav for bringing the Russian culture to masses and to Giorgio for being one of the most cheerful persons I have ever met. It was a great pleasure to see in EPFL so many members of the PhysTech family, successfully working in different fields of research and always sharing their joyfulness.

I would like to thank my parents and my brother for their continuous support, even being so far away. At last but not at least, my deepest gratitude belongs to my husband Albert for making me so happy all these years.

Lausanne, 12 March 2018

Anna

Anna Teplukhina

Address: Route du Lac 22, 1026 Denges, Switzerland

E-mail: anna.a.teplukhina@gmail.com

Citizenship: Russia

Date of birth: 29 November 1990



Research experience

2014 – 2018 **EPFL Swiss Plasma Center, Lausanne, Switzerland**

Doctoral assistant

- Development of the rapid plasma transport simulator RAPTOR (MATLAB): simulations of an entire shot from ramp-up to ramp-down; implementation of the ad-hoc gradient-based transport models for electrons; validation of the modelling results with experimental measurements.
- Development of an optimization procedure for a tokamak plasma ramp-down phase with the MATLAB optimization toolbox.
- Participation in the European experimental and simulation campaigns at the TCV (Lausanne, Switzerland), ASDEX Upgrade (Garching-bei-Munchen, Germany) and JET (Culham, United Kingdom) tokamaks.

2010 – 2014 **NRC Kurchatov Institute, Institute of Tokamak Physics, Moscow, Russia**

Research fellow

- Development of the numerical code (FORTRAN) for simulations of the fast ions interaction with ion-cyclotron waves in the ITER plasma on the computer cluster of the Institute of Tokamak Physics.

Education

2014 – 2018 **Ecole Polytechnique Fédérale de Lausanne (EPFL), Lausanne, Switzerland**

Ph.D. student, Doctoral Program in Physics (EDPY)

Thesis topic: Realistic multi-machine tokamak profiles simulations and numerical ramp-down optimization using the RAPTOR code.

Supervisor: MER Dr. Olivier Sauter

2011 – 2013 **Moscow Institute of Physics and Technology (MIPT), Moscow, Russia**

M.Sc. in Applied Mathematics and Physics, GPA 5.00/5.00

Thesis topic: Simulations of fast ions interaction with ion-cyclotron waves in tokamak plasmas.

Supervisor: Dr. Sergey V. Konovalov

2007 – 2011 **Moscow Institute of Physics and Technology (MIPT), Moscow, Russia**

B.Sc. in Applied Mathematics and Physics, GPA 4.95/5.00

Selected Journal Publications

- **A. A. Teplukhina**, O. Sauter, F. Felici, et al. (2017). "Simulation of profile evolution from ramp-up to ramp-down and optimization of tokamak plasma termination with the RAPTOR code", Plasma Physics and Controlled Fusion 59 124004, [doi: 10.1088/1361-6587/aa857e](https://doi.org/10.1088/1361-6587/aa857e).
- F. Felici, J. Citrin, **A. A. Teplukhina**, et al. (2017). "Real-time-capable multichannel tokamak transport simulations using RAPTOR", submitted to Nuclear Fusion.

- P. de Vries, et al. incl. **A. A. Teplukhina** (2018). "*Multi-machine analysis of termination scenarios with comparison to simulations of controlled shutdown of ITER discharges*", Nuclear Fusion 58 026019, [doi:10.1088/1741-4326/aa9c4c](https://doi.org/10.1088/1741-4326/aa9c4c).
- E. Maljaars, et al. incl. **A. A. Teplukhina** (2017). "*Profile control simulations and experiments on TCV: a controller test environment and results using a model-based predictive controller*", Nuclear Fusion 57 126063, [doi:10.1088/1741-4326/aa8c48](https://doi.org/10.1088/1741-4326/aa8c48).

Selected Conference Presentations

- | | |
|------|---|
| 2017 | 59th Annual Meeting of the APS Division of Plasma Physics
A. A. Teplukhina, O. Sauter, F. Felici, et al., " <i>Numerical optimization of the ramp-down phase with the RAPTOR code</i> ", Milwaukee, WI, USA, poster JP11 139. |
| 2016 | 16th Joint Varenna – Lausanne International Workshop
A. A. Teplukhina, O. Sauter, F. Felici, et al., " <i>Numerical optimization of ramp-down phases for TCV and AUG plasmas</i> ", Varenna, Italy, poster P–16. |
| 2015 | 16th European Fusion Theory Conference
A. A. Teplukhina, O. Sauter, F. Felici, " <i>Current ramps optimization study with the RAPTOR code</i> ", Lisbon, Portugal, poster P2.12. |
| 2013 | 40th EPS Conference on Plasma Physics
A. A. Teplukhina, K.O. Aleynikova, P.B. Aleynikov, S.V. Konovalov, " <i>Calculation of the ICRF heated ion distribution function inside NPA viewing angle in ITER</i> ", Espoo, Finland, poster P1.094. |
| 2012 | 39th EPS Conference on Plasma Physics
A. A. Teplukhina, et al (2012), " <i>Simulation of fast ions interaction with ICRF wave in realistic tokamak magnetic field</i> ", Stockholm, Sweden, poster P1.150. |

Honours and Awards

- | | |
|-------------|--|
| 2016 | EPFL prize to the most dedicated teaching assistants in the physics section |
| 2012 | Kurchatov Award (NRC Kurchatov Institute prize) for the best student work "Dynamics simulation for high-energy ions beam and ICR heating ions in ITER" |
| 2012 – 2013 | A.P. Alexandrov scholarship for young researches in NRC Kurchatov Institute |
| 2012 – 2013 | Special state academic scholarship for the advanced MIPT master students |
| 2008 – 2010 | Scholarship of the Innovative Education Development Fund for the advanced MIPT bachelor students |

Teaching Experience

- | | |
|-------------|--|
| 2016 – 2017 | Teaching assistant for the 2nd year bachelor students EPFL: Computational Physics, exercise sessions. |
| 2014 – 2016 | Teaching assistant for the 3d year bachelor students EPFL: Physics Laboratory Sessions, experiments related to plasma physics. |

Skills

- | | |
|-------------|---|
| Programming | MATLAB, FORTRAN 77/90, C/C++ |
| Others | Linux, Windows, LaTeX, numerical optimization methods |

Languages

- | | | | |
|-----------|--------|----------|-----------------------------|
| • English | Fluent | • French | Basic communication (A2/B1) |
| • Russian | Native | • German | Basic communication (A2) |

